Frequency comb spectroscopy on trapped calcium ions

VRIJE UNIVERSITEIT

Frequency comb spectroscopy on trapped calcium ions

ACADEMISCH PROEFSCHRIFT

ter verkrijging van de graad Doctor aan
de Vrije Universiteit Amsterdam,
op gezag van de rector magnificus
prof.dr. L.M. Bouter,
in het openbaar te verdedigen
ten overstaan van de promotiecommissie
van de faculteit der Exacte Wetenschappen
op donderdag 7 juli 2011 om 11.45 uur
in de aula van de universiteit,
De Boelelaan 1105

door

Anne Lisa Wolf

geboren te Zevenhoven

promotoren:	prof. dr. W.M.G. Ubachs
	prof. dr. K.S.E. Eikema
copromotor:	dr. S. van den Berg

Als je niet te diep nadenkt dan klopt alles
Herman Finkers

This thesis was reviewed by the following committee:

prof. dr. K.-J. Boller
prof. dr. M. Drewsen
dr. D. Iannuzzi
prof. dr. K.H.K.J. Jungmann
prof. dr. P.O. Schmidt

This work is part of the Industrial Partnership Programme (IPP) Metrology with Frequency Comb Laser (MFCL) of the Stichting voor Fundamenteel Onderzoek der Materie (FOM), which is supported financially by the Nederlandse Organisatie voor Wetenschappelijk Onderzoek (NWO). The IPP MFCL is co-financed by TNO and ASML, and it is supported and co-financed by VSL as part of the VSL metrological research program, which is funded by the Ministry of Economic Affairs of the Netherlands.

Contents

Chapter 1

Introduction

1.1 Precision spectroscopy

1.1.1 Introduction

Frequency, and therefore by definition also time, is the physical quantity which can be measured to the highest precision. The measurement of frequency is based on the counting of cycles, which can vary from the rotation of the earth, to the motion of a pendulum or the oscillation of a quartz crystal. Higher frequencies are in principle more suitable as a time standard. Precision spectroscopy relies on the counting of frequencies, in order to measure the energy level structure of an atom, ion or molecule. The record in accuracy for such a measurement is held by the time and frequency division at the National Institute of Standards and Technology in Boulder (USA), where an impressive inaccuracy of 9 parts in 10^{18} was obtained in a comparision of the $^1S_0 - ^3P_0$ transition in two $^{27}Al^+$-clocks [1]. These high precision measurements were made possible by three major developments in atomic physics in the past century, which were all awarded a Nobel prize.

The first of these ingredients is the invention of the Paul trap [2]. W. Paul was awarded the Nobel prize in 1989 for 'contributions of importance for the development of atomic precision spectroscopy'. His Paul trap confines charged particles in three dimensions by using a combination of static and electric fields (see Chapter 2). In such an ion trap particles can be confined for almost infinitely long times. Eventually, ions will get lost due to collisions with the background gas, although this process can take months under high vacuum conditions. A long trapping time allows for long interaction times and can as such improve the obtainable accuracy.

The second important step forward was the development of the technique of laser cooling of atoms (Chapter 2). The Nobel prize in 1997 was granted for the realization of cooling and trapping of atoms to S. Chu, C. Cohen-Tannoudji and W.D. Phillips. This cooling method uses a red-detuned laser to extract energy from the atom. Temperatures in the order of a millikelvin are routinely realized using this technique, and thus the Doppler line-broadening can be strongly reduced. By cooling the particles, the lineshape of an atomic transition can be narrowed down to the natural linewidth, which makes a more precise determination of the line center possible. From the first suggestions and realization of laser cooling, the implications for improvement of accuracy were already recognized [3–5]. Since these first laser-cooling experiments, the accuracy of spectroscopy on cold particles has developed at great speed, improving the record accuracy by many orders of magnitude over the years.

The third important invention is the frequency comb laser [6–8] (Chapter 3), for which the Nobel prize was awarded in part in 2005 to J.L. Hall and T.W. Hänsch. As mentioned before, precision spectroscopy is performed by counting frequencies. Optical frequencies are too high to be counted directly by electronic means. Before the development of the frequency comb, complicated frequency chains were necessary for absolute optical frequency measurements, in order to phase-coherently link visible wavelengths to the caesium standard by upconversion and many transfer lasers [9, 10]. These frequency chains had the additional drawback that they were designed to measure only a single frequency. The complexity of optical frequency measurements was strongly reduced with the development of the optical frequency comb laser. The spectrum of this device consists of a large number of phase-locked modes. The position of the modes is determined by two RF frequencies (the laser repetition frequency and the carrier-envelope offset frequency), both of which can be accurately measured. In this way the comb frequencies can be directly linked to the caesium or another frequency standard, greatly simplifying absolute frequency calibration of THz to PHz frequencies. In addition, a broadband spectrum is available directly from the comb, making the laser suitable to calibrate transitions over a wide range of wavelengths using a single frequency comb.

These three milestones in physics from the past decades have improved the attainable precision in (ion) spectroscopy enormously. Not only did they improve the ultimate precision that can be obtained in such measurements, they also made high accuracy frequency calibration more widely available. Many laboraties now have constructed Paul traps with laser-cooled ions and/or frequency combs for various applications, which will be discussed in the following section.

1.2 Applications of precision spectroscopy

The combination of cold, trapped ions and the highly stable lasers that are now available finds applications in three main research areas in atomic physics. Firstly, high accuracy frequency calibrations as described in 1.1.1 enable more accurate clocks and possibly a new frequency standard. Secondly, the ability to very precisely calibrate atomic transition frequencies can be used to test fundamental theories. Examples of such research include testing the validity of quantum electrodynamics [10–12], measuring atomic parity violation [13] and probing the stability of the fine-structure constant [14, 15]. A third application is found in the field of quantum computing, where the combination of a high degree of control over the trapped ions and laser frequencies allows for precise manipulation of atomic states [16, 17].

1.2.1 Ion clocks

A particular atomic transition needs to meet certain requirements to be useful as a frequency standard. To minimize fluctuations of the output signal, the natural linewidth of the resonance needs to be small, the interaction time and/or ion number should be sufficiently high to provide a good signal-to-noise ratio and a narrow band laser source needs to be available to probe the resonance with high resolution. In addition, systematic shifts of the output frequencies need to be well under control, requiring a transition that is insensitive to electric and magnetic fields and that can be measured in cold atoms to minimize Doppler shifts. For the development of a new frequency standard, systems based on trapped and laser-cooled atoms or ions can meet these requirements. These are promising candidates due to their high stability and accuracy compared to the current caesium standard.

For neutral atoms, clocks can be built which use a so-called optical lattice to confine the particles. This method has the advantage that large numbers ($\approx 10^6$) of atoms can be used, resulting in a short term stability that is superior over trapped ion clocks which usually consist of only one ion. However, the uncertainty that is currently realized with optical lattice clocks of 1.5×10^{-16} [18] is much lower than the fractional frequency inaccuracy of 9×10^{-18} which has been obtained for ion clocks [1]. The main advantage of an ion clock leading to this high accuracy is the possibility to trap the ion for very long times (we have observed lifetimes of over a working day), allowing for very long interrogation times and a good control over systematic effects.

Clocks based on an aluminium ion are very promising candidates for a new time standard. The aluminium ion has a very low black-body radiation shift, reducing possible systematic errors [19]. However, research on other possible ions such as Hg^+ [14, 20], Yb^+ [21, 22], In^+ [23], Sr^+ [24, 25] and Ca^+ [26, 27] is also ongoing, and the most suitable candidate for a new standard still needs to be determined.

1.2.2 Variation of the fine-structure constant

Trapped and laser-cooled ions provide a good testing ground for fundamental theories, since their reduced Doppler width and long interrogation times allow for very high precision measurements. One of these tests involves the measurement of the stability of the fine-structure constant $\alpha = e^2/4\pi\epsilon_0\hbar c$, where e is the electron charge, ϵ_0 the electric permitivitty in vacuum, $\hbar$ is Plack's constant divided by 2π, and c is the speed of light. The value of $\alpha \approx 1/137$ is not determined within the Standard Model, and there are theories which allow for a variation of this constant (see [28, 29] and references therein). A possible drift in α can be detected by comparing measurements of atomic transition frequencies over time. The combination of several highly accurate laboratory measurements of such frequencies now yield the result on the variation of α of $\Delta\alpha/\alpha = (-1.6 \pm 2.3) \times 10^{-17}$ per year in the current epoch, based on the frequency ratio measurement of an Al^+ and Hg^+ ion clock [14].

A different approach to measure a drift of α is to compare laboratory spectroscopy data to astronomical observations of strong transitions, which would allow for the detection of $\Delta\alpha/\alpha$ over billions of years (the time it takes for the light from dust clouds at high redshift to reach the earth). Such a variation in the fine-structure constant could in principle be obtained by comparing very accurate astronomical spectroscopy data for a single absorption line with laboratory spectroscopy data, where a difference in the line position between these measurements would mean a change in α. However, there are many possible systematic effects which can cause such a shift. By using many different absorption lines in different atomic and ionic species, all with a different sensitivity to a change in the fine-structure constant [30], systematic effects can be ruled out, and even a small change in α may be detected. This method is known as the Many Multiplet method [31].An example of some ionic and atomic transitions that are of interest for such an analysis are given in [32], together with the induced shift of a spectral line as a function of the variation of α (the sensitivity coefficient for $\Delta\alpha/\alpha$). The Many Multiplet method has been applied on many different quasar absorption spectra by several groups, but the results on $\Delta\alpha/\alpha$ that are presented in the litera-

ture are not consistent [33]. However, the comparison with the largest sample size (143 quasar absorption systems) and widest range of redshifts ($0.2 < z_{abs} < 4.2$)* that has been reported so far yields a result of $\Delta\alpha/\alpha = (-0.57 \pm 0.11) \times 10^{-5}$ [34]. For several spectroscopic lines that are relevant for the Many Multiplet method, the absolute wavelength accuracy does not match the level of 10^{-7}, which is feasible in astrophyiscal observations, so renewed laboratory precision measurements on dipole-allowed transitions may help to improve on the current results.

1.2.3 Quantum computing

A third application of ion trapping is found in the field of quantum computing. While in a classical computer a bit can have only two states, $|0\rangle$ or $|1\rangle$, the bits in the quantum computer can be in a superposition of states of the form $\alpha|0\rangle + \beta|1\rangle$. Due to this quantum nature of the bits, the system can be initialized into a superposition of the possible inputs, and the operations can then be processed on these inputs in parallel. However, by reading out the information, the state will be projected onto either state $|0\rangle$ or state $|1\rangle$. To make use of the parallel processing, an algorithm needs to be designed in order to extract the desired information. Certain mathematical problems are more easily solved in this way than using a classical computer. A selection and explanation of algorithms for quantum computers can for example be found in [35] or [36], including Shor's algorithm for factoring large numbers and Grover's algorithm for searching a database.

In an ion trap-based 'quantum computer' the bits are formed by the internal quantum states of the ion, being the ground state and a metastable excited state which lives long enough to process the calculation. These states can be manipulated using well-controlled laser pulses, and the detection of fluorescence from a shorter-lived state can be used to read out the bit. The individual bits can be coupled through excitation of collective motion of the ions. The use of cold trapped ions for calculating quantum algorithms was first suggested by Cirac and Zoller [37], and the first bit flip on a single ion was shown shortly after at NIST on trapped $^9Be^+$ [38]. Since this first experiment in the research of ion-based quantum computers, the field has widely expanded. An overview of the development in trapped ion quantum bits until 2009 can be found in [16] and [17]. Recently it was shown that the addition of a frequency comb to such a setup can be very useful, due to the available phase control between pulses and comb modes [39].

*In cosmology, the lookback time is usually expressed in the redshift z of the spectral lines, which is an observable. The time corresponding to this redshift is dependent on the expansion model for the universe, and is on the order of 10×10^9 year for the mentioned redshifts.

1.2.4 The calcium ion

Calcium is a versatile ion for all the above mentioned applications, and it is particularly popular in the field of quantum computing. The calcium ion has only one valence electron, yielding a relatively simple energy level structure which can be used for laser cooling. The transition frequencies that are relevant for this thesis are given in Table 1.1. In addition, the wavelengths needed for laser cooling are well accessible using diode- or (frequency doubled) Ti:Sa lasers. These properties, in combination with the presence of long-lived D-states, make the calcium ion a good candidate for both quantum computing [40] and for building an ion clock based on $^{43}Ca^{+}$ [41].

Calcium ions have a low sensitivity to the applied electric fields, due to the open level structure of the ion (so that states are not easily mixed by external fields). In addition, the $^{43}Ca^{+}$ isotope, with a nuclear spin of $7/2$, provides a state without first order Zeeman shift. However, the natural abundance of $^{43}Ca^{+}$ is only $0.135(10)\%$ (table 2.1). The precision measurements of the $4s\,^2S_{1/2} - 3d\,^2D_{5/2}$ clock transition in trapped calcium ions have so far only been performed on the most abundant isotope $^{40}Ca^{+}$ [26], [27], [42]. The most accurate transition frequency measurement up to date has yielded a result of $f_{trans} = 411\,042\,129\,776\,393.2(1.0)$ Hz [27].

For the application of measuring a possible variation of the fine-structure constant on a cosmological timescale, the calcium ion is also of interest. In order to measure such a variation, not only calcium but many different atomic and ionic transitions are compared using the Many-Multiplet method [30, 31]. Among these transitions are the $4s\,^2S_{1/2} - 4p\,^2P_{1/2}$ and $4s\,^2S_{1/2} - 4p\,^2P_{3/2}$ transitions in the calcium ion. Due to the relatively long wavelength of 400 nm, these absorption lines are shifted out of the detection region of the major telescopes and attached spectrometers (VLT-UVES and Keck-HIRES) for a redshift of approximately $z > 2$ and can thus only be used for a comparison at relatively low redshifts.

For the application in quantum computation also first the $^{43}Ca^{+}$ isotope was suggested [40], while the more abundant $^{40}Ca^{+}$ ion became the most widely used isotope. Calcium is suitable for quantum computing due to the readily available cooling lasers, and the presence of Hz-level linewidth electric quadrupole transitions that allows for resolved sideband cooling to the vibrational ground state and low decoherence. The implementation of a quantum algorithm using calcium ions was first demonstrated in Innsbruck [43]. By the inclusion of Zeeman states on the ^{40}Ca-isotope [44], entanglement up to 20 s was observed. Since the first use of calcium for a quantum algorithm both the number of entangled ions (creating

Transition		ν (MHz)	$\Delta\nu$ (MHz)	ref.
$4s\,^2\mathrm{S}_{1/2} - 4p\,^2\mathrm{P}_{1/2}$	*	755 222 766.2 (1.7)	22	[47]
$4s\,^2\mathrm{S}_{1/2} - 4p\,^2\mathrm{P}_{3/2}$	*	761 905 012.7 (0.5)	23	[48]
Transition		ν (Hz)	$\Delta\nu$ (Hz)	ref.
$4s\,^2\mathrm{S}_{1/2} - 3d\,^2\mathrm{D}_{5/2}$	†	411 042 129 776 393 (1)	0.14	[27]
$3d\,^2\mathrm{D}_{3/2} - 3d\,^2\mathrm{D}_{5/2}$		1 819 599 021 504 (37)	0.4	[49]

Table 1.1: The transition frequencies (ν) between the levels in $^{40}Ca^+$ that are considered in this thesis and their measurement uncertainty (between brackets). For comparison the natural linewidth ($\Delta\nu$) is also included. * Measured in this work, † Measured in this work to an accuracy of 0.3 MHz, the highest available accuracy result is given.

up to 8 entangled ions[45]) and the fidelity (reaching 99.99% fidelity for a single qubit [46]) have increased.

1.3 Outline

In this thesis the research we have performed on different forms of precision spectroscopy of trapped calcium ions is described. For the experiments two ion traps have been constructed, which are characterized in Chapter 2. In addition, two frequency combs were built to perform high-precision calibrations of atomic transition frequencies. The principle and properties of these Ti:Sa frequency combs are described in Chapter 3. Frequency combs can be used by either referencing an additional laser to a comb mode, or by employing the comb modes themselves for excitation of a transition. These techniques are outlined in Chapter 4. We have performed several spectroscopy experiments, which show the versatility of frequency comb spectroscopy. In the first experiment which is described in this thesis, a diode laser is used for excitation of the $4s\,^2\mathrm{S}_{1/2} - 4p\,^2\mathrm{P}_{1/2}$-transition in the calcium ion. The frequency of this diode laser is calibrated against the frequency comb (Chapter 5). In Chapter 6 the technique of direct frequency comb spectroscopy (DFCS) on trapped ions is demonstrated using the dipole-allowed $4s\,^2\mathrm{S}_{1/2} - 4p\,^2\mathrm{P}_{3/2}$-transition in $^{40}Ca^+$. We also showed that DFCS can be employed for the detection and calibration of very weak transitions, by exciting and measuring the dipole-forbidden $4s\,^2\mathrm{S}_{1/2} - 3d\,^2\mathrm{D}_{5/2}$-transition in calcium, as is shown in Chapter 7.

Chapter 2

Ion traps

2.1 The Paul trap

2.1.1 The first Paul trap

In a Paul trap a combination of oscillating and constant electric fields is used to confine ions in three dimensions. With the oscillating voltage, a "pseudopotential" is formed with a minimum in the trap center. The first radio frequency or Paul trap was built in 1954 [2] using a three-dimensional, hyperbolic electrode configuration (Fig. 2.1). In this trap molecular ions (such as H_2O^+, N_2^+ and propane), but also xenon and krypton ions were confined [50]. Due to its geometry, such trap only has a zero field in the exact center, making it very suitable for the trapping of single ions and the development of ion clocks. However, there are also occasions where the trapping of larger numbers of ions is preferred. When more ions are stored in such a Paul trap, they repel each other through the Coulomb force. The ions will thus be forced outward in the dynamic potential, where the field changes are much higher and the ions will be heated through their interactions in the RF field.

A development simultaneous to the Paul trap, originating from the same group, was the invention of the so-called mass filter or mass spectrometer [51]. This device consists of four elongated hyperbolic electrodes, where an RF potential is applied to two diagonally facing rods, while the other two carry an RF potential equal in magnitude 180° out of phase. The generated field provides a guide for ions with a specific m/q ratio (where m is the mass of the ion and q its charge), and can filter out others. Despite the presence of both the ion trap and the mass spectrometer, it took until 1989 to combine the two into a linear Paul trap [52]. This ion cage consists of four linear electrodes confining the ions radially, and two endcap electrodes that constrain the particles in the axial direction, where the

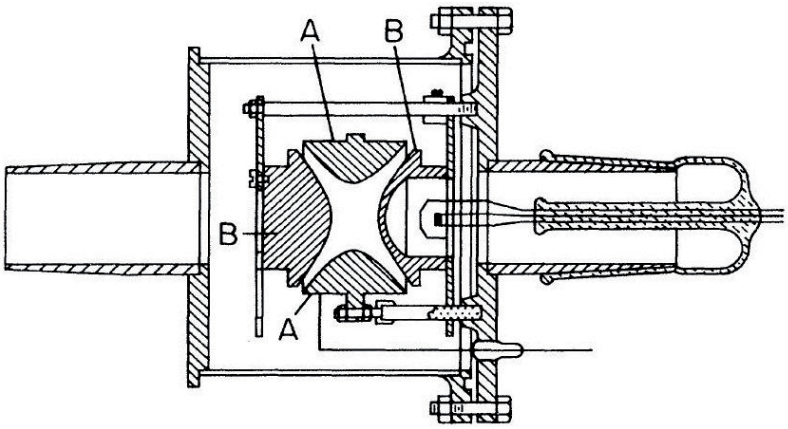

Figure 2.1: Hyperbolic trap configuration, as used in the first radiofrequency (RF) trap constructed by Paul and coworkers [2]. On the ring electrode A an RF potential is applied, while the end-cap electrodes B carry a constant (direct current or DC) potential.

axial confinement can be much weaker than the radial confinement. For convenience of construction instead of hyperbolic electrodes (that provide a perfectly harmonic potential) usually cylindrical electrodes are used. One of our linear Paul traps, which will be further described in section 2.3.1, is depicted in Fig. 2.2.

2.1.2 The potential in an infinite linear Paul trap

The trapping potential ϕ can in general be obtained from solving the Laplace equation while including the boundary conditions for the electrode configuration:

$$\nabla^2 \phi = 0 \tag{2.1}$$

The radial electric field in a linear Paul trap can be approximated by calculating the properties of a configuration consisting of four infinite cylindrical rods, which means there is no electric field component along the axial direction. By using separation of variables in cylindrical coordinates, a general solution of this equation can be found of the form:

$$\phi(r,\theta) = (A\ \cos\ k\theta + B\ \sin\ k\theta) \times (C\, r^k + D\, r^{-k}) \tag{2.2}$$

where A, B, C and D and k are all constants to be determined by the boundary conditions, and the coordinate θ and r are defined in Fig. 2.3. The trap is symmetric in θ, imposing the value $B = 0$. In addition, the field will have a finite

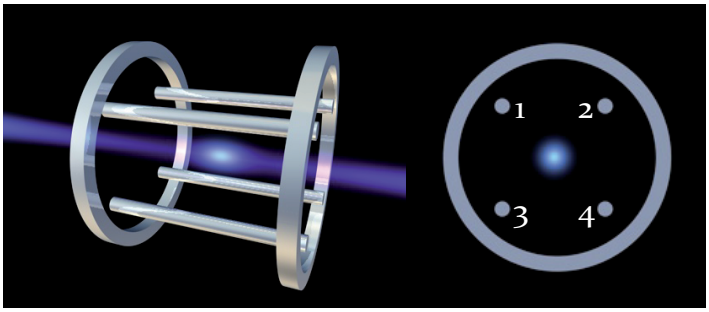

(a) Side view (b) Axial view

Figure 2.2: Electrode configuration for our first linear trap. The trap consists of four linear electrodes (labeled 1-4) for radial confinement: A Radio Frequency voltage is put on two diagonally facing rods (1,4), while the other two rods are grounded (2,3). A DC voltage is applied to the ring electrodes for axial confinement.

value in the center of the trap at $r = 0$, so also the constant $D = 0$. The symmetry of the trap requires an extreme at $\theta = \pm\pi/2$, opposite in sign to the value at $\theta = n\pi$, which leads to $k = 2(2n + 1) = 2, 6, 10, ...$The general expression for the potential is found by adding all possible singular solutions, leading to the total solution:

$$\phi(r, \theta) = \sum_n C_n r^{2(2n+1)} \cos\ 2(2n + 1)\theta \tag{2.3}$$

In the center of the trap, to first order (for $n = 0$), the sum in equation (2.3) can be written in rectangular coordinates with the substitutions $r^2 = x^2 + y^2$, $\theta = \tan^{-1} \frac{y}{x}$ and using the exponential expressions for the trigonometric functions, which results in a hyperbolic potential:

$$\phi(x, y) = C_0\ (x^2 - y^2) + C_p \tag{2.4}$$

Since the potential is only defined up to a certain reference point, the constant C_p can be added here to satisfy the boundary conditions. In this first order approximation the potential is equal to that formed by four hyperbolic surfaces, with a voltage V_0 applied at the electrodes at $x^2 = y^2 \pm r_0^2$ and $V = 0$ at $y^2 = x^2 \pm r_0^2$, where r_0 is the distance between the center and the electrode surface. It has been shown numerically that a trap with cylindrical electrodes has the best suppression of the first higher order (non-quadrupole) mode when the ratio between the

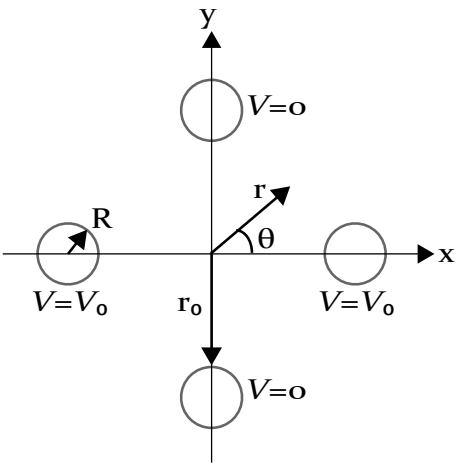

Figure 2.3: Definition of the cylindrical and cartesian coordinates for the description of the trapping potential. The electrodes are depicted as circles.

electrode radius R and r_0 is set to $R/r_0 = 1.146$ [53]. The boundary conditions impose a value of $C_0 = \frac{V_0}{2r_0^2}$ and $C_p = \frac{V_0}{2}$, which gives a potential for ion trapping:

$$\phi(x,y) = V_0 \frac{x^2 - y^2}{2r_0^2} + \frac{V_0}{2} \tag{2.5}$$

The applied voltage V_0 is split up in a part oscillating at angular frequency Ω and amplitude V and a DC offset U: $V_0 = U - V\ \cos(\Omega t)$. From this potential the equations of motion in this quadrupole field are deduced (where e is the charge and m the mass of the particle):

$$\begin{aligned} \ddot{x} + \frac{e}{mr_0^2}(U - V\ \cos(\Omega t))x = 0 \\ \ddot{y} - \frac{e}{mr_0^2}(U - V\ \cos(\Omega t))y = 0 \end{aligned} \tag{2.6}$$

These equations are known as the Mathieu equations. The stability parameters a and q are conventionally used to characterize the trapping conditions:

$$a = \frac{4eU}{mr_0^2\Omega^2}; \quad q = \frac{2eV}{mr_0^2\Omega^2} \tag{2.7}$$

On substituting $\Omega t = 2\tau$ this results in the custom form of the Mathieu equations:

$$\begin{aligned} \frac{d^2x}{d\tau^2} + (a - 2q\ \cos 2\tau)x = 0 \\ \frac{d^2y}{d\tau^2} - (a - 2q\ \cos 2\tau)y = 0 \end{aligned} \tag{2.8}$$

Floquet's theorem gives the solution to a differential equation of the form $\frac{d^2u}{d\tau^2} + Q(\tau) \times x = 0$, with $Q(\tau)$ a real function with period L. According to this theorem the function u can be written as:

$$u = e^{i\mu\tau} \times p_1(\tau) + e^{-i\mu\tau} \times p_2(\tau) \tag{2.9}$$

In this function $p_1(\tau)$ and $p_2(\tau)$ are periodic functions of τ with the same period L, and μ is a complex number. The periodic functions can be expressed in Fourier series, which leads to the equation:

$$u(\tau) = e^{i\mu\tau} \sum_{n=-\infty}^{n=+\infty} A_n e^{2in\pi\tau/L} + e^{-i\mu\tau} \sum_{n=-\infty}^{n=+\infty} B_n e^{2in\pi\tau/L} \tag{2.10}$$

In the case where $Q(\tau)$ is a symmetric function, there is a relation between the coefficients equal to $B_{-n} = D \times A_n$, with D a constant (this can be verified by filling in equation (2.10) in the differential equation). In combination with the period $L = \pi$ of the $\cos 2\tau$ term, the general solution to the Mathieu equation can be written as ($u = x, y$):

$$u(\tau) = \alpha e^{i\mu\tau} \sum_{n=-\infty}^{n=+\infty} C_n e^{2in\tau} + \beta e^{-i\mu\tau} \sum_{n=-\infty}^{n=+\infty} C_n e^{-2in\tau} \tag{2.11}$$

Where α, β and C_n are constants.

This equation can have stable ('trapped') and unstable solutions for both the x- and y-direction, and has to be stable both dimensions in order to trap the ions. In order to keep a finite amplitude for $t \to \infty$, it is necessary that μ is a real number, but not integer [54]. The values for a and q where this is the case are usually expressed in a stability diagram. For this case of an infinite linear Paul trap it is depicted in Fig. 2.4. In order to trap ions, the parameters a and q must be chosen such to stay in the region of this diagram where both the motion in x- and y-direction is stable.

To confine the ions in all three dimensions, an additional trapping field along the z-direction is necessary. This field is created by two electrodes carrying a DC field on the far ends of the z-axis. The trapping potential is usually designed to be

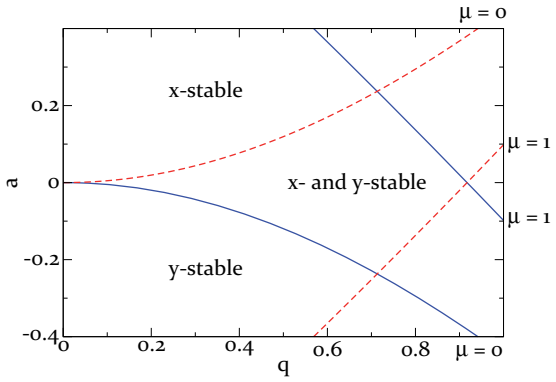

Figure 2.4: Schematic stability diagram for a linear ion trap in 2 dimensions. The ions are only trapped if the motion is stable in both the x- and y-direction.

approximately harmonic in the center, with a corresponding harmonic trapping frequency ω_z. Several geometries can be chosen for these so-called endcaps, and configurations including the use of rings, pins, and cylinders as these electrodes have been demonstrated.

2.1.3 The pseudopotential, secular- and micromotion

The equation of motion of a trapped particle can be solved approximately for $a, q \ll 1$. The forces in equation 2.8 are a combination of a static and an oscillating term. To solve the equation, the motion is divided into a fast oscillating trajectory ξ, which is due to the cosine term in the differential equation, and a slower motion X, so $x = X + \xi$. It is assumed that the amplitude of ξ is small compared to X. The Mathieu equation (2.8) can be written as:

$$\ddot{X} + \ddot{\xi} = (-\frac{a\Omega^2}{4} + \frac{q\Omega^2}{2}\cos(\Omega t))(X + \xi) \tag{2.12}$$

The assumptions mentioned above imply $\ddot{X} \ll \ddot{\xi}$, and $X \gg \xi$. In addition, on short timescales the motion is determined by the oscillating term:

$$\ddot{\xi} \approx \frac{q\Omega^2}{2}\cos(\Omega t)X \tag{2.13}$$

The function X is assumed to be static compared to ξ, so the above equation has the solution:

$$\xi = \frac{-q}{2}\cos(\Omega t)X \tag{2.14}$$

This part of the ion motion is known as micromotion, which is driven by the oscillating electric field. It can be put into equation 2.12 in order to solve for X, which leads to the following differential equation:

$$\ddot{X} = \frac{-a\Omega^2}{4}(X+\xi) - \left(\frac{q\Omega}{2}\right)^2 \cos^2(\Omega t)X \tag{2.15}$$

Because X is slow compared to ξ, the time average over one oscillation of ξ will give $< X >_\xi \approx X$. The calculation of this average for the total equation has the (approximated) result:

$$\ddot{X} = -\frac{a\Omega^2}{4}X - \frac{1}{2}\left(\frac{q\Omega}{2}\right)^2 X \tag{2.16}$$

This is an equation of the form of a harmonic motion $\ddot{x} = -\omega_{sec}^2 x$, with:

$$\omega_{sec} = \sqrt{\frac{a\Omega^2}{4} + \frac{1}{2}\left(\frac{q\Omega}{2}\right)^2} = \frac{\Omega}{2}\sqrt{a + \frac{1}{2}q^2} \tag{2.17}$$

The motion at this frequency is called secular or macromotion. The total trajectory of the ion is thus:

$$x = X + \xi = X_0 \cos(\omega_{sec} t)(1 - \frac{q}{2}\cos(\Omega t)) \tag{2.18}$$

The secular motion can be cooled [55], so the cooling conditions will eventually determine the amplitude X_0 for this motion. An example of the ion position over time is shown in Fig. 2.5 for the parameters of trap B (see section 2.3.2, $q = 0.2$ and $\Omega = 2\pi \times 2.6\,\mathrm{MHz}$).

The macromotion is the part of the motion that would occur in a harmonic potential Ψ of the form $e\Psi = \frac{1}{2}m\omega_{sec}^2 x^2$. This average potential provides a three-dimensional harmonic well for trapping of the particles, and is usually called the pseudopotential. Ideally, ions can be trapped in this potential until the limit where they reach the surface of the electrodes, which is at a distance r_0 from the trap center. The corresponding trap depth in the pseudopotential is thus $D = \frac{1}{2e}m\omega_{sec}^2 r_0^2$. For a potential with only an RF-component ($a = 0$), this leads to the expression $D = \frac{eV^2}{4mr_0^2\Omega^2}$. For example, in the first constructed linear Paul trap described in section 2.3.1 this depth is $D = 0.3\,\mathrm{eV}$ corresponding to a temperature of $3.5 \times 10^3\,\mathrm{K}$.

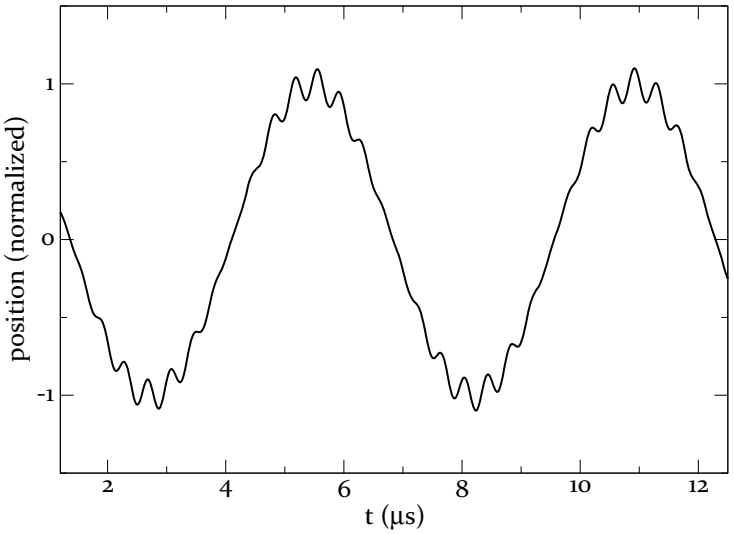

Figure 2.5: The ion motion in the trap, including both the macro- or secular motion (with the longer period) and the faster micromotion. The depicted trace is calculated for the parameters $q = 0.2$ and $\Omega = 2\pi \times 2.6\,\mathrm{MHz}$.

2.2 Cold trapped ions

2.2.1 Laser cooling

The technique of laser cooling was first introduced by Hänsch and Schawlow [3] and Wineland an Dehmelt [4]. The theory describing laser cooling depends on the frequency of the oscillation of the trapped ion ω_{ion} compared to the natural linewidth γ of the the transition used for cooling. The case for which $\gamma >> \omega_{ion}$ is called the heavy particle or weak binding limit (the situation in the experiments described in this thesis), while the other ($\gamma << \omega_{ion}$) is called the sideband-cooling or strong-binding limit [56]. In the case of the weak binding limit, the atom experiences many scattering events within one cycle, leading to a cooling mechanism as it is usually described for neutral atoms (as can for example be found in [57]): A laser which is slightly detuned below the frequency of a dipole-allowed transition is used for cooling of the particles. When the ion is moving towards this laser beam, the frequency of the light is shifted into resonance by the Doppler effect and there is a high scattering probability. When it moves away, the light is shifted away from resonance and this probability is reduced. When a photon is absorbed, the particle gets a 'momentum kick' from the light. Because the total

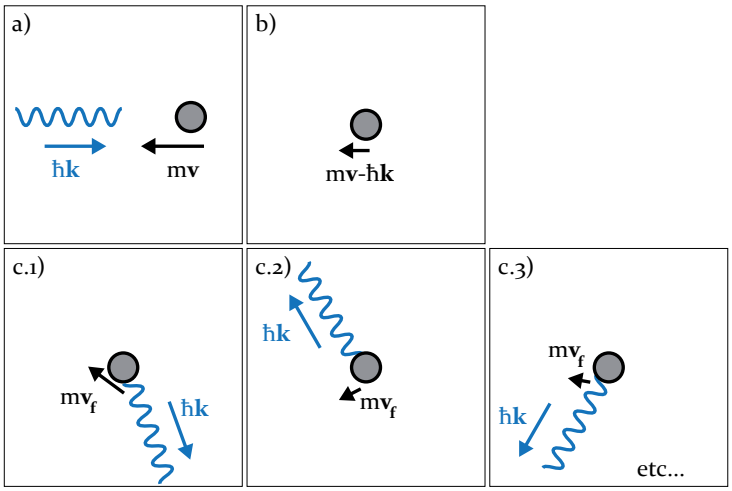

Figure 2.6: Schematic picture of the principle of laser cooling: a) An ion moving towards a red-detuned laser beam absorbs a photon. b) After the photon absorption the ion has a lower velocity in the x-direction due to momentum conservation. c) On emission of the photon, again momentum is transferred to the ion. A few options for single events are given in c.1), c.2) and c.3), where the final velocity v_f depends on the direction of the emitted photon in both direction and magnitude. Since the direction of this emission has a symmetric distribution, the average momentum transfer over many events is zero.

momentum is conserved, an ion moving towards the red-detuned beam will slow down. This momentum is transferred to a photon again when the particle decays back to the ground state (Fig. 2.6). However, the direction of the emission has a symmetric probability distribution. On averaging over many scattering events, there will thus be no net momentum transfer due to this emission. The net effect of the total scattering action is that the ion oscillation motion is damped, and thus the ion is cooled. Ultimately, this cooling process is limited by the linewidth of the transition and recoil energy

In order to further cool ions to their ground state of motion, resolved sideband cooling can be applied. This technique relies on the quantization of ion motion into quantized discrete energy levels, which can be resolved if the upper state lifetime is smaller then the trap oscillation frequency, so $\gamma < \omega_{trap}$. In this situation, the cooling laser can be tuned to a sideband of lower energy in order to extract energy from the system (Fig. 2.7). In this so-called Lamb-Dicke regime, the atom will usually decay without a change in vibrational quantum number [58], leading to an energy loss of $\hbar\omega_{trap}$. In this way, ions can be laser cooled almost entirely to the ground state of motion (ground state occupation of $> 99\%$ has been achieved

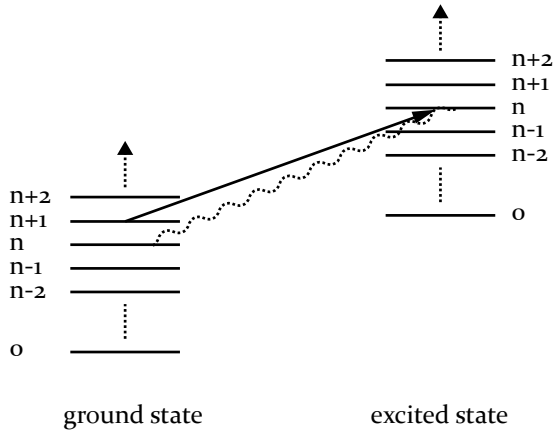

Figure 2.7: Resolved sideband cooling: Under the condition $\omega_{trap} > \gamma$, a sideband spectrum can be resolved, consisting of a central peak at the transition frequency (between states of equal n) and neighboring modes at an integer times the trap frequency. By setting the cooling laser to a lower sideband, the transition between states n+1 and n are driven (for arbitrary n). In the Lamb-Dicke regime, will usually be between states of equal vibrational quantum number [58], leading to a net energy loss of $\hbar\omega_{trap}$ per excitation.

[43]). More detailed information on resolved sideband cooling can be found in [58] or [59].

For the experiments described in this thesis, only Doppler cooling was applied. The effect of Doppler cooling can be derived quantitatively (following reference [60]) from the conservation of momentum $\vec{p}$ in a scattering event, for a particle with mass m, initial velocity $\vec{v}_i$, and final velocity $\vec{v}_f$ on absorbition of a photon with wavenumber $\vec{k}_{abs}$, followed by emission of a photon with wavenumber $\vec{k}_{em}$:

$$\Delta\vec{p} = m\vec{v}_f - m\vec{v}_i = \hbar\vec{k}_{abs} - \hbar\vec{k}_{em} \tag{2.19}$$

$$\Delta E_{kin} = \frac{1}{2}m\vec{v}_f^2 - \frac{1}{2}m\vec{v}_i^2 \tag{2.20}$$

Putting the $\vec{v}_f^2$ derived from equation 2.19 in equation 2.20 gives an expression for the change in kinetic energy ΔE_{kin} resulting in:

$$\Delta E_{kin} = \frac{\hbar^2}{2m}(\vec{k}_{abs} - \vec{k}_{em})^2 + \hbar(\vec{k}_{abs} - \vec{k}_{em}) \cdot \vec{v}_i \tag{2.21}$$

The change in kinetic energy due to motion in a single cartesian direction $j = x, y, z$ will be:

$$\Delta E_{kin,j} = \frac{1}{2}mv_{f,j}^2 - \frac{1}{2}mv_{i,j}^2 \tag{2.22}$$

All experiments described in this thesis apply laser cooling along a single axis, which is defined to be the z-axis corresponding to the coordinate system used in the description of the linear Paul trap. In this direction the momentum change due to absorption followed by re-emission is:

$$\Delta p_z = \hbar k_{abs} - \hbar k_{em,z} \tag{2.23}$$

So the kinetic energy change due to motion in the z-direction (where z can be replaced by x or y to express the kinetic energy due to motion in the other directions) will be given by:

$$\Delta E_{kin,z} = \frac{\hbar^2}{2m}(k_{abs,z} - k_{em,z})^2 + \hbar(k_{abs,z} - k_{em,z}) \times v_z \tag{2.24}$$

So for calculation of the cooling power of a laser beam along the z-axis, the direction of emission relative to the absorption (or in other words, the direction of recoil relative to the cooling laser axis) needs to be taken into account. The direction of the emitted photons will have an angular distribution $P_{em}(\theta)$, where the angle θ is the angle between the polarization of the absorbed photon and the emission direction. The total probability of emission equals unity, since all absorbed photons will eventually be emitted again: $\int P_{em}(\theta)d\Omega = 1$. The emission of photons in opposite directions is equally probable, therefore P_{em} is symmetric in $\vec{k}_{em}$. As a result the contribution of terms linear in $\vec{k}_{em}$ average out to zero. For a dipole allowed $\Delta m = 0$ transition as used for laser cooling of calcium ions, the normalized emission probability is given by $P(\theta) = \frac{3}{8\pi}\sin^2\theta$.

The laser detuning (which is of the order of MHz) is orders of magnitude smaller than the (optical) transition frequency, so the k-vectors of the absorbed and emitted light are approximately equal in magnitude: $k_{abs} \approx k_{em} \equiv k$. Combining these k-vector properties with the angular distribution of the emitted photons, the average change in energy along the z-direction per photon is given by:

$$< \Delta E_{kin,z} > = \int P_{em}(\theta)\Delta E_z \, d\Omega \tag{2.25}$$

$$= \int \frac{3}{8\pi}\sin^2\theta \times \{\frac{\hbar^2 k^2}{2m}(1 - \sin\theta\cos\phi)^2 + \hbar k v_z\} d\Omega \tag{2.26}$$

$$= \frac{\hbar^2 k^2}{2m}(1 + \frac{2}{5}) + \hbar k v_z \tag{2.27}$$

The above equation represents the average change in kinetic energy for a single absorption and emission process. The total rate of change in kinetic energy is given by the change per photon times the photon scattering rate γ_s, so:

$$\frac{dE_k}{dt} = \gamma_s < \Delta E_{kin} > \tag{2.28}$$

The scattering rate for a two-level system is equal to $\gamma_s = \gamma\rho_{22}$, where ρ_{22} is the steady state population of the upper level, which can be calculated from the optical Bloch equations. It is given by [61]:

$$\gamma_s = \frac{s_0\gamma}{2}\frac{\gamma^2}{(1+s_0)\gamma^2 + 4\delta^2} \tag{2.29}$$

Where the saturation factor $s_0 = I/I_s$, and I_s the saturation intensity. This factor can also be written as $s_0 = 2|\Omega_R|^2/\gamma$, with Ω_R the Rabi frequency. The detuning from resonance is represented by δ. For an atom moving with a velocity $\vec{v}$, a laser frequency ω_{laser} and an atomic resonance frequency ω_0 this detuning is equal to $\delta = \omega_{laser} - \omega_0 + \vec{k}\cdot\vec{v} \equiv \Delta + \vec{k}\cdot\vec{v}$. Thus for a negative detuning $\Delta < 0$, a particle moving towards the laser beam (with small enough velocity so $\vec{k}\cdot\vec{v} < -\Delta$) will see the photon energy shifted closer to resonance, and thus have a higher scattering rate. A particle moving in the opposite direction will have a lower scattering rate since it is Doppler-shifted away from resonance.

Combining expressions (2.27), (2.28) and (2.29), the rate of change in kinetic energy is given by:

$$\frac{dE_k}{dt} = \frac{s_0\gamma}{2}\frac{\{(\hbar^2k^2/2m)(1+f_s) + \hbar\vec{k}_{abs}\cdot\vec{v}\}\gamma^2}{(1+s_0)\gamma^2 + 4\delta^2} \tag{2.30}$$

By explicitly writing δ and reorganizing, the following expression is obtained:

$$\frac{dE_k}{dt} = \frac{s_0\gamma}{2(1+s_0)}\frac{1}{1+\frac{4}{(1+s_0)\gamma^2}(\Delta+kv_z)^2}(\frac{\hbar^2k^2}{2m}\frac{7}{5} + \hbar kv_z) \tag{2.31}$$

For small velocity and $s_0 \gg 1$ the central term can be approximated by:

$$\frac{1}{1+\frac{4}{(1+s_0)\gamma^2}(\Delta+kv_z)^2} \approx 1 - \frac{4}{(1+s_0)\gamma^2}(\Delta+kv_z)^2 \tag{2.32}$$

In addition, for small velocities the $(kv_z)^2$ term can be neglected, which gives an expression for the change of kinetic energy:

$$\begin{aligned}\frac{dE_k}{dt} = \frac{s_0\gamma}{2(1+s_0)}\{&\frac{\hbar^2k^2}{2m}\frac{7}{5}(1 - \frac{4\Delta^2}{(1+s_0)\gamma^2}) \\ &+ \hbar kv_zC_v - \frac{8\hbar\Delta}{(1+s_0)\gamma^2}v_z^2\}\end{aligned} \tag{2.33}$$

Where C_v contains only expressions which are independent of the velocity. The above equation is valid for particles moving with a certain single velocity. The

ion cloud which is laser cooled, will have a (usually symmetric) velocity spread. Hence, cooling over a large number of particles will result in an average energy change per ion $< \frac{dE_k}{dt} >_v$ (where the v-subscript denotes averaging with respect to the velocity distribution). Assuming that for averaging over many particles or events $P(v) = P(-v)$, the average change in kinetic energy then becomes:

$$< \frac{dE_k}{dt} >_v = \frac{s_0\gamma}{2(1+s_0)}\{\frac{\hbar^2k^2}{2m}\frac{7}{5}(1 - \frac{4\Delta^2}{(1+s_0)\gamma^2}) - \frac{8\hbar\Delta}{(1+s_0)\gamma^2} < v_z^2 >_v\} \tag{2.34}$$

In the approximation that there is no external ion heating, a steady state will be reached for $< \frac{dE}{dt} >_v = 0$, which gives an expression for $< v_z^2 >_v$ reading:

$$< v_z^2 >_v = \frac{\hbar}{4m}\frac{7}{5}\{(1+s_0)\frac{\gamma^2}{4\Delta} - \Delta\} \tag{2.35}$$

The kinetic energy that can thus be obtained for motion in the z-direction, by cooling with a laser beam on this axis, using a dipole allowed $\Delta m = 0$ transition (as is the case throughout this thesis) is equal to:

$$< E_k > = \frac{1}{2}m < v_z^2 > = \frac{7\hbar}{40}\{(1+s_0)\frac{\gamma^2}{4\Delta} - \Delta\} \tag{2.36}$$

For different cooling laser directions the kinetic energy due to motion in the other two dimensions can be calculated in a similar way, as is described in [60].

In this situation where the ions are only cooled along the z-axis, the kinetic energy in the x- and y-direction will be changed only with the recoil energy for each scattering event. This kinetic energy change averages out to zero over many absorptions and emissions, so no direct cooling is observed in these directions. However, the three dimensions in an ion trap are coupled. The efficiency of this coupling depends on the trap anisotropy parameter $\alpha = (\omega_z/\omega_r)^2$. For values of α close to unity, there is efficient thermalization between the different directions. For more 2-dimensional shapes in the trap on the other hand, the temperature to which the ions are cooled in the orthogonal dimensions can differ by two orders of magnitude from the temperature in the cooling direction [62]. For the traps used in our experiments, with $\alpha = 0.9$ for trap A and $\alpha = 0.1$ for trap B (see Section 2.3), and the Coulomb coupling leads to cooling in all three dimensions.

An example of an experiment cooling with a laser beam on the trap axis, is described in Chapter 7. The cooling laser has a power of $P = 0.1\,\mathrm{mW}$, which is focused to a beam width of $w_0 = 32\,\mu\mathrm{m}$. The magnitude of the electric field is then given by $E = 6.8\,\mathrm{kV/m}$. The Rabi frequency $\Omega_R = \mu_{21}E/\hbar = 1.14 \times$

$10^9\,\mathrm{s}^{-1}$*. Putting these numbers into equation (2.36), with a detuning of $\Delta = \gamma/2 = 2\pi \times 11\,(3)$ MHz, results in a minimum temperature of $T = 13\,(4)$ mK. This number agrees well with the temperature of $T = 14$ mK deduced from the observed linewidth.

2.2.2 Sympathetic cooling

Besides the option of directly laser cooling ions in the trap, other ions can be cooled by a laser-cooled ion through their mutual Coulomb interaction. This method is particularly useful for ions that are difficult to lasercool directly. This mechanism of sympathetic cooling was first suggested [5] and demonstrated [64] for trapped ions in a Penning trap. Sympathetic cooling in a Paul trap was first observed with an (unknown) non-fluorescing ion in a trap containing $^{198}Hg^+$ [65]. Sympathetic cooling significantly expands the range of ions that can be cooled, since there are no requirements on the energy level structure of the ion as there is for laser cooling. In addition, the mechanism of sympathetic laser cooling can be advantageous in precision spectroscopy and quantum computation. The reason for this is that cooling lasers with a small detuning relative to relevant energy levels can cause coupling between these energy levels (and corresponding Stark shifts). These shifts are reduced if the lasercooled and the probed ion are of different species.

The mass ratio that can be sympathetically cooled with a single ion species is limited, and a critical condition $m_{sc}/m_{lc} > 0.5$ was derived by Baba and Waki [66] for non-crystallized ions, under the assumption that long-range Coulomb interactions do not influence the ion trajectory. These ratios change for an ion crystal. For example, using 60 calcium coolant ions ($m = 40$u) to cool 20 ions of another species, particles with a mass down to ~ 15 u such as Mg^+ and NH_3^+ can be cooled to crystallization [67]. The largest observed mass difference that has been sympathetically cooled is presented in [68], demonstrating that fullerene ($m = 720$ u) can be cooled using magnesium ($m = 24$ u) to a temperature of $T = 14$ K. For large clouds with substantial RF heating, the temperature of the sympathetically cooled ion will be a few times higher than the laser-cooled ion temperature, where the exact ratio depends on the mass ratio between the ions [69]. Such larger crystals have also been observed, for example by Ostendorf *et al.* [70], in an experiment sympathetically cooling large molecular ions (Alexa Fluor 350, now denoted as AF) using $^{138}Ba^+$. The observed temperature ratio of $T_{Ba}/T_{AF} \sim 4$ at a mass ratio of $m_{Ba}/m_{AF} \sim 3$ agrees with the ratios predicted by [69]. The range of ions that can be sympathetically cooled can be extended to

*The electric dipole moment is approximatly $\mu_{21} = 1.75 \times 10^{-29}$ Cm, calculated from the Einstein A-coefficient [63]

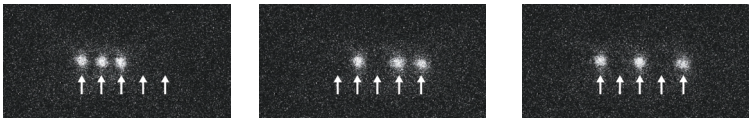

(a) (b) (c)

Figure 2.8: Three images for a trap filled with three calcium ions and two other (possibly manganese) ions. The dark ions are sympathetically cooled by the laser cooled calcium, but the ions are still warm enough to hop between sites. The arrows indicate the five ion positions.

higher mass ratios by changing the charge state of the ions [71]. For very small crystals (where all ions reside on the axis of a linear trap) sympathetic cooling can be extremely efficient. For example, in an experiment using a $^{9}Be^{+}$ and a $^{24}Mg^{+}$ ion, each ion could be cooled almost completely to the ground state of motion by laser cooling the other [72]. This observation agrees with the theory, as is described in [73], and specifically for the application to quantum information as presented in [74] and [75].

Sympathetic cooling was also observed in our experiments using trap B. To create a crystal containing both the cooling ion and the particle to be sympathetically cooled, a string of calcium ions consisting of only a few ions was loaded into the trap. After loading of the ion trap, a second oven containing manganese particles was turned on, for a sufficient period to observe dark ions in the trapping region (Fig. 2.8). These ions may be manganese ions, where the neutral manganese can be ionized through charge transfer with the trapped calcium (this effect is described in [76]). However, also the creation of calcium hydride or another impurity from the oven is a possibility.

2.2.3 Heating rates

The oscillating trapping potential can have a significant heating effect on the trapped ions, especially for an ion cloud extending far from the trap axis. The ions experience a force determined by both the overall trapping force and their mutual Coulomb interaction. If only these two effects are considered, for the i-th ion the equation of motion will be given by:

$$\frac{d^2\vec{r}_i}{dt^2} = \frac{1}{m_i}(\vec{F}_{trap,i} + \sum_{i \neq j} \frac{k_c e^2}{r_{ij}^2}\hat{r}_{ij}) \tag{2.37}$$

where $k_c = 1/4\pi\epsilon_0$ is the Coulomb constant, $\vec{F}_{trap}$ is the force due to the trapping field and $\hat{r}_{ij}$ is a unit vector between two ions i and j.

In general, to calculate the corresponding heating rates, computer simulations are necessary. These have been performed for several cases: see e.g. [77] for a string and [78] for a cloud in a hyperbolic ion trap, [79] for simulations in a linear trap with periodic boundary conditions, [80] for large crystals in a linear Paul trap and [81] for a large planar crystal. In [62] the influence of 1D laser cooling and coupling to other dimensions is described. A model for the heating rate for large trapped ion clouds in the presence of laser cooling can be found in [82]. The heating rate (for low temperatures) follows a power law dependence both in the temperature [79, 80] and in the applied trapping voltage [79].

For a few specific cases, it is quite easy to understand the heating rate will be small. For a single trapped ion the dynamics simply follow the Mathieu equation (2.8), which has a time-dependence only through functions oscillating in time, so that the average kinetic energy will remain constant and no heating occurs.

In the case of a string of ions on the axis of the trap (where there is no net electric field), the average trapping force is constant. In addition, $r_{i,j}$ does not change on average, since the ions will oscillate around an equilibrium position in a harmonic potential. Because the work that is done by the RF field on one ion is $W = \int \vec{F}_{tot} \cdot d\vec{x} = \int m d^2\vec{r}_i/dt^2 \cdot d\vec{x}$, there is on average no work done by the trapping field, and for a string of cold, trapped ions the heating rates will be negligible too.

For an extended ion crystal, the ions will undergo heating by the RF field. However, from equation (2.37) it follows that for large ion separation, the Coulomb force reduces to zero, and hence does the heating rate. This is also observed in the segmented Paul trap (trap B), where even without active cooling ions could be stored overnight. So when the ions are heated by the RF-field, the separation between them increases, until a point is reached where no more heating occurs. For the other extreme, a very cold ion sample where v reduces to zero, rewriting the work done by the field with the formula $W = \int \vec{F}_{tot} \cdot \vec{v}\, dt$ shows that also in this case the heating rate diminishes.

An additional effect which is not considered here is the heating of the trapped ions by trap imperfections influencing the particle motion, such as patch potentials and a phase difference between the electrodes. A detailed description of these effects can be found in [55].

2.2.4 The ion crystal

The shape of a string or larger crystal of trapped ions is determined by the balance between the overall trapping potential and the Coulomb interaction between trapped ions. Assuming that the ion string is more strongly bound in the radial than in the axial direction (so that the ions will form a string on the trap axis), the potential energy of the chain will be given by:

$$V = \sum_{n=1}^{N} \frac{1}{2} m\omega_z^2 x_n^2 + \sum_{n=1}^{N} \sum_{m>n}^{N} \frac{q^2}{4\pi\epsilon_0} \frac{1}{|x_m - x_n|} \tag{2.38}$$

In this equation ω_z is the axial trapping frequency and $x_{m,n}$ are the positions of the trapped ions. The equilibrium positions of the ions will be situated in the minima of the potential well:

$$\left[\frac{\partial V}{\partial x_m}\right]_{x_m = x_m^{(0)}} = 0 \tag{2.39}$$

For generalization of the problem, a dimensionless parameter $u_n = x_n^{(0)}/l$ can be introduced, with:

$$l^3 = \frac{q^2}{4\pi\epsilon_0 m\omega_z^2} \tag{2.40}$$

Then equation (2.39) can be rewritten as a set of coupled equations [83]:

$$u_m - \sum_{n=1}^{m-1} \frac{1}{(u_m - u_n)^2} + \sum_{n=m+1}^{N} \frac{1}{(u_m - u_n)^2} = 0 \tag{2.41}$$

This can be solved (numerically for N>3) to give the equilibrium spacings for an ion string [83]. As an example, the ion strings as described in Chapter 7 consist of 10 ions. According to [83] then the spacing between the ions in the center of the trap should be $0.56 \times l$, and the distance between adjacent ions increases on moving away from the center. For the calcium ions in this trap, the axial oscillation frequency is $\omega_z \approx 2\pi \times 60$ kHz (see section 2.3.2). The corresponding calculated equilibrium distance in the center of the trap is $\Delta x = 16\,(2)\,\mu$m, which is in good agreement with the observed distance of $\Delta x = 14\,(2)\,\mu$m (Fig. 2.9). For longer strings of ions, the distance between the ions in the center can be approximately calculated by the formula $u_{min} \approx \frac{2.018}{N^{0.559}}$ [83]. For trap A (with an axial trapping frequency of $\omega_z \approx 2\pi \times 47$ kHz) the ions in the center should be spaced by $17\,(1)\,\mu$m, which is in reasonable agreement with the observed distance of $21\,(2)\,\mu$m (Fig. 2.10).

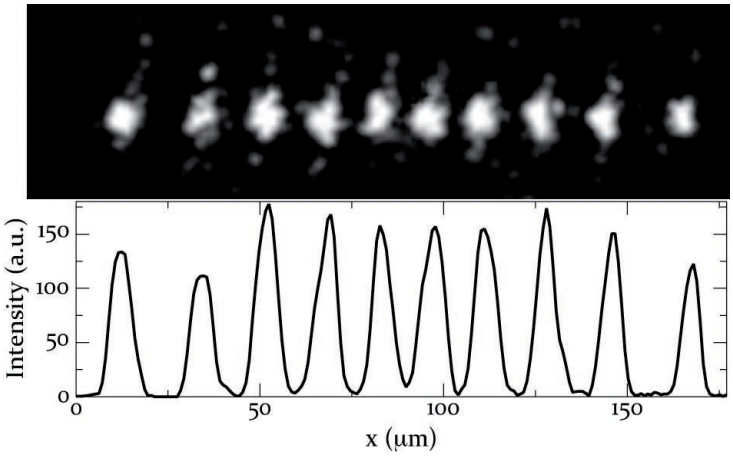

Figure 2.9: A string of ten ions as observed in ion trap B. The trace (lower part) consists of data taken from the (smoothened) picture (upper part). The numbers indicated on the x-axis are an approximation, calculated for a magnification of $M = 9$ in the optical system.

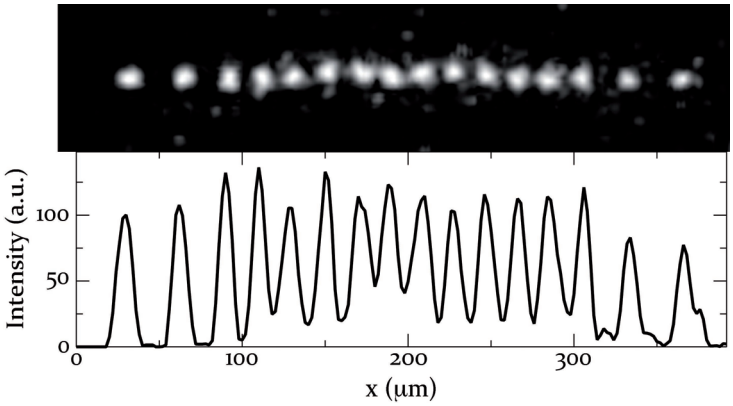

Figure 2.10: A string of twelve ions as observed in ion trap A. The trace (lower part) consists of data taken from the (smoothened) picture (upper part).

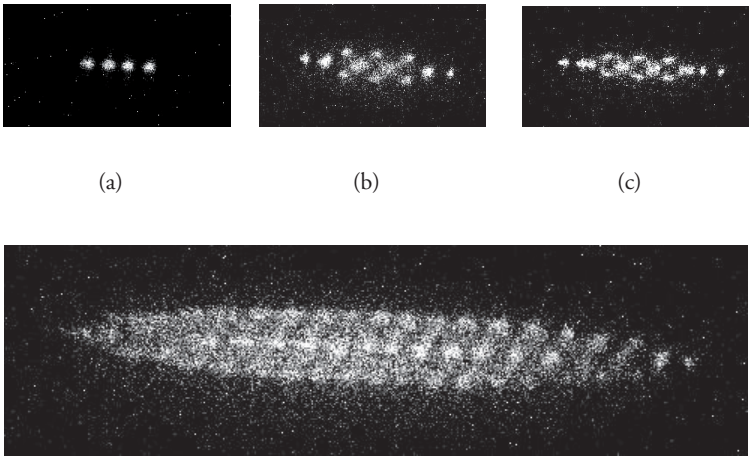

(a) (b) (c)

(d)

Figure 2.11: Different ion configurations, depending on the number of trapped ions, changing from a string (for low number of ions) in (a) to helices in (b) and (c), and forming a three-dimensional crystal for high ion numbers in (d).

The shape of the ion crystal changes with the ratio between the radial and the axial trapping frequency. The arrangement of the ion cloud depends only on the anisotropy parameter $\alpha = \omega_z^2/\omega_r^2$. At small α and small numbers of ions the ions will line up as a string on the trap axis. On increasing the anisotropy paramater or the number of ions, a "zig-zag" structure will be formed. The onset of this phase transition occurs at the value α_i, which experimentally follows a power-law behaviour [84]:

$$\alpha_i = cN^{\beta} \tag{2.42}$$

The values for c and β in equation 2.42 were experimentally determined and theoretically verified to be at $c = 3.2$ and $\beta = -1.8$ [85]. Some ion crystal configurations for different ion numbers (at constant ω_z and ω_r) is shown in Fig. 2.11.

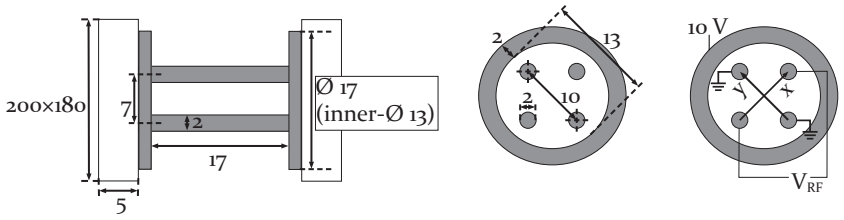

(a) Front view of the ion trap A

(b) Side view of the ion trap A

(c) Voltage applied to the ion trap

Figure 2.12: Schematic view of the ion trap A, distances are given in millimeters.

2.3 Experimental setup

2.3.1 Trap A: Unsegmented linear Paul trap, with ring-shaped endcaps

For the experiments described in this thesis, two different types of linear Paul traps are used. The first trap, used in the experiments described in Chapter 5 and 6, has a relatively simple design. It consists of four cylindrical rods for radial confinement, and two rings to provide trapping along the axis (Fig. 2.12). The rods are placed at a distance $r_0 = 4$ mm from the trap axis. The two rings that are mounted at the end of these electrodes are 17 mm apart and have a diameter of 15 mm. The ring electrodes carry a voltage of $V_{DC} = 10\,\text{V}$. The radio frequency (RF) voltages for radial confinement are supplied by an Agilent Arbitrary Waveform Generator (33120A), which provides a sinusoid with a peak-to-peak voltage of $V = 5.5\,\text{V}$ at a frequency $\Omega = 2\pi \times 3.3\,\text{MHz}$. This sine wave is resonantly upconverted using a helical resonator (see section 2.3.3) to apply $V_0 = 60\,\text{V}$ to the trap electrodes. The stability parameter for these trapping conditions is $q = 0.04$ and the corresponding secular trapping frequency $\omega_{sec} = 2\pi \times 50\,\text{kHz}$. A small stability parameter ($q << 1$) is chosen in order to reduce RF heating [79, 86].

The (instantaneous) trapping potential on the x- and the y-axis was calculated using a Laplace calculator (SIMION), and is shown in Fig. 2.13. The trapping potential is harmonic in the center of the trapping region, but deviates on moving away from $x = 0$. Due to the small diameter of the electrodes compared to the distance r_0 to the center of the trap, a relatively large anharmonic component is

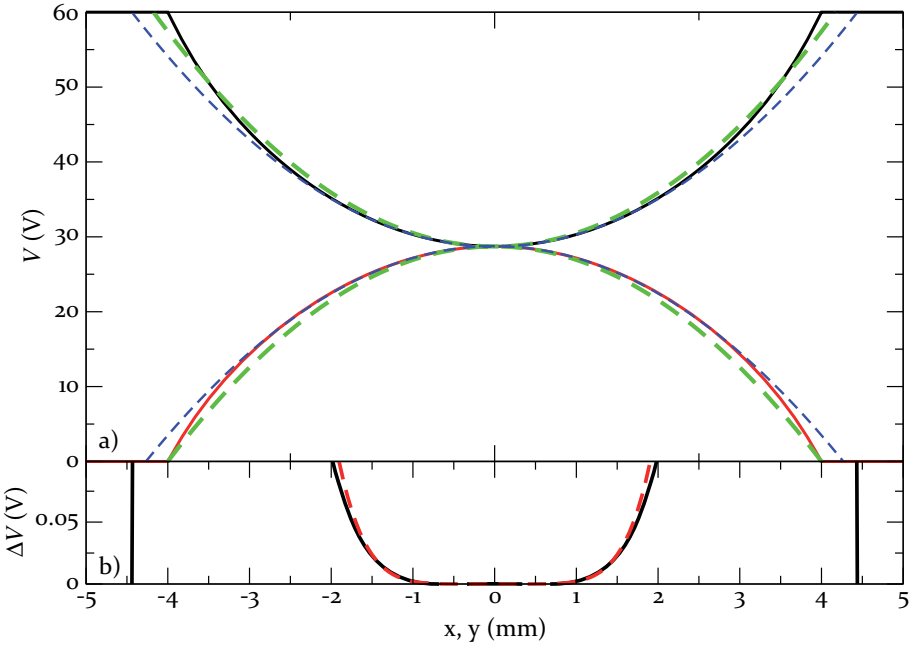

Figure 2.13: a) The instantaneous trap potential in trap A, both along the axis with the electrodes at $V = 60\,\mathrm{V}$ (upper curve) and along the axis with the grounded electrodes (lower curve). Also shown are the curves for the theory from section 2.1.2 (larger dash), and a harmonic fit (smaller dash). b) The difference between the simulated curve and the harmonic fit (solid curve), including an x^6-fit to the data.

expected. In the lower part of Fig. 2.13 the deviation from a harmonic potential is shown. The corresponding fit shows that this graph follows an x^6-behaviour, which is the next order in the expansion of the trapping potential.

The average potential along the axis is plotted in Fig. 2.14. In this dimension the potential in the center is also harmonic in a first order approximation. A harmonic fit to the central region yields a position-dependent voltage of $V(0,0,z) = 0.018\,\mathrm{V/mm^2} \times z^2 + 0.63\,\mathrm{V}$. Assuming a potential of the form $V = \frac{1}{2}\frac{m\omega_z^2}{e}z^2 + V_C$, this corresponds to an axial trapping frequency of $\omega_z = 2\pi \times 47\,\mathrm{kHz}$.

The fluorescence from ions in the trap is collected with a $f = 25\,\mathrm{mm}$ lens (diameter of 25 mm). The open structure of the ion trap allows for the collection of light over a large solid angle of approximately 0.2π sr, which in turn makes high count rates possible. Further details on the imaging of the ion fluorescence can be found in section 2.3.6.

To be able to also detect non-fluorescing ions, a Channel Electron Multiplier

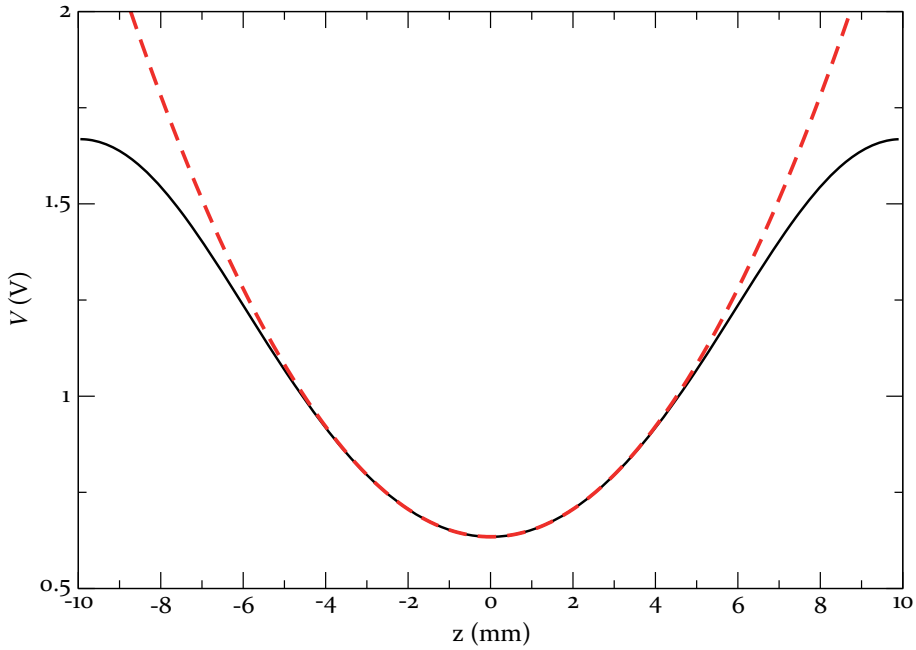

Figure 2.14: The average potential on the axis of trap A (solid curve). The central part of the trapping potential is harmonic (dashed curve), fitted with the function $V = 0.018V/\mathrm{mm}^2 \times x^2 + 0.63V$.

(CEM) was mounted at a distance of $\sim$ 1.5 cm from the ion trap with an extractor grid mounted right in front of it. Using a pulsed high voltage on this grid, ions are extracted from the trap, and then detected on the CEM (Fig. 2.15). In order to avoid coupling between the RF-trapping potential and this fast switching high voltage, the electrodes providing these voltages are connected to the voltage supply using semi-rigid coaxial cable.

The trap is mounted inside a vacuum chamber, which is evacuated to a pressure of $p = 2 \times 10^{-9}$ mbar. Under these vacuum conditions, the lifetime of the ions in trap A is limited to approximately 10 minutes due to collisions with background gas (Fig. 2.16).

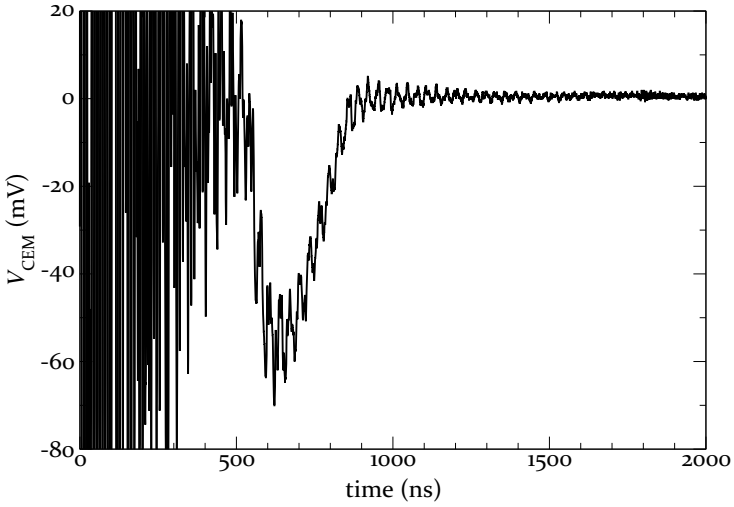

Figure 2.15: An example of the signal recorded on the Channel Electron Multiplier after photo-ionization in trap A. At 0 ns, an extraction pulse is applied to the grid mounted underneath the ion trap. The high amplitude oscillations in the first 500 ns are caused by coupling of the fast kV pulse on this grid to the CEM, as are the fast oscillations that are recorded for later times. The large negative signal centered at around 650 ns is due to the extracted calcium ions.

2.3.2 Trap B: Segmented linear Paul trap

The second trap that was built, is a segmented linear Paul trap (Fig. 2.17, 2.18 and 2.19). In this trap, the ions are trapped radially using four cylindrical electrodes with a diameter of 8 mm, at a distance to the trap center of $r_0 = 3.5$ mm. To accomplish confinement along the axis, the cylinders are differently segmented: Two electrodes are undivided and consist of one 60 mm long piece. The other two electrodes are segmented into five parts. The 12 mm long segments are separated by 100 μm. The ions can be trapped at the central segment, while an endcap potential is put on the adjacent electrodes. In addition, two separate trapping regions can be created in this trap, by putting DC voltages on electrode one, three and five.

The RF trapping voltages for this ion trap are resonantly upconverted with a helical resonator consisting of a doubly wound coil (see section 2.3.3). The used trapping voltage was $V_{RF} = 150$ V at a frequency $\Omega = 2\pi \times 2.6$ MHz. These parameters correspond to $q = 0.2$ and $\omega_{sec} = 2\pi \times 202$ kHz. The helical resonator output is connected to the trap via a cylindrical waveguide, with the inner conduc-

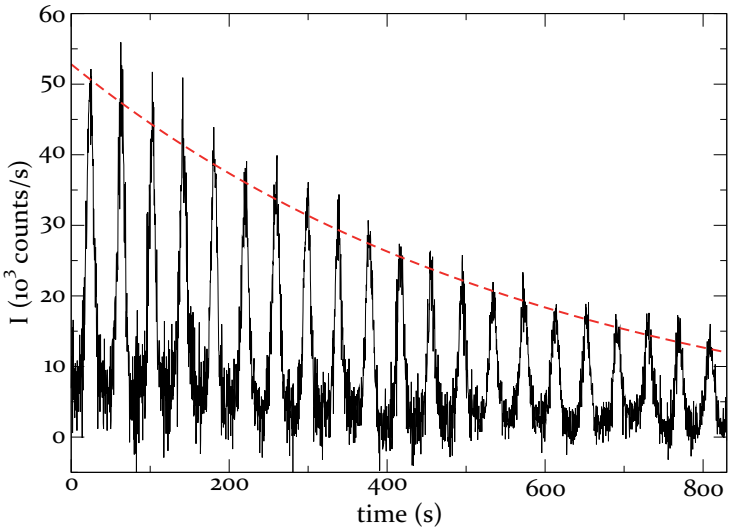

Figure 2.16: The fluorescence as measured in a scan with the frequency comb laser over the $4s\,^2\mathrm{S}_{1/2} - 4p\,^2\mathrm{P}_{3/2}$-transition, showing a decay in amplitude due to the loss of ions in the trap (continuous line). A line fitted to this exponential decay is also shown, corresponding to a lifetime of 10 minutes (dashed line).

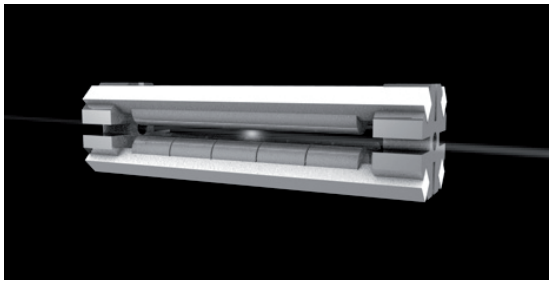

Figure 2.17: Trap B: Segmented ion trap.

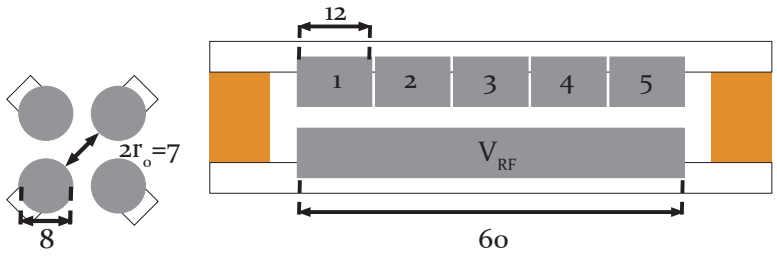

(a) Front view of the ion trap

(b) Side view of the ion trap. A voltage of $V = 10\,\mathrm{V}$ is put on electrodes 1,2,4 and 5, while electrode 3 is connected to ground. The RF-voltage is applied to the long electrode. The voltages on diagonally facing electrodes are identical.

Figure 2.18: Schematic view of the segmented ion trap B, distances are given in millimeters. The set of segments shown in the side view is located above the electrode out of one piece. The other electrodes have the opposite configuration.

tor consisting of two parallel copper bars. These inner conductors are separated by a sheet of Kapton foil for insulation. The conductors are thus capacitively coupled through their construction, and an additional capacitor of $C = 1\,\mathrm{nF}$ is mounted between the conductors in order to prevent phase shifts over the leads. The used endcap voltage is $V_{ec} = 10\,\mathrm{V}$ on electrodes 2 and 4. The voltages supplied to the DC electrodes are filtered using low-pass RC-filters with a cutoff frequency of $\omega_{co} = 2\pi \times 1.6\,\mathrm{kHz}$. Such a filter prevents that the DC-electrodes pick up the oscillation frequency of the trapped ions, which can transport and reflect over the leads and add an additional out-of-phase oscillation to the trapping potential, causing heating. Two RC-filters are used to filter the supplied voltage: one inside the vacuum (close to the electrodes) in order to prevent reflections over the leads in the chamber, and one outside for additional filtering.

The (instantaneous) potential for this trap configuration was simulated in SIMION, for which the result is shown in Fig. 2.20. Due to the chosen ratio $R/r_0 = 1.14$, which is close to the ideal ratio for a harmonic trap of $R/r_0 = 1.146$, the potential closely follows a harmonic behavior which matches the trap with infinite electrodes described in section 2.1.2 very well. However, the axial potential is much less harmonic compared to trap A due to the geometry of the endcaps, as can be seen in Fig. 2.21. The fitted curve of $V(0,0,z) = 0.03\,\mathrm{V/mm^2} \times z^2 + 0.2\,\mathrm{V}$ corresponds to an axial trapping frequency of $\omega_z = 2\pi \times 6 \times 10\,\mathrm{kHz}$.

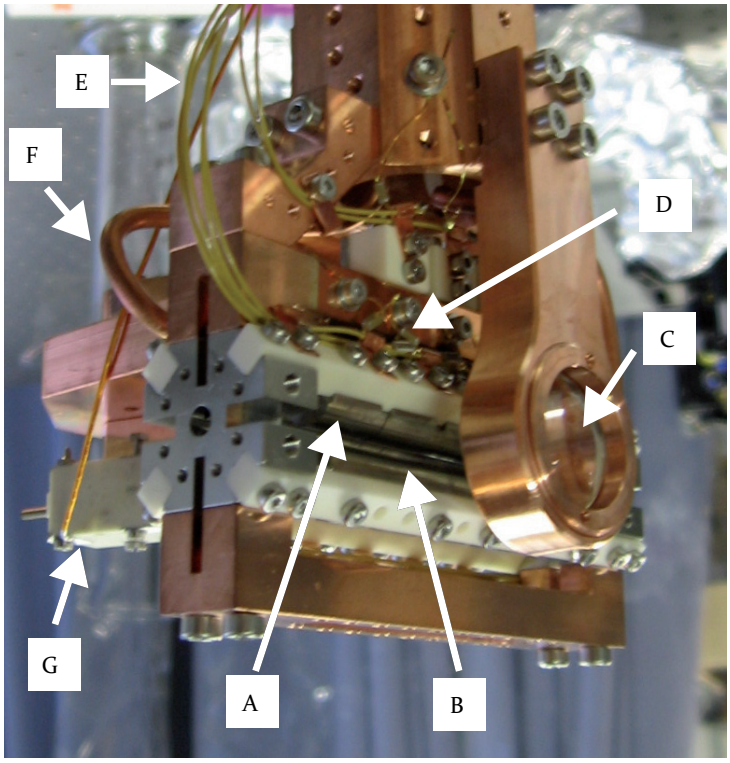

Figure 2.19: Photograph of the segmented, mounted ion trap B. A=DC segments, B=RF electrode, C=lens, D=RC filter circuit, E=Connections DC electrodes, F=Connection RF electrode, G=CEM.

The trap is also equipped with excitation electrodes, for resonant excitation of selected masses (a feature which was not used for the experiments conducted in this thesis). These electrodes consist of molybdenum plates mounted in a position parallel to the trap axis, but placed slightly above the trap. These electrodes can be used to identify dark ions, or to eject unwanted species (such as calcium hydride, formed by collisions with background gas) from the trap.

As for trap A, next to trap B a CEM is mounted for detection of ions. This CEM is mounted at a distance $\sim$ 5 cm from the trapping region, behind a grid in order to extract the ions. Due to the more closed configuration compared to trap A and the larger distance to the trapping region, for trap B the RF-voltage was switched off completely in order to extract the ions from the trapping region.

In trap B, a chamber pressure of 10^{-11} mbar was achieved. The lifetime under

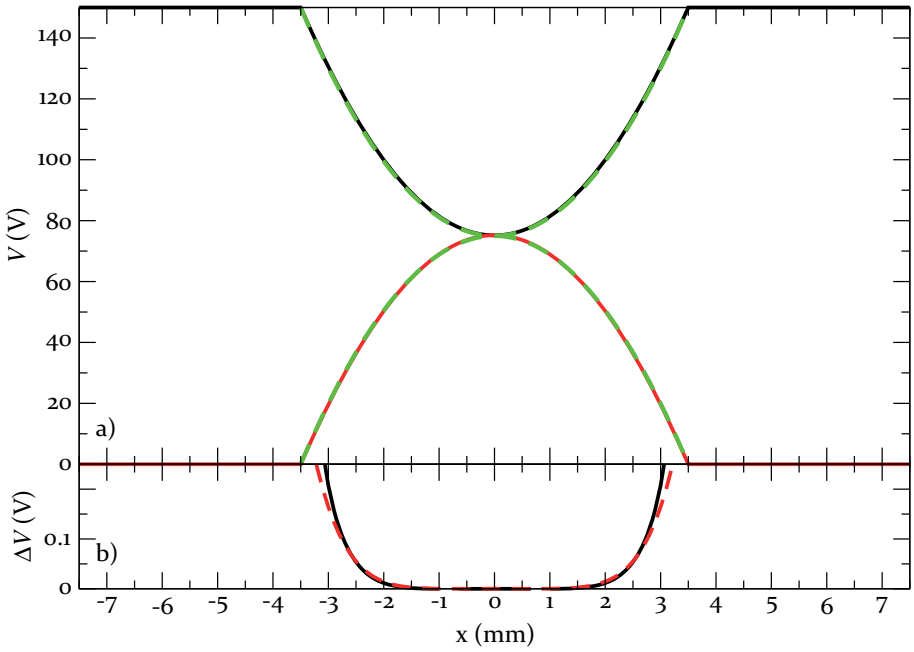

Figure 2.20: a) The trapping potential in the center of the trap for a configuration with $V = 150V$ on two of the electrodes, for both the axis along the electrodes at high voltage (upper curve) and along the axis on which the grounded electrodes are located (lower curve). The dashed line indicates the curve as predicted for the ideal infite trap described in section 2.1.2. $r_0 = 3.5\,\mathrm{mm}$, $R = 4.0\,\mathrm{mm}$. b) The difference between the simulated trapping potential, and a fitted harmonic potential (solid curve) and a corresponding x^6-fit (dashed curve).

these vacuum condition was measured to be over 8 hours, where the limit is set by the duration of the measurements.

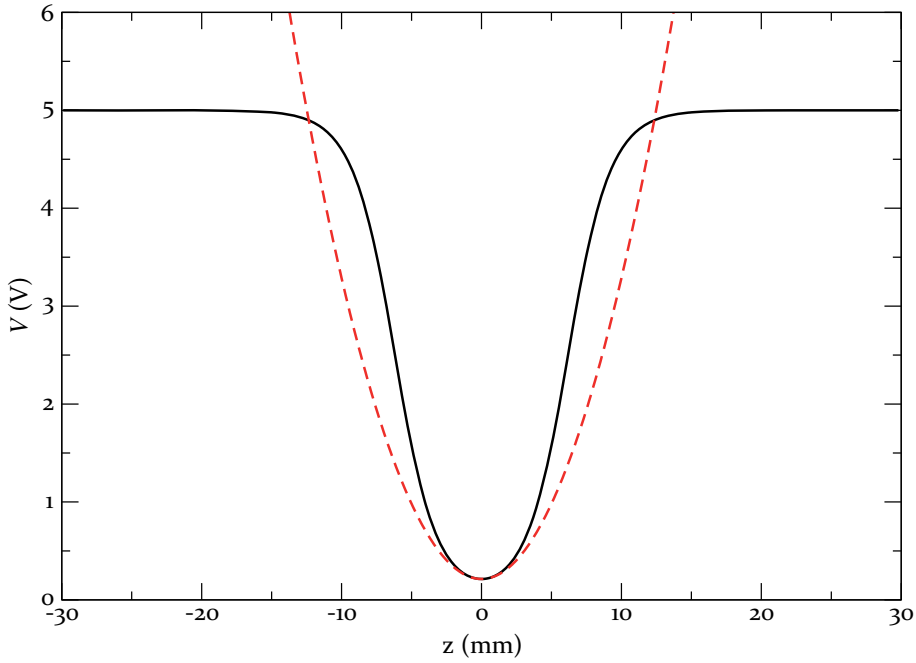

Figure 2.21: The average trapping potential along the axis of the ion trap B (solid curve) and a corresponding harmonic fit (dashed curve) to the function $V = 0.03V/\mathrm{mm}^2 \times z^2 + 0.2V$.

2.3.3 Helical resonators

A helical resonator consists of an inductor inside a conducting shield. This combination forms both an inductance and a capacitance, and is as such a resonant LC-circuit. The sine waves used for generating the RF trapping potential are produced by an 80 MHz arbitrary waveform generator (Agilent 33120A). Since the generator can only provide a peak-to-peak voltage of $V_{pp} = 10\,\mathrm{V}$, the signal is resonantly upconverted by a helical resonator. This method has the additional advantage over an RF amplifier that the voltage provided to the electrodes is filtered. A schematic view of such a helical resonator is given in Fig. 2.22. The sine wave from the arbitrary waveform generator is coupled to the resonator using an antenna consisting of a small coil of copper wire. The parameters for the resonator were chosen according to the design guidelines in [87]. For trap A, a copper shielding conductor with an inner diameter of $D_{shield} = 90\,\mathrm{mm}$, was used around an inductor of $n = 40$ loops with a spacing of $d = 2.5\,\mathrm{mm}$, wound around a perspex support with a diameter of $D_{ind} = 50\,\mathrm{mm}$. The inductance of this inductor is

$L = 32\,\mu$H. An adjustable air capacitor is mounted in parallel with this inductor, making the (loaded) resonance frequency adjustable between $f_{res} = 1.8$ MHz and $f_{res} = 3.8$ MHz. Trap A itself has a capacitance of $C = 13$ pF.

The resonator used for trap B had a slightly different design. A double wound helix was used in order to be able to compensate for stray electric fields. Instead of the single wire shown in Fig. 2.22 now two wires follow the same coiled path, by which different DC electric fields can be applied to the RF electrodes. For the support of these helices a teflon cylinder is used, for which the dielectric losses are much lower compared to perspex. The bottom end of the coils is now connected to ground via a capacitor of $C = 100$ nF, to provide a connection to ground for the RF, while a DC voltage can be connected to provide the desired trapping potential.

For this resonator, again a copper shielding conductor with an inner diameter of $D_{shield} = 90$ mm, was used. This coil consists of $n \sim 60$ loops with a spacing of $d = 1.3$ mm, wound around a teflon support with a diameter of $D_{ind} = 38$ mm.

2.3.4 Loading the trap with calcium ions

Calcium is a highly abundant element, and can be cheaply purchased. The ^{40}Ca is with 97% the most abundant isotope (see Table 2.1), and is obtained efficiently from a piece with a natural composition. In order to bring calcium into the gas phase, material is evaporated from an oven made of aluminum oxide, which is heated by a tungsten wire carrying a current of I = 2A. The neutral atom cloud is ionized using resonant photo-ionization, which leads to selective ionization of one isotope. Isotope selective photo-ionization of calcium was first performed in 1974 [88], using a two-step process from a metastable state with light at 616 and 488 nm. The first optical loading of an ion trap was performed by Kjaergaard *et al.* in 2000 [89], using two photons at 272 nm. We use a method involving resonant excitation of the $4s\,^1\mathrm{S}_0 - 4p\,^1\mathrm{P}_1$ transition at 423 nm, followed by excitation by laser light at wavelengths shorter then 391 nm to the continuum, or around 391 nm to autoionizing states (Fig. 2.23), similar to the scheme proposed in [90]. A transition at 423 nm is resonantly excited using a frequency-doubled continuous wave Ti:Sa ring laser (Coherent 899), pumped by a 5W Nd:YAG laser (Spectra Physics Millenia). This laser is frequency-locked to a temperature stabilized etalon. The output light of the ring laser is frequency doubled in a 'bowtie' cavity based on an Lithium Triborate (LBO) crystal, which is stabilized to the output frequency of the ring laser using a Hänsch-Couillaud lock [91]. The calcium atom is photo-ionized from the excited state. For the experiments

described in Chapter 5, a pulsed, frequency tripled Nd:YAG laser was used (Solar), producing $P = 0.3\,\mathrm{J}$ pulses of 355 nm light at 10 Hz repetition frequency. In the later experiments (Chapter 6 and 7), frequency doubled light from the frequency comb at $\lambda < 391$ nm was used.

2.3.5 Laser cooling of calcium ions

Calcium ions have only one valence electron, leading to a relatively simple energy level structure (Fig. 2.24). The ion is laser-cooled on the $4s\,^2\mathrm{S}_{1/2} - 4p\,^2\mathrm{P}_{1/2}$ transition at 397 nm, with a natural linewidth of 22 MHz. The situation is slightly different from the ideal two-level system as described in Chapter 2.2, since there is a third level involved. In 7 % of the excitations, the electron decays into the $3d\,^2\mathrm{D}_{3/2}$-state. Since this state has a lifetime of 1 second, a repumper at 866 nm is necessary to keep the ions in the cooling cycle. Two grating-stabilized diode lasers are used in order to perform the cooling and repumping. The cooling laser has a small fluorescence pedestal, which is centered at around 396.2 nm, and extends to 394 nm. This pedestal could potentially lead to optical pumping into the $3d\,^2\mathrm{D}_{5/2}$-state. However, since the divergence of this emitted fluorescence beam is different from the laser beam emitted at 397 nm, most of this light is filtered out by the optical setup along the cooling laser path. For the measurements on direct frequency comb excitation of the dipole forbidden $4s\,^2\mathrm{S}_{1/2} - 3d\,^2\mathrm{D}_{5/2}$ transition, an additional grating was placed in the beam in order to further reduce this background light. Both diode lasers are placed in an aluminum box in order to shield the laser setup from acoustic influences and temperature drifts in the laboratory. The frequency of the cooling laser is steered by computer, based on continuous measurements with an Atos LM-007 lambdameter, while the repumper laser is left free running.

Isotope	Abundance
^{40}Ca	96.94(16)%
^{42}Ca	0.65(2)%
^{43}Ca	0.135(10)%
^{44}Ca	2.09(11)%
^{46}Ca	0.004(3)%
^{48}Ca	0.19(2)%

Table 2.1: The (stable or very long-lived) isotopes of calcium and their abundance [92].

2.3.6 Detection of fluorescence

All spectroscopic experiments described in this thesis rely on the imaging of light at 397 nm onto a detector. In the first two experiments (described in Chapter 5 and 6) a photomultiplier tube was used for photon detection. The corresponding imaging system is shown in Fig. 2.25. The beam of fluorescence photons is collimated by a lens with a focal length of $f = 25\,\mathrm{mm}$ inside the vacuum chamber, and imaged onto the photomultiplier tube using a second lens with a focal length of $f = 100\,\mathrm{mm}$, leading to a magnification of $M = 4$. In order to suppress the detection of ambient photons, the total imaging setup is built inside a light-shielded box, and the necessary optics can be aligned from outside this box. In addition, the vacuum chamber windows are mounted under Brewster's angle to minimize reflections of the light used for laser cooling.

With trap B the imaging optics were changed, so that both a photomultiplier tube and an Electron-Multiplying Charge-Coupled Device camera (EMCCD, Andor iXon$^{\mathrm{EM}}$ +) could be used simultaneously (Fig. 2.26). Inside the vacuum, an aspheric lens (AR coated for the UV) with an effective focal length of $EFL = 25\,\mathrm{mm}$ was used. With this lens an intermediate focus at $\approx 28\,\mathrm{cm}$ from the trapping center is created, where the image is spatially filtered using a pinhole. The image at the pinhole is re-imaged onto the EMCCD using a $f = 10\,\mathrm{cm}$ lens over a distance of two times $2f$, resulting in a total magnification of the imaging system of $M = 9\,(1)$. A similar system is used to image the ion cloud onto the photomultiplier. As in the first optical setup, the bending mirrors and second lens can be aligned from outside the light-shielding box.

Despite the filtering of the cooling laser beam and the use of either Brewster-angled or antireflection coated entrance windows for the vacuum chamber, there is a background of scattered photons, which is detected by the camera or photomultiplier. It is especially important to correct for this background on alignment of the cooling laser (where the detected number of photons at 397 nm can increase on wrong alignment due to an increase of scattering) and in the case of detection of the weaker signal due to the $4s\,^2\mathrm{S}_{1/2} - 4p\,^2\mathrm{P}_{3/2}$-transition in the presence of the cooling laser. Optical pumping to the long-lived D-levels is used to correct for this background, the (see Fig. 2.24). For the alignment of the cooling laser, the repumper laser on the $3d\,^2\mathrm{D}_{3/2} - 4p\,^2\mathrm{P}_{1/2}$ transition is asynchronously chopped with a duty cycle of 3 % (in order to minimize distortion of the cooling). Both the signal with and without the repumper at 866 nm are recorded. These two signals are subtracted with correction for the duty cycle, to give only the fluorescence signals from the ions. The electronic scheme for this detection method is given in Fig. 2.27.

For the detection of the $4s\,^2\mathrm{S}_{1/2}-4p\,^2\mathrm{P}_{3/2}$-transition at 394 nm a very similar method is used. In this situation, the second repumper on the $3d\,^2\mathrm{D}_{5/2}-4p\,^2\mathrm{P}_{3/2}$ at 854 nm was chopped using a mechanical chopper with a duty cycle of 50%. The signals with and without the presence of the repumper are subtracted in order to filter out the signal due to excitation of the $4s\,^2\mathrm{S}_{1/2}-4p\,^2\mathrm{P}_{3/2}$-transition (the experiment is described in detail in Chapter 6).

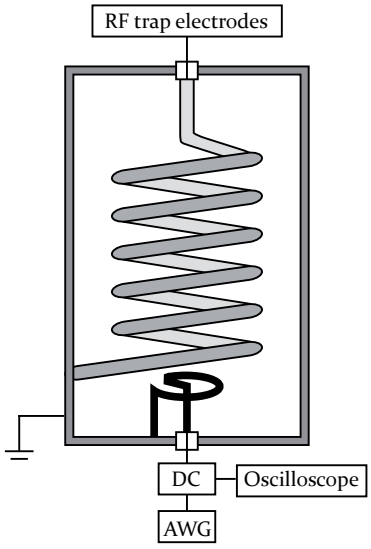

Figure 2.22: Schematic view of a helical resonator as used for the ion trap: It consists of an inner conducting coil shielded by a grounded outer conducting cylinder. The electric field generated by an arbitrary waveform generator is coupled in through an antenna, indicated by the black loop in the bottom. In reality the coil has $n \approx 10$ windings to improve the coupling. The other side of the inductor is connected to the RF trap electrodes. The field can be monitored through the reflected signal, which is split off via a directional coupler (DC). BNC connectors are used for the feedthroughs in the top and bottom.

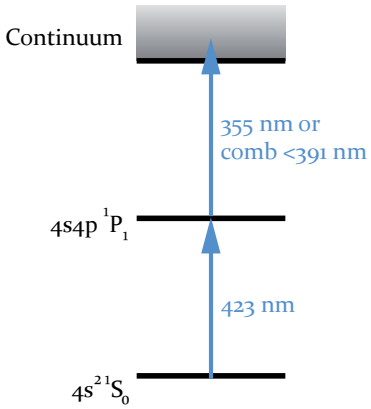

Figure 2.23: Simplified energy level diagram for neutral calcium, showing the levels involved in the photo-ionization: A resonant photon at 423 nm brings the atom in an excited state, from which the calcium can be ionized with a 355 nm photon from a frequency-tripled Nd:YAG laser or with wavelengths below 391 nm from the frequency-doubled frequency comb.

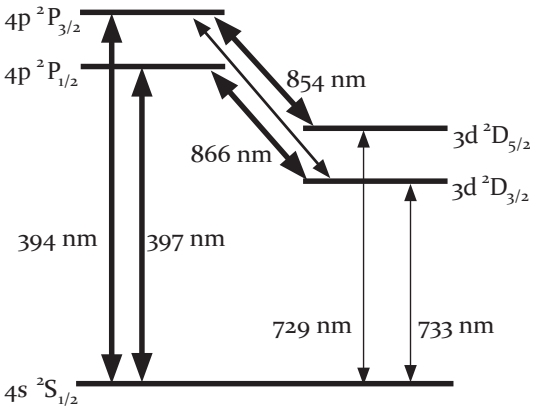

Figure 2.24: Partial energy level diagram for the $^{40}Ca^+$-ion. The shown levels are the energy levels involved in the experiments described in this thesis. For more detailed information on the involved levels see Table 1.1.

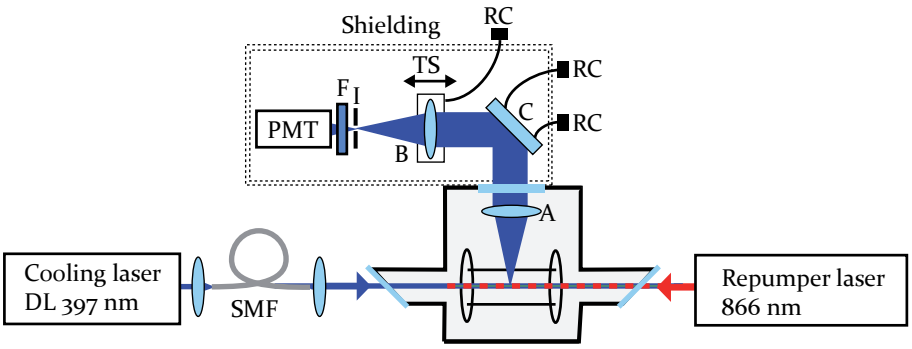

Figure 2.25: Schematic view of the optics used for imaging the fluorescence of the ion: Light emitted by the trapped ions is collimated on a lens (A) inside the vacuum chamber ($d = 25\,\text{mm}$, $f = 25\,\text{mm}$). A second lens (B) ($d = 50\,\text{mm}$, $f = 100\,\text{mm}$) is used to focus the light onto a iris (I) for spatial filtering, followed by a narrow band interference filter (F) at $\lambda = 397\,\text{nm}$. The filtered light is detected on a Photomultiplier tube (PMT). The beam can be aligned onto the PMT using a mirror (C). The lens B is mounted on a translation stage (TS) in order to be able to optimize the focus for spatial filtering. The imaging setup is mounted in a felt-covered box to reduce background photon scattering onto the PMT. The adjustable optics C and B can be steered from outside the light-shielding box (via a remote control RC).

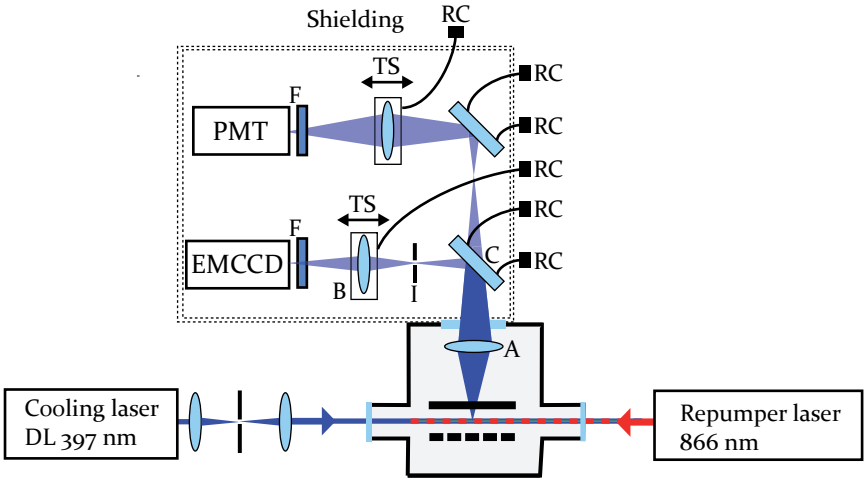

Figure 2.26: Schematic view of the optics used for imaging the fluorescence of the ion: In the second trapping setup, both the PMT and EMCCD can be used simultaneously, with very similar imaging systems. The labeling is the same as in Fig. 2.25.

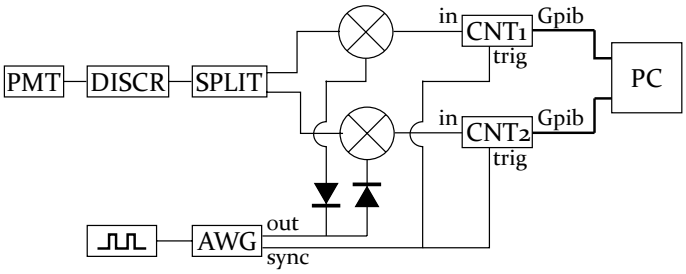

Figure 2.27: Electronic diagram for the fluorescence detection scheme, used for both alignment of the cooling laser and (in a slightly modified form) for detection of the signal due to the $4s\,^2\mathrm{S}_{1/2} - 4p\,^2\mathrm{P}_{3/2}$-transition. The photon signal detected on the photomultiplier tube (PMT) is converted to square pulses by a discriminator (DISCR). This signal is divided into two branches using a power splitter (SPLIT). The splitter outputs are mixed with a signal which is non-zero when the repumper laser is present in the trap on one mixer, and when the repumper is absent on the other. These signals are produced by an arbitrary waveform generator (AWG), which is triggered by an optical chopper. The mixed signals are counted on two different counters (CNT1 and CNT2), so both the signals with and without the repumper are recorded. The difference in counts is calculated by a computer (PC), resulting in the background-corrected fluorescence signal.

Chapter 3

The frequency comb laser

3.1 The principle of a frequency comb laser

The name of the frequency comb is based on its representation in the spectral domain, which consists of a regular array of modes (Fig. 3.1(a)). Such a spectrum is created from a mode-locked laser, in which many cavity modes can co-exist and be amplified. The phase relation between the cavity modes is fixed. This results in a spectrum of 'comb teeth' which are equally spaced in frequency. In the time domain, the interference between the cavity modes results in a train of short pulses (Fig. 3.1(b)). The pulses are separated by a time T, which is determined by the length of the cavity. In general, there will be a phase difference ϕ_{ceo} between the carrier wave and the envelope of the pulse, which will change by $\Delta\phi_{ceo}$ from pulse to pulse (Fig. 3.1(b)).

The time- and frequency-domain pictures of the frequency comb are connected through a Fourier transformation. The comb modes are spaced by a distance $f_{rep} = 1/T$ in the frequency domain, and span over a width determined by the gain bandwidth of the laser crystal, the dispersion characteristics of the cavity and self-phase modulation. On extrapolating the comb of frequencies to zero, there is an offset of $f_{ceo} = f_{rep}\Delta\phi/2\pi$. The mode-locked laser is turned into a frequency comb by locking both the f_{ceo} and f_{rep} to a frequency standard, as is described in Chapter 3.3.2. In this frequency comb, the frequency of the n^{th} comb mode is fixed to $f_n = f_{ceo} + n \times f_{rep}$. Since both f_{ceo} and f_{rep} are frequencies on the order of MHz to GHz, they can be measured using commercially available electronics, and locked to a frequency standard such as a rubidium or caesium clock. In this way, the accuracy of such a time standard can be transferred to the optical domain, making very high accuracy spectroscopy possible at optical frequencies and beyond. In addition, the frequency comb also provides the

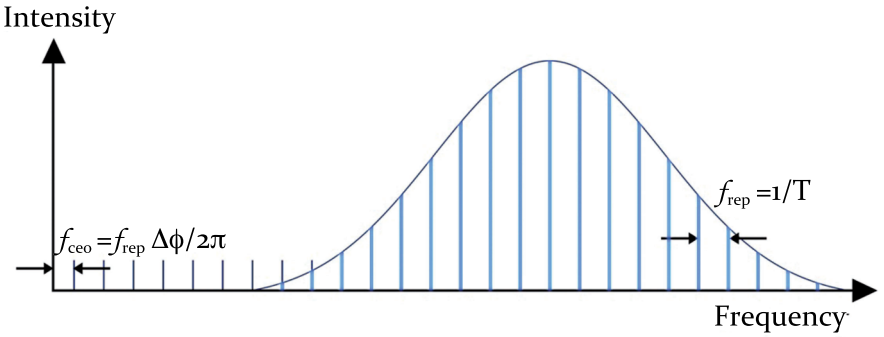

(a) In the frequency domain the comb is composed of a regular array of laser modes.

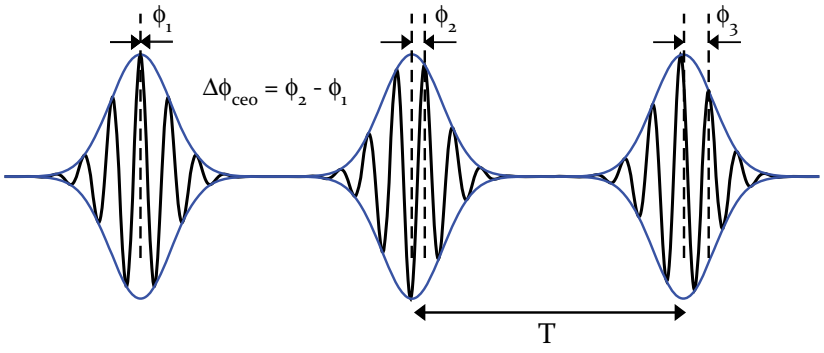

(b) In the time domain the frequency comb consists of an infinite train of short pulses.

Figure 3.1: Schematic representation of the frequency comb in both the time and frequency domain.

clockwork to transfer the accuracy between measurements in the optical domain, or from PHz back to MHz frequencies.

3.2 Principle of operation

3.2.1 The AC Kerr effect and the mode-locked laser

In order to achieve mode-locking, a mechanism of loss modulation is necessary to make the pulsed operation more favourable than continuous wave (cw) lasing. Both active and passive mode-locking have been demonstrated. The passive mechanism of Kerr-lens mode-locking has been very successful for generating ultra-short pulses. Combined with higher order dispersion control and the ultra-broadband gain profile of Ti:sapphire, the AC Kerr effect enables the production of few-cycle pulses from Ti:Sa oscillators.

The Kerr effect is a change of the refractive index, in the presence of an electric field. It is a nonlinear effect, which in the case of the AC Kerr effect is induced by the light field itself. The light induces a change in refractive index given by $n = n_0 + n_2 \times I$ [93], where n_0 is the linear, n_2 is the non-linear refractive index and I is the intensity. The central (more intense) part of the laser beam thus experiences a higher effective refractive index than the outer part. This effect leads to self-focusing, which is responsible for Kerr-lens mode locking. Combined with a hard aperture at an appropriate position in the cavity, intensity dependent losses are introduced (Fig. 3.2). This aperture has the effect equivalent to a fast saturable absorber. For cw lasing, a part of the beam is cut on the aperture and there is a constant net loss mechanism in the cavity. However, for a high intensity spike this loss can be reduced for a short time by the self-focusing effect. Short pulses thus have a higher net gain in this situation, and can be stably formed. These lasers can be self-starting from noise fluctuations if the right conditions are fulfilled [94, 95]. However, mode-locking typically must be induced actively, as is done in our case by quickly moving a mirror on a movable stage.

Kerr-lens mode locking is even possible without an additional hard aperture. The reason for this is that the gain profile in the crystal varies radially, due to the beam profile of the pump beam. By tightly focusing the pump laser this spatially dependent gain can have a better overlap with the self-focused short pulses, as compared to cw operation, and can therefore also lead to stable pulsed operation [96] (Fig. 3.3).

The AC Kerr effect has a second major influence on the mechanism forming a femtosecond frequency comb laser through self-phase modulation. Since the intensity is time-dependent, the center of the pulse experiences a higher refractive index. Inn this way the peak of the pulse in the time domain is delayed. The resulting phase modulation shifts the leading part of the pulse to longer wavelengths, while the trailing part is shifted to shorter wavelengths (Fig. 3.4). Through this ef-

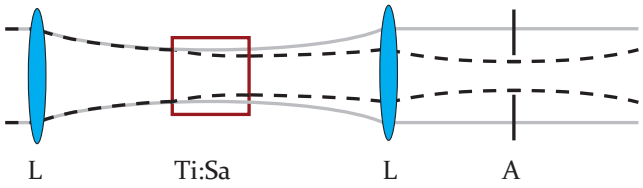

Figure 3.2: Schematic view of the effect of self-focusing with a hard aperture (A) in an optical system with curved optics (L): For pulsed operation (black dashed trace) the high peak power leads to self-focusing through the Kerr effect. In continuous wave operation (grey trace), the power is lower and there will be less self-focusing. When a hard aperture is placed at an appropriate position in the beam path, for the continous wave the losses will be higher than in pulsed operation.

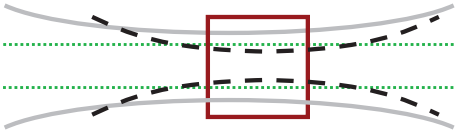

Figure 3.3: Schematic view of the effect of self-focusing in a crystal (depicted here as a square) without an additional hard aperture: In CW operation, the peak power is low and there is little self-focusing (continuous line). In pulsed mode, the peak power is much higher and the laser is focused more due to the Kerr effect (dashed). When the pump volume is relatively small, the overlap between the pump and the cavity mode is better for the mode with the additional focusing effect, and thus the pulses experience a higher gain.

fect additional bandwidth is created on the original spectrum of the pulse, leading to broadening of the output spectrum of the frequency comb.

3.2.2 Group velocity dispersion and chirped mirrors

The generation of broad spectra in a frequency comb crucially depends on keeping the pulses short (and thus the peak powers high) for effective use of the non-linear effects described in the previous section. However, while travelling through the cavity the pulse spreads in time due to group velocity dispersion (GVD) (Fig. 3.5), which is given by $GVD = \frac{\partial^2 k}{\partial \omega^2}$. Most materials, such as the Ti:Sa-crystal, fused silica wedges and air in the frequency comb cavity have a positive GVD (normal dispersion) at 800 nm. Without the addition of negative dispersion this effect would limit the pulse duration to longer pulse lengths. Negative GVD (anomalous dispersion) can for example be provided by prism pairs [97], gratings [98] or chirped mirrors [99] (for which the dispersion is denoted as group delay dispersion

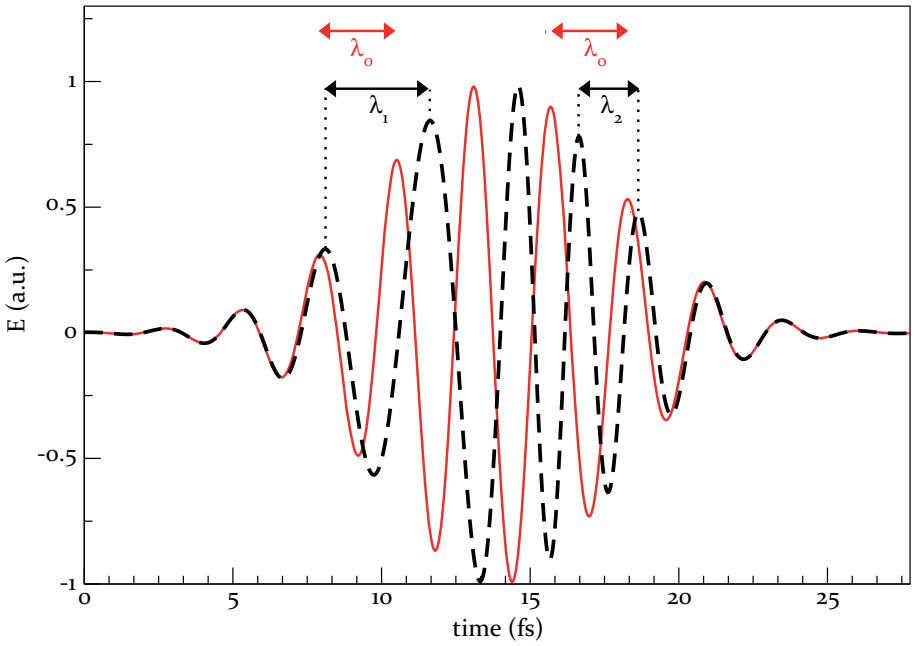

Figure 3.4: Self-phase modulation on the real part of the electric field, as caused by the Kerr effect for a Gaussian pulse: The center of a pulse entering the non-linear medium (dashed line) is delayed due to the higher refractive index, causing the front of the pulse to be red-shifted (λ_1) while the trailing edge of the pulse is blue-shifted (λ_2). For reference, the wavelength of the non-modulated pulse (λ_0) is indicated as well.

or GDD). Prism pairs have been widely used in the first Ti:Sa-based femtosecond lasers, making pulses as short as $\sim$ 8.5 fs. [100]. However, the use of chirped mirrors allows for beter control of higher order dispersion, a much more compact design and easier alignment of the laser.

Chirped mirrors are a type of Bragg mirrors: They consist of alternating layers of high and low refractive index to produce reflection [101]. A stack of such layers forms a Fabry-Perot-like structure, where positive interference between the layers leads to a high reflectivity. This structure will have a wavelength dependent penetration depth, and as such a group delay [102]. A quarter wave stack (with layers of an optical thickness of $\lambda/4$) is most efficient in reflecting a certain wavelength λ. A monotonic variation of the period results in a monotonic variation of the group delay and a zero GDD. For a quadratic penetration depth as a function of wavelength, either positive or negative GDD can be realized. The optical thickness of the layers can be numerically optimized to produce highly reflective

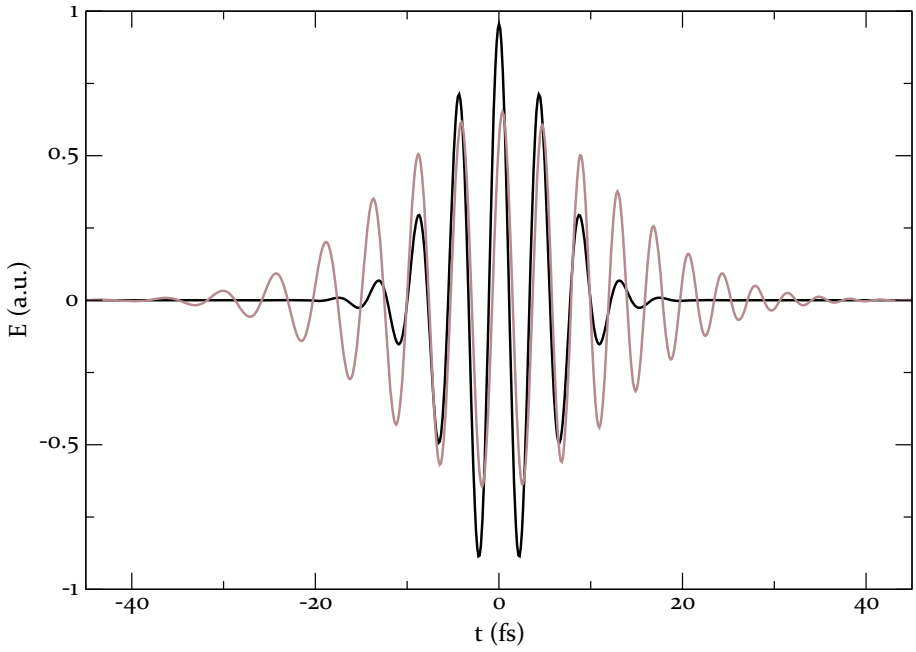

Figure 3.5: The effect of dispersion on the real part of the electric field: A 10 fs pulse at 800 nm (black trace) becomes twice as long on traveling through 1.7 mm of fused silica (grey trace).

mirrors with the desired GDD-properties. By compensating the positive chirp due to the optical elements in the cavity using negative GVD mirrors, the pulse length inside the crystal can be minimized, in order to create short pulses.

3.2.3 The non-linear Schrödinger equation

The effects producing a mode-locked laser are quantified using the non-linear Schrödinger equation. To derive this equation, we begin by describing the propagation of electro-magnetic waves with the so-called wave equation, which is obtained from the Maxwell equations [103]:

$$\vec{\nabla}^2\vec{E} - \mu_0\epsilon_0\frac{\partial^2\vec{E}}{\partial t^2} = \mu_0\frac{\partial^2\vec{P}}{\partial t^2} \tag{3.1}$$

The response of a medium to the field is described by its polarization $\vec{P}$, which is nonlinear for intense light fields. The induced polarization can be written as a sum of linear and nonlinear terms $\vec{P} = \vec{P}_L + \vec{P}_{NL}$, where the linear term is given

by [103]:

$$\vec{P}_L = \epsilon_0 \int_{-\infty}^{\infty} \chi^{(1)}(t-t')\vec{E}(\vec{r},t')dt' \tag{3.2}$$

In this equation $\chi^{(1)}$ is the electric susceptibility of the medium. Since the linear polarization is a convolution of $\chi^{(1)}$ and $\vec{E}$, its Fourier transform is given by the product of the Fourier transforms of $\chi^{(1)}$ and $\vec{E}$ (where the vector sign is omitted to improve readability):

$$\widetilde{P}_L = \epsilon_0 \widetilde{\chi}^{(1)} \widetilde{E} \tag{3.3}$$

The Fourier transform of the second order time-derivative gives a factor $-\omega^2$ [104], and thus the total wave equation (3.1) can be transformed into:

$$\nabla^2 \widetilde{E} + \epsilon_0 \mu_0 \omega^2 \widetilde{E} = -\omega^2 \mu_0 \epsilon_0 \widetilde{\chi}^{(1)} \widetilde{E} \tag{3.4}$$

Now taking the propagation to be only in the z-direction ($\vec{E} = E_z \hat{z}$) and explicitly expressing the carrier wave with wavenumber k_0 and frequency ω_0, the electric field can be written as:

$$\widetilde{E}_z = \widetilde{A}(z,\omega) e^{-i(k_0 z - \omega_0 t)} \tag{3.5}$$

Putting this expression into the wave equation, and dividing by $e^{-i(k_0 z - \omega_0 t)}$ leads to:

$$\frac{\partial^2 \widetilde{A}}{\partial z^2} - \widetilde{A} k_0^2 - 2ik_0 \frac{\partial \widetilde{A}}{\partial z} + \frac{\omega^2}{c^2}(1+\chi^{(1)})\widetilde{A} = 0 \tag{3.6}$$

The above expression can be simplified by using the slowly varying envelope approximation. This approximation is based on the assumption that the pulse envelope $A(x,y,z)$ varies slowly compared to the wavelength of light, or $\frac{\partial^2 A}{\partial z^2} \ll ik\frac{\partial A}{\partial z}$, so $\frac{\partial^2 A}{\partial z^2}$ can be neglected. In addition, the electric susceptibility can be written as $1+\chi^{(1)} = (n + i\frac{c}{2\omega}\alpha)^2 \approx n^2$ [103], where the absorption α is assumed to be small and n is the refractive index. The wave equation then becomes:

$$-\widetilde{A} k_0^2 - 2ik_0 \frac{\partial \widetilde{A}}{\partial z} + \frac{\omega^2}{c^2} n^2 \widetilde{A} = 0 \tag{3.7}$$

or (with $k = \omega n/c$ and using $k^2 - k_0^2 = (k+k_0)(k-k_0) \approx 2k_0(k-k_0)$):

$$2k_0(k-k_0)\widetilde{A} - 2ik_0 \frac{\partial \widetilde{A}}{\partial z} = 0 \tag{3.8}$$

In order to explicitly express the group velocity dispersion the wavenumber k can be expanded into a series around ω_0, taking into account up to the second order derivative:

$$k(\omega) \approx k_0 + \left[\frac{\partial k}{\partial \omega}\right]_{\omega_0} (\omega - \omega_0) + \frac{1}{2}\left[\frac{\partial^2 k}{\partial \omega^2}\right]_{\omega_0} (\omega - \omega_0)^2 \tag{3.9}$$

The Fourier transform of (3.8), with (3.9) inserted for k, divided by $2ik_0$ gives an expression for the pulse envelope in the time domain:

$$\frac{\partial A}{\partial z} + \left[\frac{\partial k}{\partial \omega}\right]_{\omega_0} \frac{\partial A}{\partial t} - \frac{i}{2}\left[\frac{\partial^2 k}{\partial \omega^2}\right]_{\omega_0} \frac{\partial^2 A}{\partial t^2} = 0 \tag{3.10}$$

For the description of mode-locking, the third order susceptibility must be taken into account ($\chi^{(2)} = 0$ in an isotropic medium). This nonlinear term is given by [103]:

$$\vec{P}_{NL} = \epsilon_0 \int_{-\infty}^{\infty} \chi^{(3)}(t-t_1, t-t_2, t-t_3)\vec{E}(t-t_1)\vec{E}(t-t_2)\vec{E}(t-t_3)dt_1 dt_2 dt_3 \tag{3.11}$$

By assuming an instantaneous response of the medium to the electric field or $\chi^{(3)}(t-t_1, t-t_2, t-t_3) = \chi^{(3)}\delta(t-t_1)\delta(t-t_2)\delta(t-t_3)$, we obtain for equation (3.1):

$$\vec{\nabla}^2\vec{E} - \mu_0\epsilon_0(1+\chi^{(1)})\frac{\partial^2 \vec{E}}{\partial t^2} = \mu_0\epsilon_0 \frac{\partial^2 \chi^{(3)}\vec{E}\vec{E}\vec{E}}{\partial t^2} \tag{3.12}$$

If a wave with polarization in the x-direction is taken, the tensor-product on the right-hand side is [103]:

$$\vec{\nabla}^2\vec{E} - \mu_0\epsilon_0(1+\chi^{(1)})\frac{\partial^2 \vec{E}}{\partial t^2} = \mu_0\epsilon_0 \frac{\partial^2 \frac{3}{4}\chi^{(3)}_{xxxx}|E|^2\vec{E}}{\partial t^2} \tag{3.13}$$

On the left-hand side are the terms for the equation with only P_L, which can be written in the form of equation (3.10). The term on the right side can be rewritten using the same substitution, arriving at the so-called nonlinear Schrödinger equation:

$$\frac{\partial A}{\partial z} + \left[\frac{\partial k}{\partial \omega}\right]_{\omega_0} \frac{\partial A}{\partial t} - \frac{i}{2}\left[\frac{\partial^2 k}{\partial \omega^2}\right]_{\omega_0} \frac{\partial^2 A}{\partial t^2} = \chi^{(3)}_{xxxx}\frac{-3\omega_0^2}{8ik_0}|A|^2 A \tag{3.14}$$

$$= \frac{3i\chi^{(3)}_{xxxx}\omega_0}{8nc}|A|^2 A \tag{3.15}$$

The $\frac{\partial k}{\partial \omega}$-term represents the influence of the inverse group velocity or group delay, the part proportional to $\frac{\partial^2 k}{\partial \omega^2}$ is due to the group velocity dispersion (GVD). The

term on the right-hand side is responsible for the AC-Kerr effect, which can be split into a real (self-focusing) and imaginary (self-phase modulation) part. In order to calculate the pulse dynamics (including the wavelength dependent dispersion and gain), equation (3.14) can be solved through numerical simulations. The pulse peak power and duration depend on the position inside the cavity, and the shape of the output spectrum is dependent on the exact amount of GVD [105].

3.3 Ti:Sapphire frequency combs based on commercial negative GVD mirrors

3.3.1 Laser design

Two similar Ti:Sa-based frequency combs were built, based on commercial chirped mirrors (Layertec GmbH). Due to the broad gain bandwidth of Ti:Sa, in principle pulses as short as 5 fs are possible [106]. In order to make a laser that can sustain a broadband pulse, the overall group delay dispersion (GDD) of the cavity needs to be close to 0 fs^2 over a wide spectrum. A low net GDD will ensure that the pulse remains short, with a high peak intensity, upon propagation. This provides the necessary condition for a high self-phase modulation, which in turn generates additional spectral bandwidth and strong mode locking. Negative dispersion is added to the cavity by using chirped mirrors. In the following description of the frequency combs I and II, average values for this GDD are given. However, over the output spectrum these values can fluctuate over tens of fs^2, and produce oscillations in the output spectrum. Sometimes dispersion oscillation compensated pairs are used. Such a pair consists of two mirrors, both with a dispersion oscillating with frequency, for which the oscillation mostly cancels out for the combination of the two (Fig. 3.6).

3.3.1.1 Frequency comb I

The first frequency comb we built generates a broadband spectrum, to serve as a seed laser for a non-collinear optical parametric chirped-pulse amplifier [107]. The design of this laser is shown in Fig. 3.7. The total cavity length per roundtrip is 4 m, which corresponds to a repetition frequency of $f_{rep} = 75$ MHz. By adjusting the cavity length, the repetition rate can be tuned between 70 and 300 MHz. The gain medium for this laser is a Ti:Sa crystal with an optical path length of 2.5 mm, pumped with 5.5 W from a frequency doubled Nd:YVO_4-laser (Coherent Verdi). The pump light is focused onto the crystal using an $f = 36$ mm lens. The mirrors M1 and M2 are a dispersion oscillation compensated pair, with a GDD of -70 fs^2

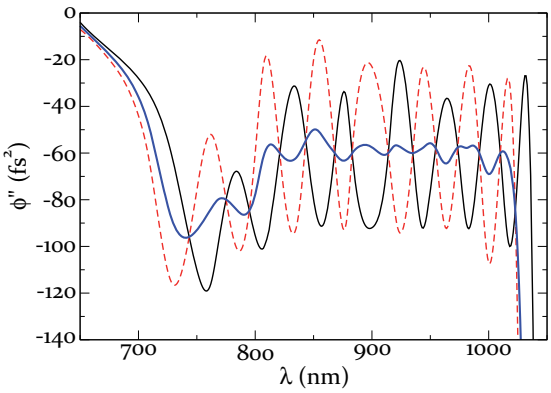

Figure 3.6: Dispersion curve for an oscillation compensated pair with a GDD of $-70\,\mathrm{fs}^2$ per mirror. The individual mirrors, as indicated by the thin solid and dashed lines, have a dispersion oscillating with frequency. The average of these two curves (thick gray line) shows that this oscillation largely cancels for the combination of the two mirrors.

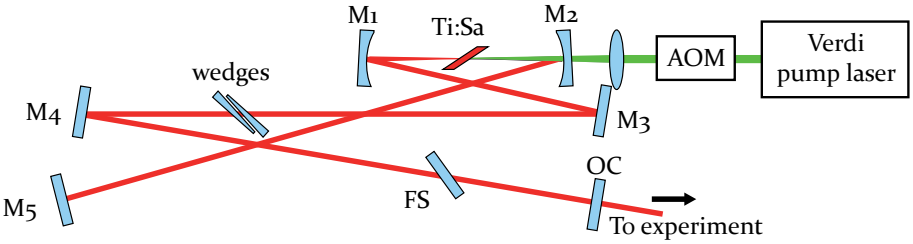

Figure 3.7: Design of frequency comb I. The lasers is built using commercial mirrors (M1-M5 and OC=80% output coupler, see text) from Layertec. The mirror M3 is mounted on a piezo. FS=1 mm fused silica.

each. They are anti-reflection coated for the pump laser light at 532 nm, and have a radius of curvature of 50 mm. M3, M4 and M5 all have a GDD of $-50\,\mathrm{fs}^2$, while the 80% output coupler has a GDD of $0\,\mathrm{fs}^2$. This combination of mirrors brings the total negative dispersion for the cavity to $-530\,\mathrm{fs}^2$. The Ti:Sa crystal has a positive group velocity dispersion (GVD) of $58\,\mathrm{fs}^2/\mathrm{mm}$ at 800 nm. For control of the f_{ceo}, wedges of fused silica are inserted in the cavity, which have a GVD of $36\,\mathrm{fs}^2/\mathrm{mm}$. Since with these elements the total dispersion has quite a high negative value, a plate of 1 mm fused silica is added, bringing the total amount of positive dispersion to $\sim 500\,\mathrm{fs}^2$.

With this design, pulses with a spectral width of more than 300 nm were produced (Fig. 3.8), with an average power of $P = 0.4\,\mathrm{W}$. This output was used as a

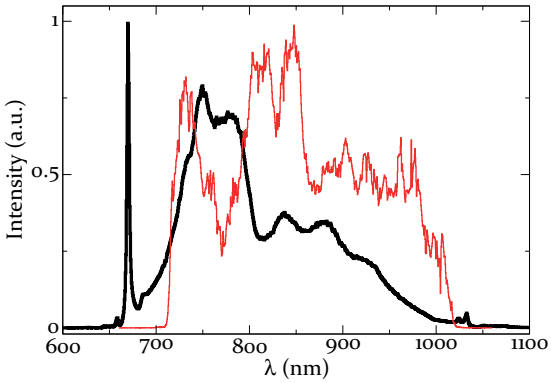

Figure 3.8: Output spectrum for the first frequency comb laser (thick trace), which was used as a seed for noncollinear optical parametric chirped pulse amplification [107, 108]. The amplified output spectrum is indicated by the thin trace.

seed for non-collinear optical parametric chirped-pulse amplification, producing pulses with a peak intensity of 2 TW and a duration of 7.6 fs [108].

3.3.1.2 Frequency comb II

The laser setup for the experiments on calcium ions is depicted in Fig. 3.9. The total cavity length is approximately 1.7 m, corresponding to a repetition frequency of $f_{rep} = 180$ MHz. The repetition frequency can be adjusted in the range $f_{rep} = 150 - 220$ MHz. The 2.5 mm long Ti:Sa crystal is pumped with $P = 3.8$ W from a pump laser at 532 nm, focused using a $f = 36$ mm lens. M1 and M2 have a radius of curvature of $r = 50$ mm, and have an anti-reflection coating for the pump laser wavelength. They form an oscillation compensated pair with a negative GVD of -70 fs^2 each. The 85% output coupler has approximately 0 fs^2, as has M3. The other two mirrors M4 and M5 both have a dispersion of -50 fs^2. These mirrors are again designed to cancel the oscillation on the combination of the two. However, since one of these mirrors is the end mirror, the effect of this cancellation is less. The total negative dispersion on one roundtrip through the cavity thus comes to -430 fs^2. The total (positive) dispersion per roundtrip due to Ti:Sa is 290 fs^{2*}. For control of the value of f_{ceo}, two fused silica wedges are inserted in the cavity. Per roundtrip, a few mm of fused silica are passed, bringing the total dispersion to approximately -30 fs^2. The resulting spectrum is

*The dispersion is wavelength dependent, the mentioned value is an average value around the central wavelength.

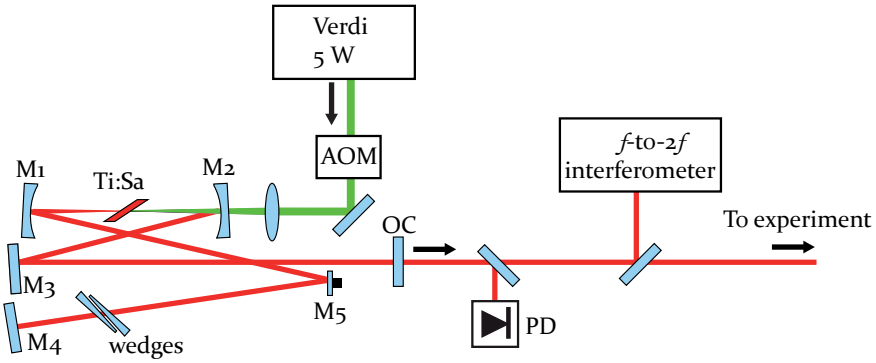

Figure 3.9: Design of frequency comb II. The lasers is built using commercial mirrors (M1-M5 and OC=85% output coupler) from Layertec. The mirror M5 is mounted on a piezo. PD=photodiode.

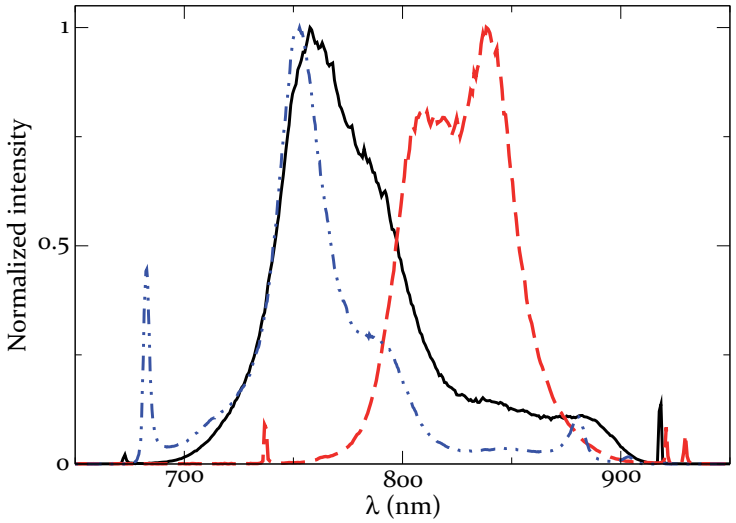

Figure 3.10: Comb spectra with different amounts of glass inside the cavity. Solid line: ~ 1.5 mm fused silica, dashed line: no wedges, dash-dotted line: ~ 2 mm fused silica.

very much dependent on the exact dispersion balance in the frequency comb (Fig. 3.10). The average output power of this design is $P = 0.7$ W. By changing the optical path length through two wedges of fused silica (FS), the dispersion curve is shifted and slightly tilted. This shift corresponds to a change in the frequency comb spectrum (Fig. 3.10).

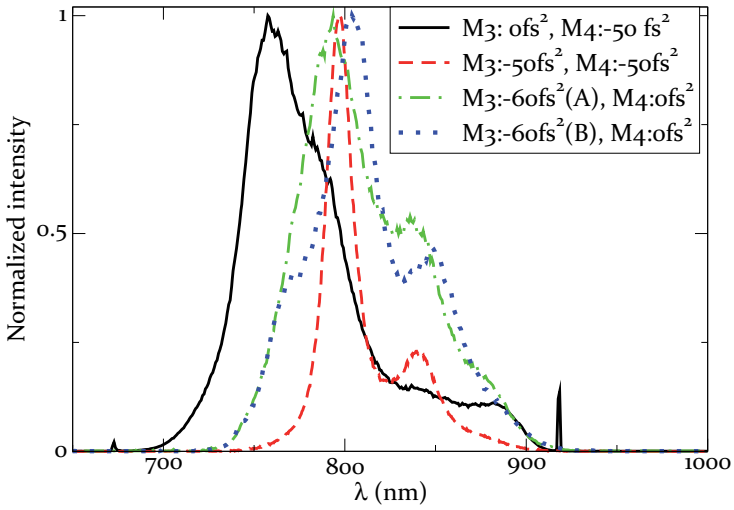

Figure 3.11: Comb spectra with different mirrors for GVD-correction. Besides having different average values for the dispersion, the used mirrors will also have a different wavelength dependence. The mirrors indicated A and B are the two mirrors from a dispersion oscillation compensated pair.

The spectrum can also be modified by using mirrors with different GVD-curves (Fig. 3.11). The spectrum will narrow on adding more negative dispersion, but also the peak can be shifted by modifying the zero-crossing of the total dispersion curve.

3.3.2 Locking the carrier-envelope offset and repetition frequency

The modelocked laser is turned into a frequency comb by very accurate control of the repetition frequency f_{rep} and the carrier-envelope offset frequency f_{ceo} (the electronic setup is shown in Fig. 3.12). The repetition frequency is easily detected using a fast photodiode (EOT ET-4000). It is filtered out electronically from the photodiode signal, and then mixed with the locking frequency from a low-noise, stable frequency generator. The difference frequency is sent to a PID controller, which provides the feedback signal for locking f_{rep}. This feedback is applied on the laser through a fast and a slow channel. Short term stabilization is achieved using a piezo-electric transducer (on which one of the cavity mirrors is mounted, see Fig. 3.9) to change the cavity length. On long time scales, the cavity length is corrected through the baseplate temperature. Heating resistors heat up the baseplate to provide this feedback.

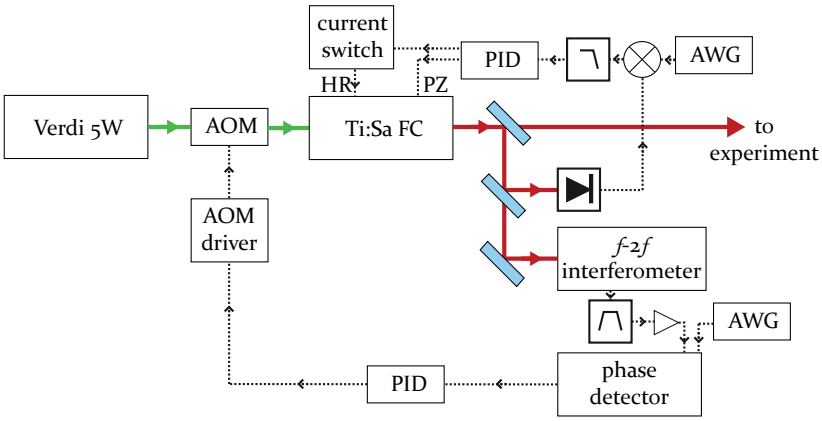

Figure 3.12: The electronic setup for locking the frequency comb (see text). The f_{rep} is detected on a photodiode. From the output signal the 4^{th} harmonic is filtered, which is then mixed with the output of an arbitrary frequency generator (AWG) that is multiplied by 16. The difference signal from the generator is the input for a PID-controller, which controls a piezo to stabilize the cavity length. For long term temperature stabilization, the voltage on the piezo is used as input for control of the baseplate temperature via heating resistors (HR), to stabilize the cavity length over longer timescales. The f_0 is measured using an f-2f interferometer (Fig. 3.16). This signal is filtered using a bandpass filter. The phase difference between the f_0 and the output from an arbitrary frequency generator (AWG) is measured, and feedback on the AOM is provided by a PID-controller. For the experiments described in Chapter 7 the AWG was replaced by a 3 GHz function generator, to which the 16^{th} harmonic of f_{rep} is locked (see text).

In the experiments measuring the $4s\,^2\mathrm{S}_{1/2}-4p\,^2\mathrm{P}_{1/2}$ (Chapter 5) and $4s\,^2\mathrm{S}_{1/2}-4p\,^2\mathrm{P}_{3/2}$ (Chapter 6) transitions in $^{40}\mathrm{Ca}^+$, the generator providing the reference frequency was an 80 MHz Agilent 33250A Arbitrary Waveform Generator, multiplied by sixteen in order to generate the fourth harmonic of the repetition frequencies around 180 MHz. For the experiment on the clock transition in calcium (Chapter 7), this generator is replaced by a 3 GHz Agilent function generator, to which the 16^{th} harmonic of the repetition frequency is locked. Both generators are locked to a rubidium atomic clock (Stanford Research Systems PRS-10), which is referenced to the (caesium-based) Global Positioning System (GPS). On short timescales of the order of seconds, the rubidium clock will have a stability that is orders of magnitude better then the GPS. However, for averaging times over longer timescales of several hours the stability of GPS will be higher (Fig. 3.13). The rubidium clock is corrected based on the GPS signal for long timescales, improving the accuracy for averaging over large time spans. This method makes

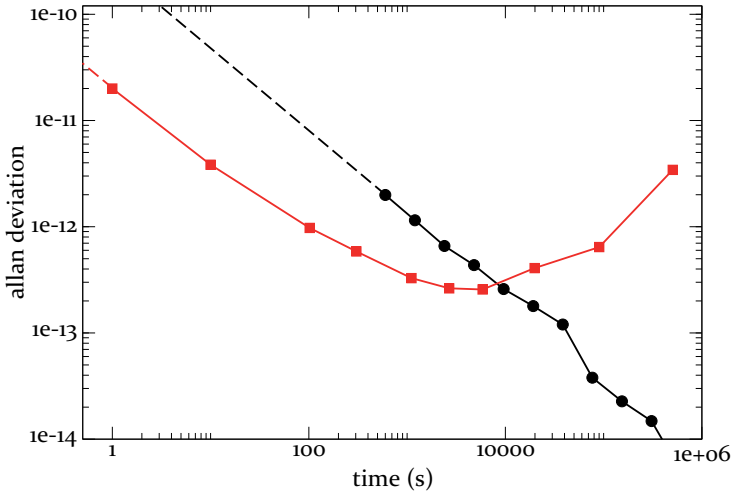

Figure 3.13: Allan deviation for both the rubidium clock (squares) and GPS (circles). The rubidium clock Allan deviation is based on the manufacturer specifications. The GPS data is based on the NIST Boulder GPS data archive [111] for the month november 2009.

measurements possible with an uncertainty of a few parts in 10^{-13} for averaging over 24 hours [109]. The highest achieved accuracy presented in this thesis is 7×10^{-10} on a transition frequency of 762 THz. Measurements with a higher precision have been demonstrated in our laboratory using a fiber-based frequency comb, locked to the same GPS-disciplined rubidium clock. For measurements on the $1s2s\,^3\mathrm{S}_1 - 1s2s\,^1\mathrm{S}_0$ (magnetic dipole) transition in ^{4}He at 193 THz, a precision of 10^{-11} on averaging over ~ 100 s was achieved [110].

The second frequency to be controlled in a comb laser is the carrier-envelope offset frequency. It is detected using a so-called f-$2f$-interferometer [6, 8]. The principle behind this measurement device can be explained in the frequency domain picture: The comb consists of modes which are exactly equally spaced, with the n$^{\mathrm{th}}$ mode at $f_n = f_{ceo} + n \times f_{rep}$. If this comb is upconverted by sum frequency mixing, the resulting comb structure has modes at $f_{ceo} = 2 \times f_{ceo} + m \times f_{rep}$, where m is an integer. In an octave spanning comb, these two can be overlapped on a photodiode to generate a beat signal, containing the f_{ceo} (Fig. 3.14). Frequency combs that directly provide an octave-spanning spectrum can be constructed, and in this case the f_{ceo} is detected with a relatively simple scheme [112–114]. However, even with less than one octave from the oscillator a supercontinuum spanning over an octave can be generated in a photonic crystal fiber, while maintaining the comb structure [115, 116]. Such a broadened spectrum,

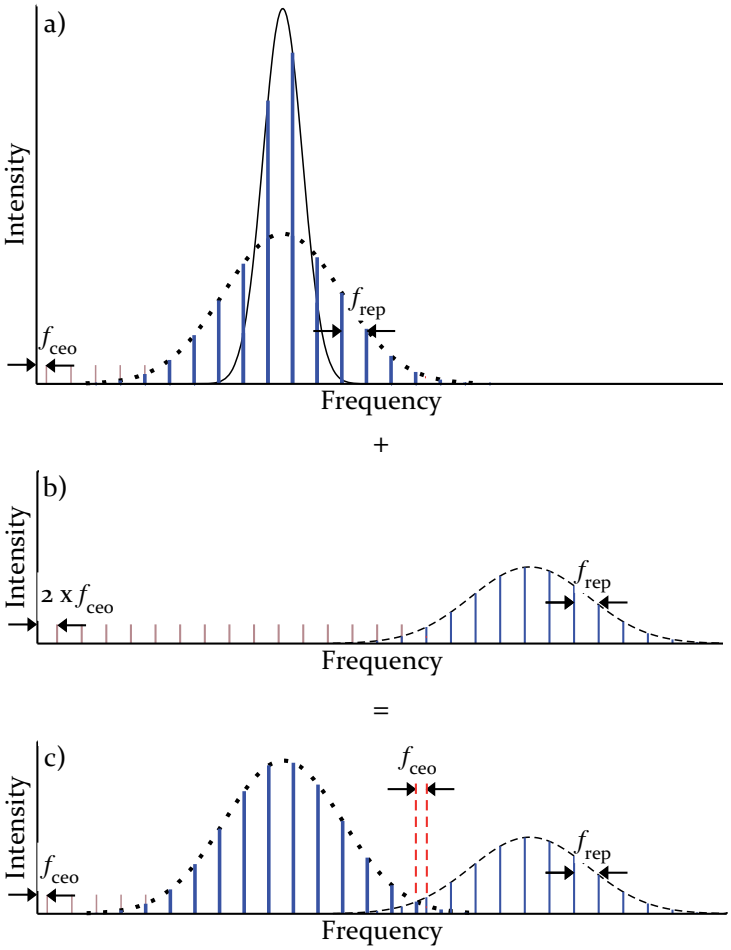

Figure 3.14:
(a) The frequency comb spectrum (solid line) is broadened in a photonic crystal fiber to an octave-spanning spectrum (dotted line). In this process both f_{rep} and f_{ceo} are unchanged. The comb modes are depicted by vertical lines. Only a few comb modes are indicated to show the principle. In reality, the spectrum of the frequency comb consists of $\sim 10^6$ modes.
(b) The broadened spectrum (dotted line in (a)) is frequency doubled, resulting in a spectrum at twice the frequency (dashed line). While the repetition frequency remains the same, the offset frequency is doubled. The frequency doubled spectrum thus has an $f'_{ceo} = 2 \times f_{ceo}$.
(c) A beat note is generated by overlapping the broadened and frequency doubled spectra onto an avalanche photodiode. This signal yields the carrier-envelope offset frequency f_{ceo}.

employed for f_{ceo}-detection, is shown in Fig. 3.15. The setup for measuring f_{ceo} is depicted in Fig. 3.16. The broadened spectrum generated in the photonic crystal fiber is focused in a BBO-crystal to generate the second harmonic of the low-frequency part of the spectrum. The fundamental and doubled spectrum have orthogonal polarizations, and travel through the two arms of an interferometer after being seperated by a polarizing beamsplitter. One of the end mirrors of the interferometer is mounted on a translation stage in to adjust the temporal overlap between the two spectra. The polarization states of the fundamental and frequency doubled signals are projected onto a common axis using a half-wave plate and a polarizing beamsplitter, after which the beat signal is detected on an avalanche photodiode.

Coarse adjustment of f_{ceo} can be made by changing the amount of fused silica in the cavity by shifting the position of a wedge in the laser. For automatic feedback, the pump intensity is employed to control the phase slip between carrier and envelope from pulse to pulse [117, 118]. This dependence is due to the Kerr effect (section 3.2.1) for an octave-spanning Ti:Sa frequency comb [119, 120]. The Kerr effect as described previously has an intensity dependent refractive index, and as such an intensity dependent difference between the phase and group velocity, which in turn changes the phase shift from pulse to pulse [121]. In addition, the time dependence of the Kerr effect needs to be taken into acount, which results from the time-dependence of the non-linear polarization. This leads to an effect called self-steepening, causing a shift in the peak of the pulse compared to the carrier wave, and in this way changes the carrier-envelope phase shift [103, 122, 123]. The combination of these two effects provides the observed change in f_{ceo} on changing the intensity.

An acousto-optic modulator (AOM) is used to change the pump intensity and provide a feedback on f_{ceo}. The phase difference between an Arbitrary Waveform Generator (Agilent 33250A) and the filtered beat signal is detected, and sent to a PID-controller which generates the feedback signal to the AOM driver. An example of the locked f_{ceo}-signal is shown in Fig. 3.17.

3.3.3 Scanning a frequency comb

In order to scan a frequency comb over the transition to be measured, either the carrier-envelope offset frequency or the repetition frequency can be varied. The latter has the main advantage that the scan step Δf_{rep} is multiplied by the mode number n, meaning that only a very small range of f_{rep} has to be scanned in order to make a wide scan around the transition frequency f_{trans} to be measured. To give an example, for the $4s\,^2\mathrm{S}_{1/2} - 4p\,^2\mathrm{P}_{3/2}$ transition at 762 THz,

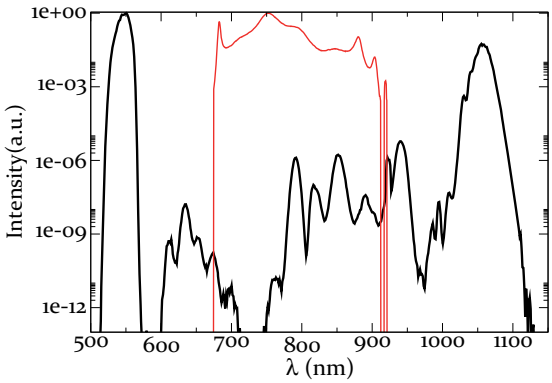

Figure 3.15: The spectrum from the frequency comb (thin trace) is broadened in a non-linear fiber to an octave spanning spectrum (thick trace).

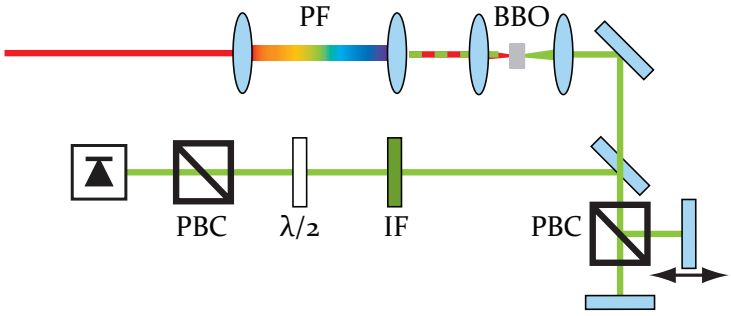

Figure 3.16: Schematic of the $f-2f$ interferometer as used for the f_{ceo}-detection. PF=photonic fiber, PBC=polarizing beamsplitter cube, IF=532 nm interference filter, $\lambda/2$=half-wave plate. One of the mirrors is mounted on a translation stage (indicated with an arrow) to correct for a delay between the doubled and broadened spectrum.

at $f_{rep} = 180\,\text{MHz}$, the mode number is $n = 4.2 \times 10^6$. Therefore, a scan of the repetition frequency of only $42.5\,\text{Hz}$ is enough to scan over the full repetition rate of $180\,\text{MHz}$ at the transition frequency. In order to achieve such a scan the laser cavity only needs to be scanned over a length $\Delta L = 0.4\,\mu\text{m}$, which is easily achieved using the piezo-electric transducer that is also used for locking the comb repetition rate.

On scanning the repetition frequency over a large frequency range, several consecutive comb modes come into resonance with the transition frequency. A resonance will occur for:

$$f_{ceo} + n \times f_{rep,n} = f_{trans} \tag{3.16}$$

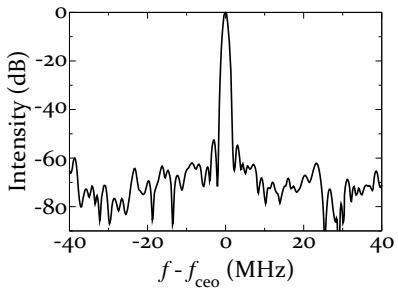

(a) The locked f_{ceo} as measured on a spectrum analyzer with a video bandwidth of 1 Hz, and a resolution bandwidth of 1 Hz. The observed bandwidth is resolution limited. $f_{ceo} = 38.2$ MHz.

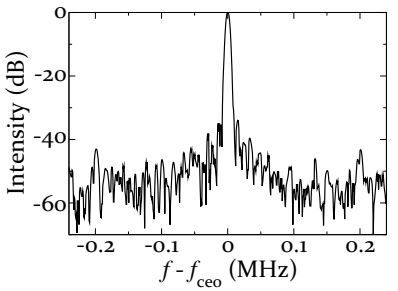

(b) Here the same beatnote as in Fig. 3.17(a) is shown, over a broader frequency range, with a resolution bandwidth of 4.7 kHz and a video bandwidth of 4.7 kHz. $f_{ceo} = 38.2$ MHz

Figure 3.17: The measured f_{ceo} signal, measured on two frequency scales, showing the good signal-to-noise ratio for the beatnote.

If mode m is resonant with the transition at a repetition frequency of $f_{rep,m}$, then the mode number $m-i$ is resonant for $f_{rep,m-i} = \frac{1}{1-i/m} \times f_{rep,m}$. In the signal that is acquired by scanning several comb modes over the transition (as is shown in Fig. 3.18) the spacing between the modes m and $m-i$ is thus:

$$\Delta f = \frac{1}{m/i - 1} \times f_{rep,m} \approx i/m \times f_{rep,m} \tag{3.17}$$

Because of this well-controlled and known structure of the frequency comb, a scan containing several resonant comb modes in sequence can be fit collectively to give a single transition frequency. This method of scanning several comb modes over the transition frequency of interest is used for the direct frequency comb spectroscopy of the $4s\,^2\mathrm{S}_{1/2} - 4p\,^2\mathrm{P}_{3/2}$-transition in $^{40}\mathrm{Ca}^+$, which is described in Chapter 6.

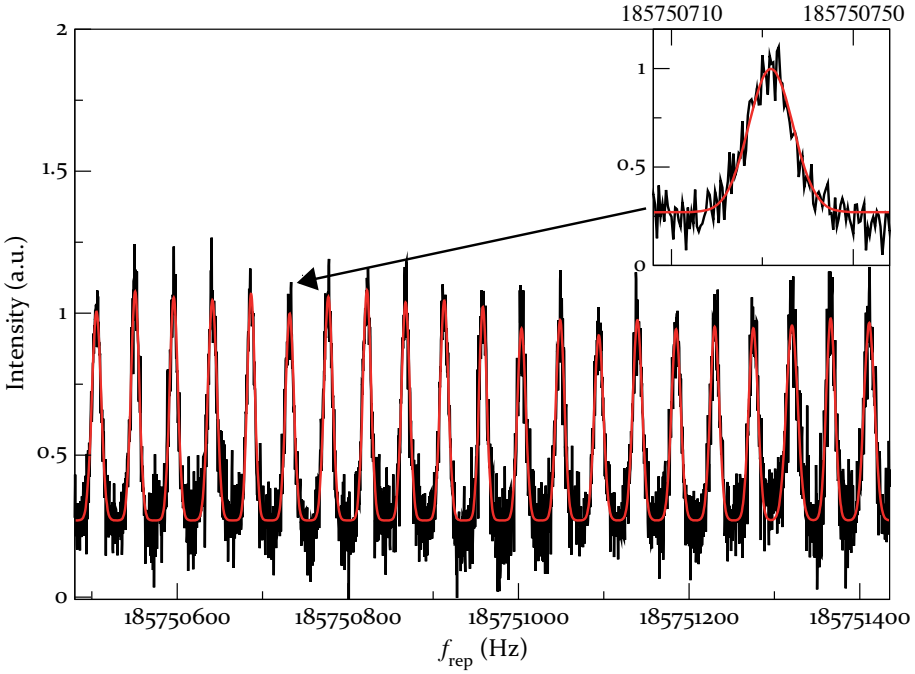

Figure 3.18: The signal for scanning 21 comb modes over the $4s\,^2\mathrm{S}_{1/2} - 4p\,^2\mathrm{P}_{3/2}$-transition, after correction for decay. The whole scan is collectively fitted. In the inset the fit result for one of the peaks is shown.

Chapter 4

Precision spectroscopy and the frequency comb

The current standard of time is, by definition, based on a transition in the caesium atom*. By using this element in an atomic fountain, the best working caesium clocks can now give an accuracy of 3.3×10^{-16} [125, 126]. However, work is in progress towards even more accurate standards, based on other trapped and cooled atoms or ions which could lead to a redefinition of the SI second in the near future. The impressive progress which was made in recent years is summarized in Fig. 4.1, now leading to clocks based on a trapped ions with an accuracy at the 10^{-17}-level [1]. A big advantage of these clocks over the caesium fountain clocks lies in the much higher transition frequency used. While the transition in caesium lies at 9 192 631 770 Hz, the 'clock' transition in for example $^{27}Al^{+}$ is at $\nu = 1\,121\,015\,393\,207\,857.4(7)$ Hz [14]. The five orders of magnitude higher transition frequency could in principle significantly improve the ion clock stability on short timescales. The counting of such high frequencies has been made possible by the invention of the frequency comb laser [6–8]. With a frequency comb, optical transitions frequencies can be down-converted to radio frequencies (RF), which can be electronically counted. This division is not only useful for defining new standards, but also for measuring other optical transition frequencies. Since the comb links the optical to the RF domain, the transition to be measured can be linked to the caesium standard. In addition, it enables relative measurements between transitions in the optical domain.

*Since 1968 'The second is the duration of 9 192 631 770 periods of the radiation corresponding to the transition between the two hyperfine levels of the ground state of the caesium 133 atom' [124]. In 1997 the definition was altered by adding the requirement of the atom being at rest: 'This definition refers to a caesium atom at rest at a temperature of 0 K'.

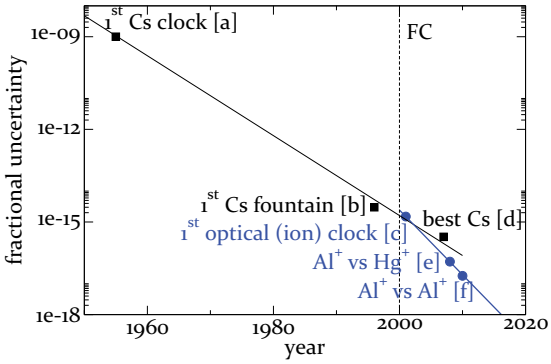

Figure 4.1: Overview of some important developments in high precision spectroscopy. The dashed line indicates the invention of the frequency comb (FC). The points in the graph represent: [a] The first caesium clock [127], [b] The first caesium fountain [128], [c] The first optical ion clock [20], [d] The current state-of-the-art caesium standard [125], [e] A relative measurement of two ion clocks with a fractional uncertainty of 10^{-17} [14], [f] Current record for accuracy [1].

4.1 Accuracy and stability

The performance of a frequency standard is judged both by the precision that can ultimately be achieved on long averaging times, and by the stability of the clockwork indicating the fluctuations of the output frequency. The stability is usually expressed in terms of Allan deviation σ_y [129], which for a normalized frequency difference $y(\tau)$ is defined through the Allan variance σ_y^2:

$$(\sigma_y(\tau))^2 = \sum_{i=1}^{N-1} (y_{i+1}(\tau) - y_i(\tau))^2/(2N-2) \tag{4.1}$$

So for a sample averaging time τ in a total measurement of duration $N \times \tau$, the Allan deviation is an average frequency deviation between two consecutive points in the sample. In the case where a frequency standard is based on an atomic transition, this deviation can also be expressed in terms of measurement parameters [41]:

$$\sigma_y(\tau) = \frac{1}{Q\,S/N}\sqrt{\frac{T_c}{\tau}} \tag{4.2}$$

In this equation $Q = f_{trans}/\Delta f_{FWHM}$ is the quality factor of the atomic transition, S/N is the signal-to-noise ratio and T_c is the cycle time needed for measuring the transition frequency in the ion. From formula (4.2) it follows that a

clock based on a narrow optical transition in a trapped ion can have a much faster realization of a standard than caesium, due to its much higher transition frequency compared to the natural linewidth and resulting higher quality factor.

The second characteristic for a frequency standard, the accuracy, refers to how well the clock agrees with the SI-definition of the second. The transition frequency can be well determined at relative uncertainties down to 10^{-15}, for which caesium clocks (on which the definition of the second is based) can be built. However, for the best available ion clock the optical frequency measurement is now limited by the realization of the unit of time. Therefore, the ultimate performance of such a clock can only be expressed in a relative uncertainty between two of these clocks, as for example has been done between an aluminium and a mercury single ion optical clock [14] or between two aluminium single ion optical clocks [1]. Some examples of the highest achieved accuracies for both Cs-standards and ion clocks over the years are represented in Fig. 4.1.

4.2 Calibrating a probe laser against the frequency comb

The frequency comb is a very versatile tool for spectroscopy due to the combination of a very wide bandwidth and the narrow width of the individual modes. The combs described in this thesis can have a spectral width of $>$ 200 nm (Fig. 3.8 and 3.10), while the individual modes have a width of $\approx$ 2 MHz FWHM. Since the absolute frequencies of the comb modes are very well controlled and known (see section 3.3.2) it can be used as a 'ruler': To determine the unknown frequency of a cw laser, it is measured against the frequency of the comb modes (Fig. 4.2). This is done by mixing the cw laser with a frequency comb mode to generate a beat signal. The two lasers are spatially overlapped onto an avalanche photodiode (in a setup as depicted in Fig. 5.6), where the beat between the cw laser and the modes of the combs is recorded. An example of such a beat signal between a cw Ti:Sa ring laser at 729 nm and a Ti:Sa frequency comb is shown in Fig. 4.3.

From the beat between the two lasers the frequency of the unknown laser f_{cw} can be determined by the formula:

$$f_{cw} = \pm f_{ceo} + n \times f_{rep} \pm f_{beat} \tag{4.3}$$

There are a few factors in this equation which are not directly obtained from the beat measurement, which are the signs in front of f_{ceo} and f_{beat} and the mode number. The sign of the beat frequency f_{beat} can be determined by keeping the cw laser frequency locked to the same position (within a few MHz will usually be enough), while scanning the repetition frequency f_{rep}. If the beat results from

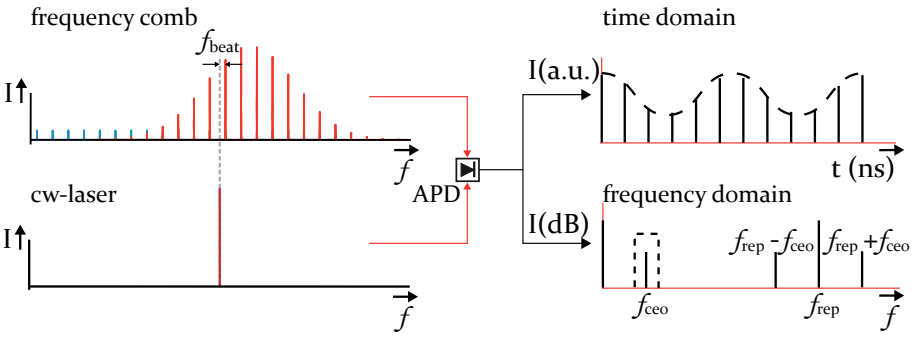

Figure 4.2: The principle of measuring the frequency of a cw-laser with a frequency comb: The comb consists of many modes over a broad wavelength range (schematically depicted in the upper spectrum), while the cw laser will have a very narrow, single mode, spectrum (depicted in the lower spectrum). By combining the two laser beams on an avalanche photodiode (APD) the beat signal between the two can be measured. In the time domain the beat signal appears as a modulation of the pulses, at the frequency of the beat. In the frequency domain, this frequency (and its integer multiples) will manifest itself as a narrow peak. A convenient frequency (in our experiments the one closest to zero) is filtered out with a bandpass filter and measured using an RF counter.

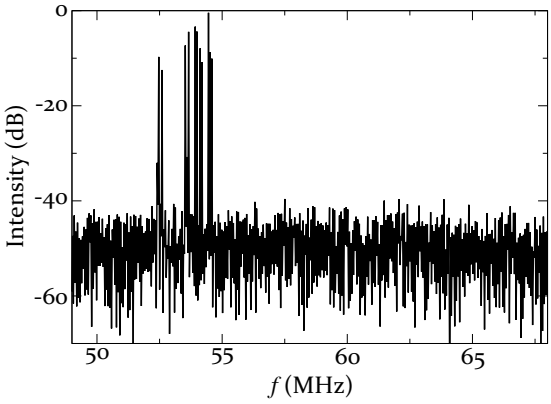

Figure 4.3: An example of the beatnote between an 899 Coherent Ti:Sa ring laser (stabilized on its reference cavity) and the frequency comb, measured with an RF spectrum analyzer with RBW=20 kHz, VBW=20 kHz, and a sweeptime of 50 ms. The frequency of the cw Ti:Sa laser fluctuates on a timescale much faster than the sweep time, resulting in the multiple peak structure in the recorded beatnote.

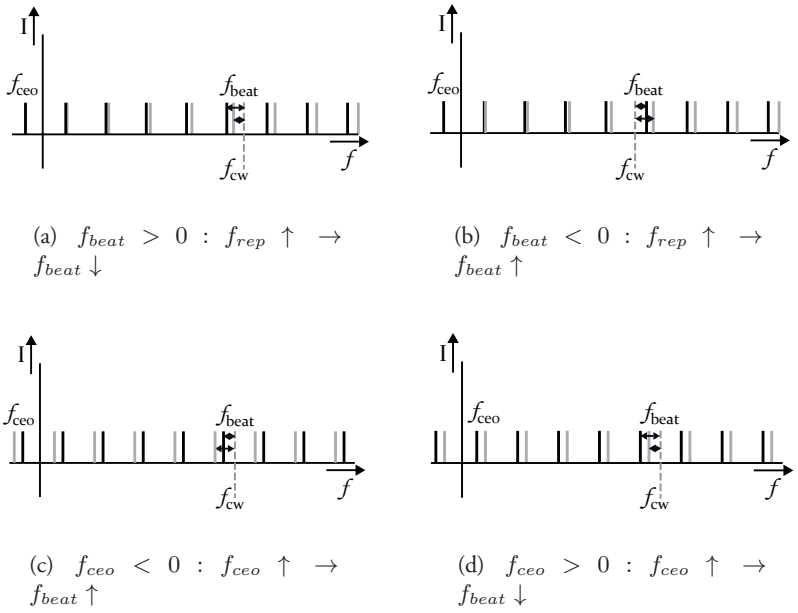

(a) $f_{beat} > 0 : f_{rep} \uparrow \rightarrow f_{beat} \downarrow$

(b) $f_{beat} < 0 : f_{rep} \uparrow \rightarrow f_{beat} \uparrow$

(c) $f_{ceo} < 0 : f_{ceo} \uparrow \rightarrow f_{beat} \uparrow$

(d) $f_{ceo} > 0 : f_{ceo} \uparrow \rightarrow f_{beat} \downarrow$

Figure 4.4: The effect of changing f_{rep} and f_{ceo} on f_{beat}. In figures (a) and (b) f_{rep} is increased (from the black to the grey bars), resulting in a de- (a) or increase (b) of f_{beat} (indicated by arrows) depending on the sign of f_{beat}. In figures (c) and (d) f_{ceo} is increased (from the black to the grey bars), resulting in an in- (c) or decrease (d) of f_{beat} depending on the sign of f_{ceo}.

a mode below the cw-laser mode, then on increasing f_{rep}, f_{beat} will decrease (Fig. 4.4(a)). If on the other hand the cw-laser mode is at a lower frequency than the corresponding comb mode, then on increasing f_{rep}, f_{beat} will increase (Fig. 4.4(b)). The carrier envelope offset frequency can subsequently be determined in a similar manner by changing f_{ceo} while again keeping the laser frequency constant, with f_{beat} now of known sign (Fig. 4.4(c) and 4.4(d)). The frequency f_{ceo} can also be determined by beating a laser of known frequency to the comb. Once the sign of f_{ceo} has been determined, it can be deduced from the direction of the PID feedback, which remains the same if the sign of f_{ceo} does not change. The measurements described in this thesis were performed with an $f_{ceo} < 0$.

The other unknown in equation 4.3 is the mode number n, or in other words the determination of the mode closest to the cw laser mode. If the frequency that needs to be determined is known with an accuracy well within half the repetition

frequency of the comb, the mode number can be assigned with confidence for measurements at a single repetition frequency. Another option is to measure the frequency of the cw-laser with a well-calibrated wavemeter. If these two options are not available, the correct mode number can be determined by performing the calibration at a number of different repetition frequencies. The output of a measurement will be a beat frequency (with known sign), at a known f_{ceo} and f_{rep}. From this measurement a series of possible laser frequencies can be calculated for several possible values of n (indicated by a single set in Fig. 4.5). This measurement can then be repeated at other repetition frequencies. For each of these measurements a set of possible laser frequencies is calculated, based on equation (4.3) with different mode numbers. At the correctly assigned comb mode the values will be the same, while for neigboring comb modes the calculated frequencies the numbers do not match. Depending on the spacing between the sets and the number of sets, there will be are several frequencies where the different sets give the same value within the measurement accuracy. The spacing between these points can be increased by adding measurements at different frequencies if needed. However, for the sets shown in Fig. 4.5 the next crossing already deviates 5 GHz from the assigned value f_0 for a measurement accuracy < 5 MHz. Usually there will be sufficiently accurate data available to determine the transition frequency within this 5 GHz.

4.3 Direct frequency comb spectroscopy

4.3.1 Atomic one- and two-photon transitions

Frequency combs have had a great impact on the development of very precise spectroscopy. The spectroscopy of so-called clock transitions in trapped ions to an accuracy at the 10^{-17}-level was made possible by the achievement of frequency combs with Hz-level linewidths (and beyond) [1, 130]. Direct frequency comb spectroscopy (DFCS) using the comb at the full repetition rate, for excitation of a one-photon transition, can be treated similar to cw-excitation: One of the comb modes is located at approximately the transition frequency, and therefore excites the electronic transition. Excitation rates are determined by the power in this one comb mode, while the other modes only contribute to the AC-Stark shift of the line and the background signal. For a two-photon transition, in principle all

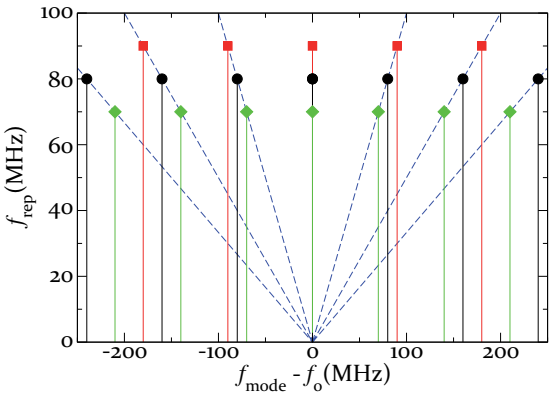

Figure 4.5: Schematic example of the principle of mode determination by changing the f_{rep}: Three different sets of possible frequencies for the calibrated cw-laser are shown (squares, circles and triangles), measured at a repetition frequency as shown on the y-axis. The different positions on the x-axis indicate several possibilities for the frequencies (depending on the mode number), relative to a certain frequency f_0. The frequencies determined at the different f_{rep} give the same value for the mode number at f_0, which thus is the frequency of the cw laser. The slopes between the points for the different repetition frequencies with the same Δn will intersect at the laser frequency at $f_{rep} = 0$ (dashed lines).

comb modes can contribute, because different comb modes can add up to the same frequency for two-photon excitation (Fig. 4.6).†

The direct excitation of transitions with a frequency comb laser was first performed in 2004 on rubidium [131] and in 2005 on krypton [132]. This early work on DFCS already points out many of the advantages of DFCS. The work on rubidium shows that a broad spectrum can be covered in a single scan over one repetition rate. The krypton-experiment shows the application of frequency combs for spectroscopy at short wavelengths: The frequency comb provides short pulses in the time domain, with which high peak powers can be obtained. By using nonlinear effects such as sum-frequency mixing and high-harmonic generation, wavelengths can be obtained which are out of reach of cw-lasers. This approach has now been extended to vacuum ultraviolet (VUV) [133] and extreme ultraviolet (XUV) [134] wavelengths.

Since these first results, direct frequency comb spectroscopy has been demonstrated in several experiments (an overview up to 2008 is given in [135]). A mea-

†Such an experiment with counter-propagating beams will not be entirely Doppler free anymore, but will have a Doppler shift depending on the used bandwidth.

(a) (b)

Figure 4.6: The difference between one- and two-photon spectroscopy using a frequency comb. For one-photon spectroscopy, only one comb mode is resonant at a time (figure (a)). In the case of two-photon excitation, several combinations of comb modes can add up to the same transition frequency (figure (b)).

surement that is particularly worth mentioning in the view of this thesis was performed by Fortier *et al.* in 2006. They demonstrated the first direct frequency comb spectroscopy on a dipole-forbidden transition, the $4s^2\,{}^1\mathrm{S}_0 - 4s4p\,{}^3\mathrm{P}_1$ transition in cold calcium atoms (with a natural linewidth of 374 Hz) [136]. In a later experiment they calibrated the $4s4p\,{}^3\mathrm{P}_1 - 4s5s\,{}^3\mathrm{S}_1$ transition, where the transition frequency was measured at an accuracy of 1×10^{-10} [137]. These experiments are a first demonstration of the possibility of exciting a narrow clock transition using direct frequency comb spectroscopy. We have demonstrated direct frequency comb spectroscopy on a significantly weaker transition [138]. We have measured the $4s\,{}^2\mathrm{S}_{1/2} - 3d\,{}^2\mathrm{D}_{5/2}$ transition frequency in ${}^{40}\mathrm{Ca}^+$ (which has a natural linewidth of 0.14 Hz), as is described in detail in Chapter 7.

4.3.2 Molecular fingerprinting

The signal obtained by direct frequency comb spectroscopy repeats over every f_{rep}. This repetition complicates the unfolding of the spectrum when many lines are recorded simultaneously over a broad spectrum, as is the case for molecular spectra. This issue can be overcome by using a high (1 GHz) repetition rate frequency comb, in combination with a so-called Virtually Imaged Phase Array (VIPA) and a grating [139] or a high-finesse cavity [140] to resolve all individual comb modes.

An example of a setup for measuring molecular absorptions using a frequency comb is depicted in Fig. 4.7. Light at around 1.5 μm (a wavelength range where

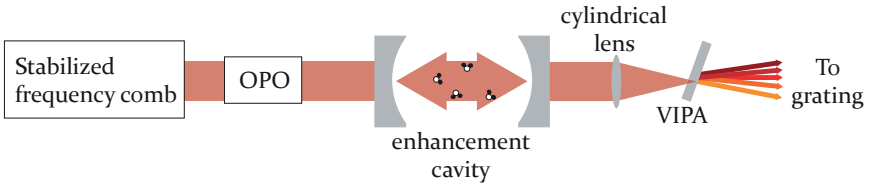

Figure 4.7: A simplified scheme for cavity enhanced frequency comb spectroscopy: Light from a frequency comb is converted to a spectrum around 1.5 μm using an Optical Parametric Oscillator (OPO) (for this purpose also a fiber comb around 1.5 μm can be used). The output light is coupled into an enhancement cavity in order to achieve highly sensitive absorption spectroscopy. The output is resolved into a 2D-array displaying the individual comb modes using a spectrometer consisting of a VIPA (Fig. 4.8) and a grating.

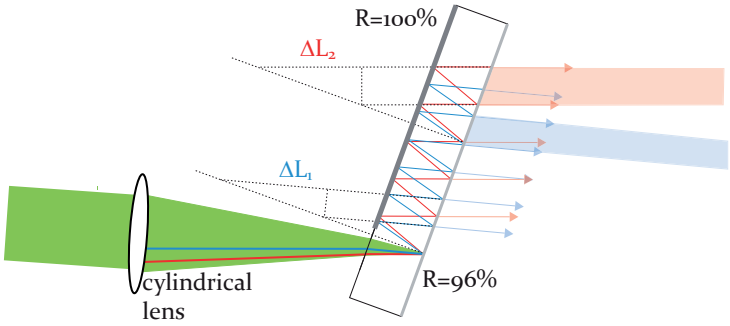

Figure 4.8: The working mechanism in a Virtually Imaged Phase Array (VIPA): The VIPA consists of a thin etalon, with one side coated to have a high reflectivity ($R = 96\%$ in the picture), while the other side is partially coated to provide a 100% reflectivity. The change in refractive index n with wavelength results in different path lengths ($\Delta L = m \times \lambda/n$ for constructive interference. Consequently, the output angle of the VIPA is angle-dependent, providing separation of the comb modes. For a spectrum broader than the free spectral range, the diffraction orders however do still overlap.

many molecular absorptions can be observed) is generated either directly using a fiber frequency comb, or by coupling light from a Ti:Sa frequency comb into an optical parametric oscillator for generation of light at the desired wavelength. The absorption signal is then focused onto a VIPA (Fig. 4.8) to provide angular dispersion, followed by a grating in the perpendicular direction to separate overlapping diffraction orders (see for example [139, 141]). The resulting signal can provide a single shot absorption spectrum over a wide range of wavelengths. In addition, the comb can be scanned over the repetition frequency in order to further resolve the absorption features.

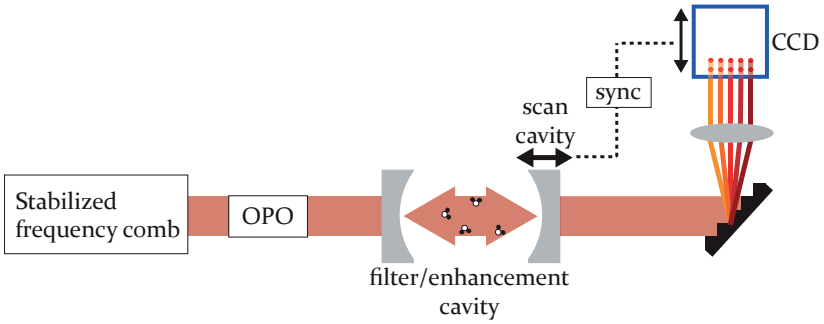

Figure 4.9: Simplified schematic for the application of comb cavity ringdown spectroscopy using a scanning cavity: The comb and OPO are the same as in Fig. 4.7. However, the enhancement cavity now has a length which is no longer exactly matched to the cavity length of the frequency comb. By choosing an appropriate ratio between the enhancement and frequency comb cavity length, the spacing of the transmitted frequency comb is much larger compared to the original comb spectrum, and can be resolved using a grating. By scanning the cavity over one free spectral range, the entire comb spectrum can be recorded.

The drawback of the above described method lies in the use of a static cavity, so that both its length and dispersion must be properly matched in order to obtain a broadband signal containing all of the comb modes. This problem can be overcome by using the cavity itself as the mode filtering device [140, 142]. The spacing between transmitted modes is given by the free spectral range $FSR = 2\pi c/nL$ (where n is the effective refractive index, and L the cavity length). The cavity is designed to have a FSR which is a multiple i/j of the frequency comb repetition rate where j is an integer and $i = j + 1$. As a result only every integer times ith comb mode is transmitted (surpressing the other modes with a cavity with a high enough finesse). The reduced frequency comb can be spectrally resolved on a CCD camera using a grating. By simultaneously scanning the cavity length and the image on the camera, a 2D image of all the comb modes can be obtained. This method suffers from a lower signal compared to the first one, but does gain in simplicity of the setup.

4.3.3 Multiheterodyne spectroscopy

Another method to resolve the individual modes in the comb spectrum involves the application of two frequency combs simultaneously, as suggested by [143] and demonstrated by [144–146]. The so-called multiheterodyne spectroscopy uses the time domain signal in order to observe the frequency domain absorption spec-

trum. In the time domain, the frequency comb shows a pulse shape (where f_{ceo} is omitted for ease of explanation):

$$I(t) = \sum_n C_n \cos(n\omega_{rep}t) \tag{4.4}$$

The frequency dependent absorption spectrum of a medium gives a frequency dependent modulation:

$$I'(t) = \sum_n A_{mod,n} \times C_n \cos(n\omega_{rep}t) \tag{4.5}$$

A beat can be made between such a modulated comb with a repetition frequency $\omega_{rep,1}$ and a second, non-modulated frequency comb, with repetition frequency $\omega_{rep,2}$, resulting in a beat signal:

$$I_{tot}(t) = \frac{1}{2}\sum_{n,m} A_{mod,n}\{\cos(n\omega_{rep,1}t - m\omega_{rep,2}t) + \cos(n\omega_{rep,1}t + m\omega_{rep,2}t)\} \tag{4.6}$$

With a fixed frequency difference $\Delta\omega = \omega_{rep,1} - \omega_{rep,2}$ between the combs, after low-pass filtering, the time signal will read:

$$I_{tot}(t) = \frac{1}{2}\sum_n A_{mod,n} \cos(n\Delta\omega t) \tag{4.7}$$

For which the Fourier transform will give a spectrum:

$$I_{tot}(\omega) = \frac{1}{4}\sum_n A_{mod,n} n\Delta\omega \tag{4.8}$$

The near-infrared spectrum is thus mapped onto an RF-spectrum, which can be mapped back onto the original spectrum mathematically. Since there are no moving parts involved, the scanning can be done very fast (in the order of tens to hundreds of μs [147]), making this a very powerful method to scan over a large frequency range. The fact that two frequency combs are involved does make it more expensive then the previously mentioned methods.

Chapter 5

Frequency metrology on calcium ions

5.1 Introduction

The detection of a possible variation in the fine structure constant α by Webb *et al.* [31] was founded on the so-called many-multiplet method. In that study accurate wavelengths of absorption lines of a number of atoms and ions, observed at high redshift in the line-of-sight of Quasi Stellar Objects (QSO or 'quasars'), are compared with the laboratory (zero redshift) wavelengths of those atomic resonances. Such an analysis may yield a value for $\Delta\alpha/\alpha$ over time spans of many billion years. Improved methods and inclusion of over a hundred of high-redshift absorption systems now have delivered a positive effect with a 5σ significance [148]. However, comparison of highly-accurate single ion optical clocks in the laboratory have yielded results consistent with a zero change, measuring a present-day value of $\dot{\alpha}/\alpha = -1.6 \pm 2.3 \times 10^{-17}$ per year [14].

Echelle-grating spectrometers attached to very large telescopes, provide the opportunity for highly accurate wavelength calibration of astrophysical data, with the prospect of detecting a change in the fine structure constant over cosmological timescales. However, for several spectroscopic lines the absolute wavelength accuracy does not match the level of 10^{-7}, which is feasible in astrophysical observations, bringing about the need for renewed and updated laboratory precision measurements. One of the lines that need a more accurate frequency calibration is the $4s\,^2\mathrm{S}_{1/2} - 4p\,^2\mathrm{P}_{1/2}$ transition in Ca^+ [149], which is the subject of this paper.

In general, trapped calcium ions are studied both for use in very accurate ion clocks [41, 150] and for quantum computation [151, 152] (more information on this subject can be found in Chapter 1). Nevertheless, the $4s\,^2\mathrm{S}_{1/2} - 4p\,^2\mathrm{P}_{1/2}$

transition that is used for Doppler cooling these ions, has been given far less attention. For this transition, often the value $\nu = 25\,191.5182$ cm^{-1} is cited [153]. This frequency is based on a private communication with U. Litzén, who recently recalibrated the corresponding data yielding an updated value of $\nu = 25\,191.519(0.002)$ cm^{-1} [154]. The next best wavelength calibration dates back as far as 1956, with a value $\nu = 25\,191.51(0.13)$ cm^{-1}, obtained by Edlén and Risberg using classical spectroscopy [155].

In the present study, a linear Paul trap is used for confinement of a cloud of calcium ions, while laser cooling is employed to obtain a linewidth equal to twice the natural linewidth of the transition. The cold ions are probed using a second laser beam of lower intensity. Simultaneously, a part of this laser is heterodyned to a frequency comb for absolute frequency calibration.

5.2 Experimental setup and procedures

5.2.1 Ion production and trapping

The calcium ions are trapped in a linear Paul trap (Fig. 5.1) consisting of 4 linear electrodes for radial confinement, and 2 ring electrodes for restriction in the axial direction. These elements are suspended and separated by insulating spacers. The electrode dimensions enable fluorescence collection over a large solid angle of $\approx 0.2\pi$ sr. The four linear electrodes are placed at a distance $r_0 = 4$ mm from the trap axis, and the ring electrodes are 17 mm apart. A radio frequency (RF) voltage V_0 at a frequency $\Omega = 2\pi \times 3.3$ MHz is applied to the electrodes 1 and 4, while the electrodes 2 and 3 are grounded. The characteristic stability parameter of the Mathieu equation, which describes the motion of an ion in an harmonic RF potential, is $q = 2QV_0/m\Omega^2 r_0^2$ [55]. Here Q and m are the charge and mass of the ions respectively. A small stability parameter ($q << 1$) is advantageous to reduce RF heating [78, 79]. However, trap imperfections and micromotion in an extended cloud can still lead to substantial heating of the confined ions [55, 86]. The trap is generally operated with a $V_0 \approx 60$ V, corresponding to $q = 0.04$. The ring electrodes that are held at a constant voltage of typically $V_{DC} = 10$ V create a harmonic potential for axial confinement. The ion trap is described in detail in Chapter 2.

The trap is installed in a vacuum chamber, which is evacuated to a pressure of 2×10^{-9} mbar. Neutral calcium atoms are evaporated from an oven into the linear Paul trap. In the trapping region calcium atoms are resonantly excited to the $4p\,^1\mathrm{P}_1$ level by a frequency-doubled CW (continuous wave) Ti:sapphire ring laser (Coherent 899) producing 422 nm, and subsequently ionized by a frequency

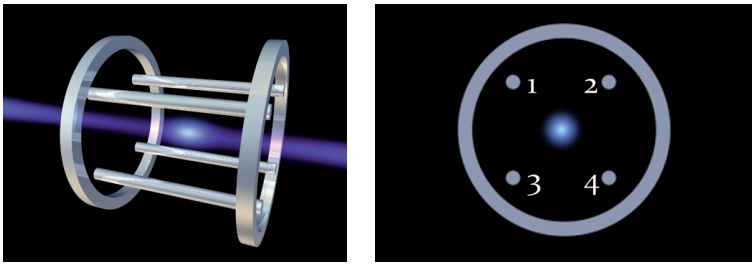

(a) Side view (b) Axial view

Figure 5.1: Electrode configuration for the linear trap. The trap consists of four linear electrodes (labeled 1-4) for radial confinement: A Radio Frequency voltage is put on two diagonally facing rods (1,4), while the other two rods are grounded (2,3). A DC voltage is applied to the ring electrodes for axial confinement.

tripled Nd:YAG (yttrium aluminum garnet) laser operating at 355 nm (Fig. 5.2). The RF source for the trap (Agilent 33120A) is resonantly enhanced and filtered by a helical resonator (with a loaded Q≈140). For diagnostic purposes a Channel Electron Multiplier (CEM) and extraction grid were installed underneath the Paul trap. By pulsed extraction of the ions from the trap with a variable delay and detection on the CEM, the ionization rate and trapping conditions can be probed and optimized.

5.2.2 Doppler cooling to ion cloud crystallization

In order to counteract RF heating and reduce the Doppler width of the measured transition, the ions are laser cooled on the $4s\,^2\mathrm{S}_{1/2} - 4p\,^2\mathrm{P}_{1/2}$ transition (the relevant energy levels are shown in Fig. 5.3). The cooling laser is a 397 nm grating stabilized diode laser ($P = 3$ mW, Toptica DL100). Since the ions in the excited $4p\,^2\mathrm{P}_{1/2}$ state have a 7% probability of decaying to the long-lived $3d\,^2\mathrm{D}_{3/2}$ state, an additional diode laser at 866 nm ($P = 1$ mW, Toptica DL100) is used for repumping.

Excitation of the transition is observed through the emitted fluorescence at 397 nm. Using a 25 mm diameter lens with a focal length of 25 mm inside the vacuum chamber, 5 % of this light is collected. The ion cloud is imaged onto a pinhole to remove background radiation and scattered light from the electrodes, and its fluorescence is detected on a photomultiplier tube (PMT, Philips XP2020Q).

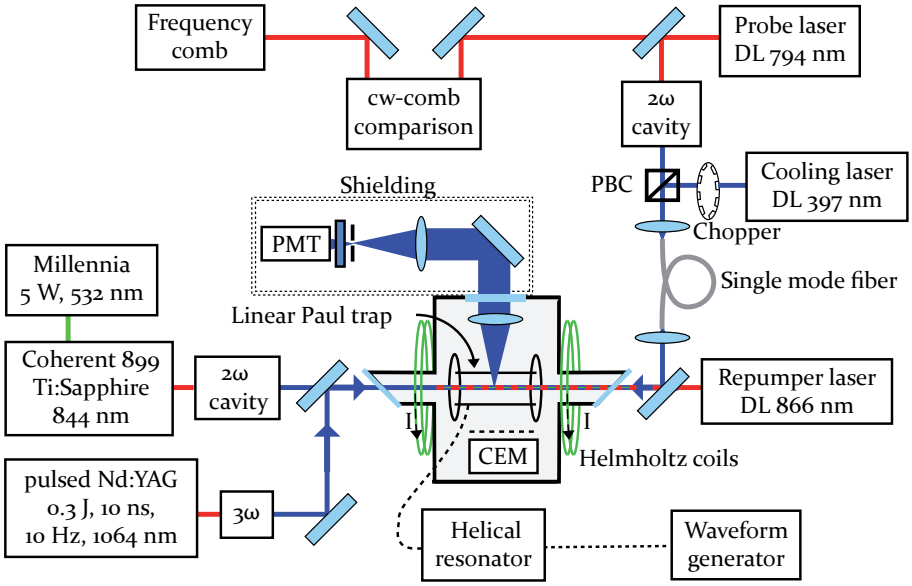

Figure 5.2: Schematic design of the laser system and linear Paul trap. The lens used for focusing the light onto the single mode fiber is a 40 times microscope objective. More details on the frequency doubling can be found in Fig. 5.5. DL=Diode laser, PMT=Photo-Multiplier Tube, 2ω=frequency-doubling setup, 3ω=frequency-tripling setup, PBC=Polarizing Beamsplitter Cube, CEM=Channel Electron Multiplier.

Before being focused into the trapping region, the cooling laser is spatially filtered by a single-mode optical fiber (3M FS-VS-2614, mode field diameter 3.14 μm), which reduces the effective cooling laser power to $P = 1$ mW. The filtering further reduces the background signal due to scattered light from the trap electrodes, which mainly originates from the 397 nm cooling laser. In Fig. 5.4 two excitation spectra of trapped and laser cooled ions are shown, obtained by scanning the cooling laser. Depending on the cooling efficiency (controlled by the repumper detuning), the recorded fluorescence as a function of the cooling laser frequency can follow two characteristic curves [156]. If the ions keep relatively warm and do not crystallize, the profile is a red-shifted, distorted Gaussian (red curve). On the other hand, with sufficient laser cooling, the fluorescence can start out on a similar curve when the cooling laser is far from resonance, until the ions become sufficiently cold and crystalize. This sudden localization of the ions leads to a smaller Doppler width, resulting in a decrease in fluorescence. On further scanning of the cooling laser over the transition, a narrower resonance appears due to the lower temperature of the ions (blue curve). Such a crystallized ion cloud is used

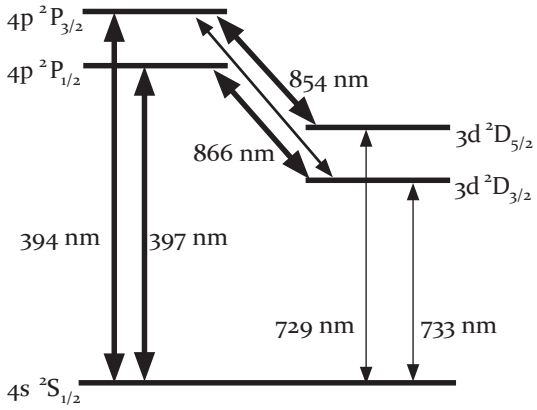

Figure 5.3: Partial energy level diagram of Ca^+

for the spectroscopy to minimize Doppler broadening. Laser cooling is performed with the cooling laser set at detuning $\Delta f \approx 10$ MHz from resonance (locked to a wavemeter (Atos model LM-007) within ≈ 6 MHz), which is approximately half the natural linewidth. The achieved temperature is typically $T \approx 1$ K. This is higher than the Doppler limit of $T = 0.5$ mK, probably due to anharmonicity of the applied electric field or other trap imperfections [55, 86]. The large number of trapped ions (~ 100) magnifies this effect, since the Coulomb repulsion forces the ions away from the more harmonic trap center. The lifetime of the ions in the trap is measured to be $\tau \approx 8$ min by monitoring the fluorescence from the cooling laser.

5.2.3 Spectroscopy and absolute frequency calibration

Because the $4s\,^2\mathrm{S}_{1/2} - 4p\,^2\mathrm{P}_{1/2}$ transition is both the cooling and measured transition, the cooling laser is periodically switched off using a chopper with a duty cycle of 0.5 at a frequency of 0.3 kHz. The fluorescence due to the spectroscopy laser is recorded during these periods. A diode laser at 794 nm (Toptica DL100) is frequency doubled to 397 nm to probe the transition (Fig. 5.5). To minimize heating of the cloud the probe laser intensity is a thousand times weaker than the cooling laser. After spatial filtering a power of only $P \approx 1$ μW remains, which is focused to 0.5 mm diameter in the trap. The induced fluorescence is detected with the imaging system and PMT described previously (Fig. 5.2). The fluores-

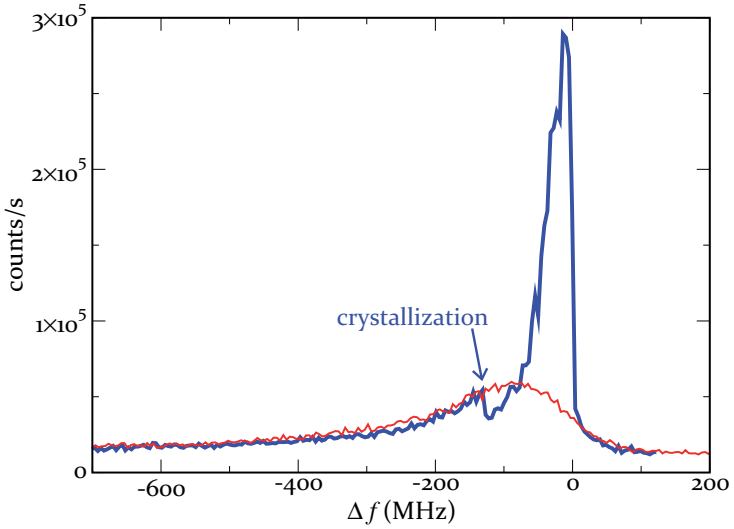

Figure 5.4: Observed fluorescence vs. frequency detuning Δf, on scanning the cooling laser over the $4s\,^2\mathrm{S}_{1/2} - 4p\,^2\mathrm{P}_{1/2}$ transition in Ca^+. Red thin trace: $T_{\mathrm{ions}} \approx 40$ K, blue thick trace: $T_{\mathrm{ions}} \approx 4$ K. The sudden decrease in fluorescence in the blue curve is the typical signature for crystallization of the ion cloud (see text).

cence of both the cooling laser and the spectroscopy laser are separately recorded, using a gating technique synchronized to the chopper in the cooling laser beam. The cooling and probe laser are guided through the same single mode fiber (Fig. 5.2), ensuring good alignment of the weak probe beam onto the cold ion cloud, while also spatially filtering the probe beam. In addition, by monitoring the cooling laser induced fluorescence, ion loss from the probed region can be observed during the scan.

The probe laser is calibrated on an absolute frequency scale by referencing it to a frequency comb (see Chapter 3 and [7, 8]). A frequency comb laser is characterized by two frequencies: The repetition frequency f_{rep} which determines the mode spacing, and the carrier-envelope offset frequency f_{ceo}, that gives the comb its offset from zero frequency. Both frequencies are locked to a Rubidium atomic clock (Stanford Research Systems PRS-10), which is referenced to the Global Positioning System (GPS), fixing the frequency of the n^{th} mode to $f_n = \pm f_{ceo} + n \times f_{rep}$. The Allan deviation of the frequency comb modes is determined from the stability of the repetition rate relative to the clock combined with the stability of the frequency reference. For the typical averaging time of 1 second, the contributions to the Allan deviation are 0.09 and 0.05 MHz respectively. Due to the short

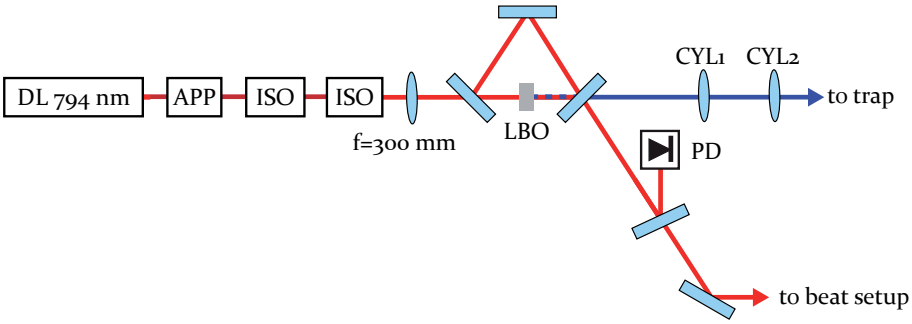

Figure 5.5: The diode laser and doubling cavity as used for the spectroscopy. APP=anamorphic prism pair ISO=Faraday isolator CYL1=cylindrical lens f=70 mm CYL2=cylindrical lens f=100 mm

measurement times, the latter is determined by the stability of the Rubidium reference. The contributions are added up in quadrature to a 1 second Allan deviation of $\sigma = 0.1$ MHz for optical modes at 377 THz, leading to an uncertainty of 0.2 MHz in the calibration at 755 THz. The comb laser operates at a repetition rate of 207 MHz and with a spectrum of 54 nm FWHM around 825 nm.

An interference beat note is generated between the spectroscopy laser and the comb laser modes, by overlapping the near-infrared fundamental output of the spectroscopy laser with the output of the frequency comb laser. The comb light is spectrally filtered using a grating and curved mirror in a 2f configuration (Fig. 5.6) to reduce the amount of comb modes and improve the signal to noise ratio of the recorded beat note with the spectroscopy laser. An avalanche photodiode (Menlo Systems APD210) detects the 40 dB (bandwidth 400 kHz) beat note f_{bn} between the two lasers, which is monitored using a frequency counter (Agilent 53132A, referenced to the aforementioned Rubidium clock).

The laser frequency f_l follows from the locked frequencies f_{ceo}, f_{rep}, and the measured beat frequency f_{bn} through the equation:

$$f_l = \pm f_{bn} + \pm f_{ceo} + n \times f_{rep} \tag{5.1}$$

The sign of f_{bn} can be simply deduced from the known scanning direction of the laser. The scan over the transition was repeated at a different locking frequency of the carrier envelope offset frequency to determine the sign of f_{ceo}. To calibrate the laser frequency the mode number n still has to be determined. The most accurate measurement up to date for the $4s\,^2\mathrm{S}_{1/2} - 4p\,^2\mathrm{P}_{1/2}$ transition in Ca^+ has an uncertainty of 60 MHz, which complicates assigning the mode number

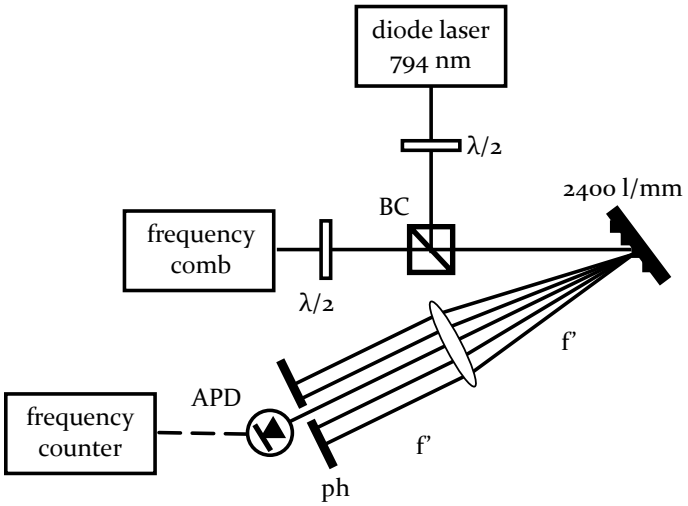

Figure 5.6: Schematic view of the setup for heterodyning the CW diode laser with the frequency comb. The CW laser is overlapped with the comb on a beamsplitter (BC). A grating-based spectral filter is used to reduce the number of comb modes on the detector. For clarity a lens is drawn with focal length $f' = 50\,\mathrm{cm}$, but in practice a curved mirror is used. APD=Avalanche Photodiode, ph=pinhole, $\lambda/2$=half-wave plate.

n with confidence. This is solved by repeating the measurement at two different comb repetition frequencies, sufficiently far apart to distinguish between the adjacent mode numbers. As the transition frequency is independent of the used comb repetition rate, the measurements coincide for a particular mode number n, from which the absolute frequency can be determined (see below). This method is similar to that proposed in [157] and used in [132].

5.2.4 Results

A typical scan of the spectroscopy laser takes about 2 minutes (Fig. 5.7), which is substantial compared to the trap lifetime of $\approx$ 8 min. In order to minimize distortion of the line profile, the spectroscopy signal is corrected for this ion loss, and scans are always performed in both the forward (increasing frequency) and backward (decreasing frequency) direction. Since the cooling is insufficient to reach the natural linewidth of the transition, a Voigt profile, i.e. a convolution of a Gaussian and a Lorentzian is fitted to the data. The width of the Lorentzian is fixed to 22.4 MHz [158], the natural linewidth of the transition. The width of the Gaussian component is fitted, with a typical full width half maximum on the

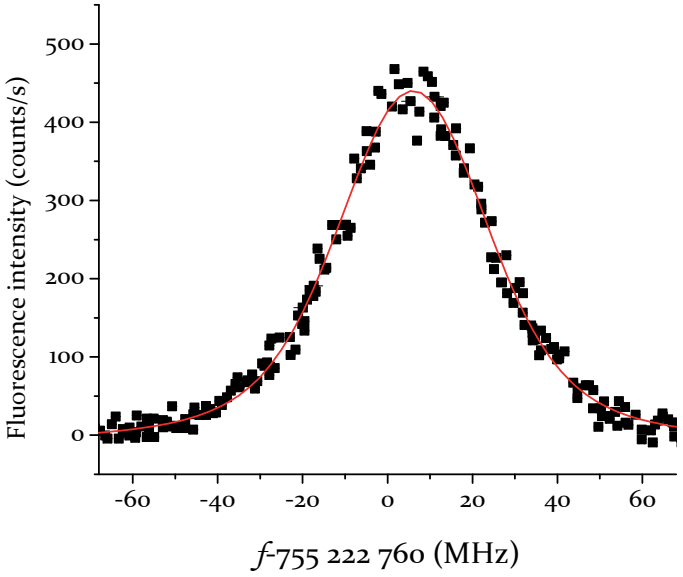

Figure 5.7: An example of the measured fluorescence spectrum for the $4s\,^2\mathrm{S}_{1/2} - 4p\,^2\mathrm{P}_{1/2}$ transition in Ca^+ (black dots) and the corresponding Voigt fit (red line), corrected for the trap loss during the scan.

order of 45 MHz. From this fitted value an ion cloud temperature of $T \approx 1$ K is deduced.

The mode number is determined by measuring the transition frequency using different frequency comb repetition rates of $f_{rep} = 189$ MHz and $f_{rep} = 207$ MHz. This results in two sets of possible transition frequencies (Fig. 5.8). The measurements clearly coincide at a value of $f = 755\,222\,766$ MHz, which is near the literature value of $f = 755\,222\,740(60)$ MHz.

Several effects that can introduce systematic and statistical errors on the transition frequency have been investigated. These include the Stark shifts caused by both the light field and the Paul trap, the stability of the comb modes and the Zeeman shift caused by the earth magnetic field. The respective shifts and statistical uncertainties are tabulated in Table 5.1.

In order to probe the Zeeman shift, a magnetic field is generated in the direction of the laser beam using Helmholtz coils (9 windings, diameter $2r = 19$ cm). For magnetic fields in this direction, if the polarization of the spectroscopy laser is not completely linear, the $\Delta m = \pm 1$ transitions will have a different excitation rate. The Zeeman shift ($\Delta E = g_J m_J \mu_B B$) in the involved energy levels results

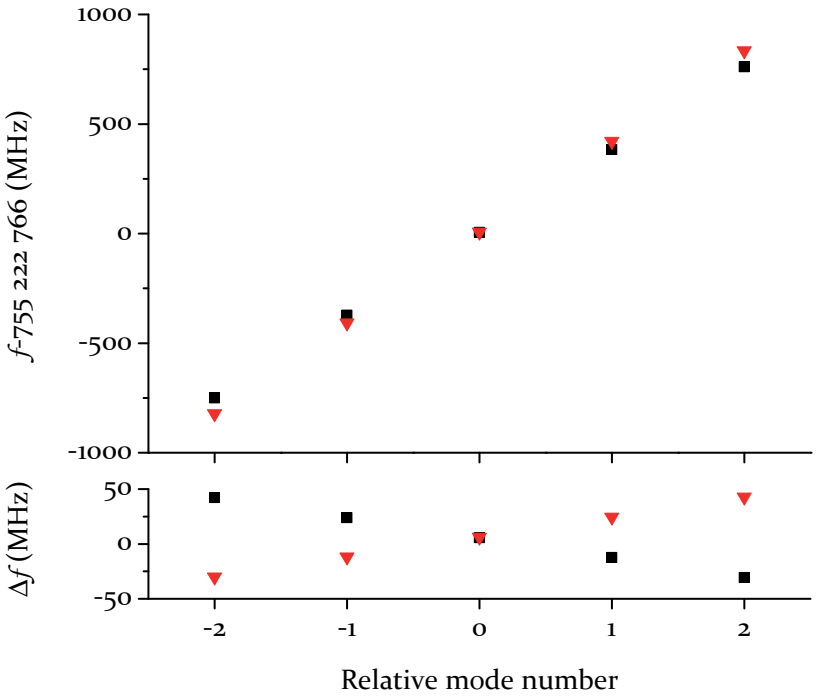

Figure 5.8: Absolute calibration of the $4s\,^2\mathrm{S}_{1/2}-4p\,^2\mathrm{P}_{1/2}$ transition in Ca^+ is performed by finding the coincidence of measurements with two different frequency comb repetion rates of 189 MHz (circles) and 207 MHz (triangles). The depicted transition frequency $f = 2 \times f_l$, since the laser frequency is measured in the infrared, after which the laser is frequency doubled for the spectroscopy. Consequently the spacing between adjacent points in the picture is $2 \times f_{rep}$. The upper graph shows the frequency dependence on the choice of mode number. The lower graph shows the frequency difference between the points in the upper graph, with $\Delta f = f - 755\,222\,766\ \mathrm{MHz} - 2 \times n' \times 198\ \mathrm{MHz}$, where n' is the relative mode number (error bars are smaller than the point size).

in an expected magnetic field dependent shift in the transition frequency of ± 19 kHz/μT for the $\Delta m = \pm 1$ transitions. For perpendicular magnetic field components no shifts of the line center, but only broadening can be expected to first order. These are therefore not considered.

The line center of the transition as a function of the applied external fields was recorded for three different polarizations: right- and left-circular (σ^+ and σ^- respectively) and linear ($= \sigma^+ + \sigma^-$). The result is shown in Fig. 5.9. Linear fits to the data show Zeeman coefficients of 19(1) kHz/μT and 15(1)

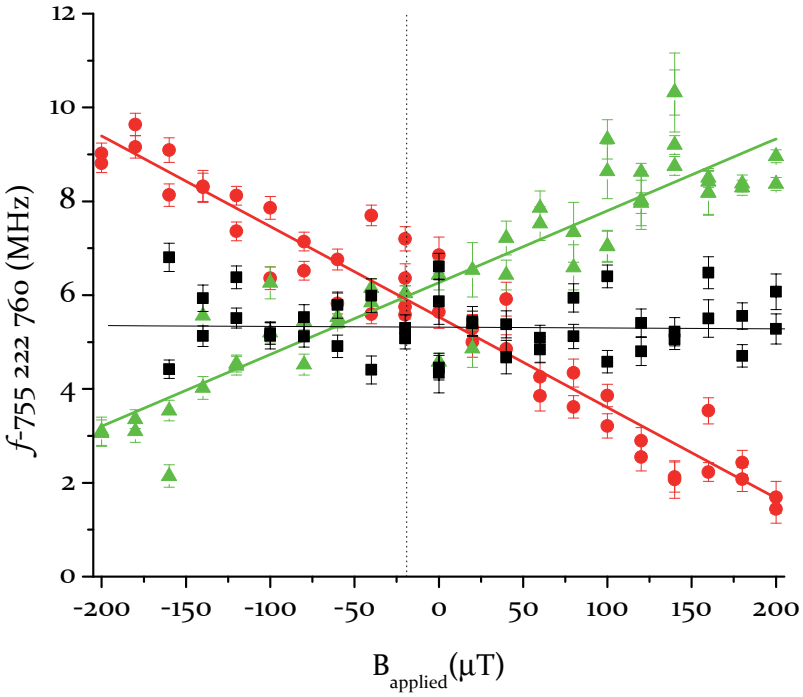

Figure 5.9: Transition frequency for the $4s\,^2\mathrm{S}_{1/2} - 4p\,^2\mathrm{P}_{1/2}$ transition in Ca^+ with respect to an applied magnetic field $B_{applied}$ (not yet corrected for systematic shifts). Three different polarizations were used (see text): right-circular (σ^+, green triangles), left-circular (σ^-, red circles) and linearly polarized light ($\sigma^+ + \sigma^-$, black squares). The dotted line indicates the value of the applied field where $B_{applied} = -B_{earth}$.

kHz/μT for the σ^+ and σ^- components. The deviation of the latter from the calculated value can be attributed to an inaccurate control of the polarization in the interaction region, due to depolarization by the Brewster angled vacuum windows. For excitation with linear polarization, a first order Zeeman coefficient of 0.0 kHz/μT is expected, and it was correspondingly measured to be 0.2(1.0) kHz/μT. Therefore the final calibration of the $4s\,^2\mathrm{S}_{1/2} - 4p\,^2\mathrm{P}_{1/2}$ transition is based on an average over the measurements with linear polarization. The crossing of the curves with σ^+ and σ^- polarization yields the zero total magnetic field at $B_{applied} = -21(6)\ \mu$T (in good agreement with the expected earth magnetic field component of $-19\ \mu$T). Based on the magnetic field uncertainty of 6μT, an upper limit for the total residual Zeeman shift of $6\mu\mathrm{T}\times 0.2(1.0)$ kHz/μT $= 1.2(6.0)$ kHz is calculated, which is negligible.

Effect	Shift (MHz)	1σ Uncertainty (MHz)
Zeeman	0.0	0.0
AC Stark repumper	-0.4	0.6
AC Stark spectroscopy laser	-0.4	0.8
RF Stark effect	0.0	1.2
Comb calibration	0.0	0.2
Statistics		0.6
Total	-0.8	1.7

Table 5.1: Measured systematic shifts and uncertainty budget (1σ). All values in MHz.

AC Stark shifts in the spectroscopy data for both the repumper laser and the probe laser were evaluated by changing their respective intensities. As expected, both shifts were found to be small compared to the the measurement uncertainty ($-0.4(0.6)$ MHz and $-0.4(0.8)$ MHz respectively, Table 5.1). In order to assess possible trap induced shifts, the RF voltage V_0 was varied over a range from 50-200 V. The corresponding shift was measured to be consistent with a zero value: $\Delta f = 0.0(1.2)$ MHz.

The $^{40}\mathrm{Ca}^+$ $4s\,^2\mathrm{S}_{1/2} - 4p\,^2\mathrm{P}_{1/2}$ transition frequency follows from the statistical average of the measurements with linearly polarized light, corrected for the measured shifts. The total measured value adds up to $f = 755\,222\,765.4(0.6) + 0.4(0.6) + 0.4(0.8) + 0.0(1.2) + 0.0(0.0) = 755\,222\,766.2(1.7)$ MHz, with the uncertainties taken in quadrature. The present result is consistent with the most accurate previously reported value of $\nu = 25\,191.519(0.002)$ cm^{-1} ($f = 755\,222\,740(60)$ MHz).

5.3 Conclusions

We have performed an absolute frequency calibration of the $4s\,^2\mathrm{S}_{1/2} - 4p\,^2\mathrm{P}_{1/2}$ transition in $^{40}\mathrm{Ca}^+$ ions in a linear Paul trap, including a study of Zeeman and Stark shifts. The transition was measured to be at $f = 755\,222\,766.2(1.7)$ MHz, in a laser cooled ion cloud of $T \approx 1$ K. The presented value represents more than an order of magnitude improvement over the previous most accurate measurement. This level of accuracy, at $\Delta\lambda/\lambda = 2 \times 10^{-9}$, is such that for any comparison with state-of-the-art astrophysical data, the laboratory value can be considered exact.

The employed technique for trapping and cooling ions will be used for spectroscopy on other ions in the near future. We plan to trap and sympathetically

cool ions such as Mn^+ and Ti^+ with Ca^+. In this way, we expect to reach improvements in energy level calibration of these ions, similar to the demonstrated accuracy for calcium. This will provide accurate laboratory wavelengths for the comparison with high-redshift astronomical data in a search for a possible variation of the fine structure constant over cosmological time scales.

Chapter 6

Direct frequency comb spectroscopy of trapped ions

6.1 Introduction

Optical frequency comb lasers provide a phase coherent link between radio frequency sources and optical frequencies [7, 8]. As a result optical frequencies can be counted, which has made spectroscopy and optical clocks possible with an extremely high accuracy on the order of $10^{-16} - 10^{-17}$ [14, 25]. In most experiments a continuous wave (CW) laser is used as a probe of an atomic or molecular transition, which is then calibrated against a frequency comb (see e.g. [159] for an experiment on atoms, [160] for references to measurements on tightly confined ions, and [47, 161] for measurements on ions in the weak binding limit).

However, frequency combs can also be used for direct excitation, without the need of a CW laser. This is possible because the pulsed output of a comb laser (as seen in the time domain) is equivalent to many equidistant narrow modes in the frequency domain. Direct frequency comb spectroscopy has been demonstrated in beam experiments [132, 162], atomic vapour cells [163] and cold neutral atoms in magneto-optical traps [131, 136], but not yet on cold ions in an ion trap.

Ion traps provide the opportunity to simultaneously trap different species. By laser cooling one type of ion, the other ions in the trap can be sympathetically cooled [164, 165]. A system to trap and cool one ion species can then be used without major modifications to trap and cool other types of atomic and molecular ions. Frequency combs offer a wide spectrum of frequencies through coherent broadening in nonlinear optical fibers [166] and doubling in nonlinear crystals or higher harmonic generation in gas jets [167, 168]. The combination of direct frequency comb spectroscopy and ion trapping thus provides the possibility to

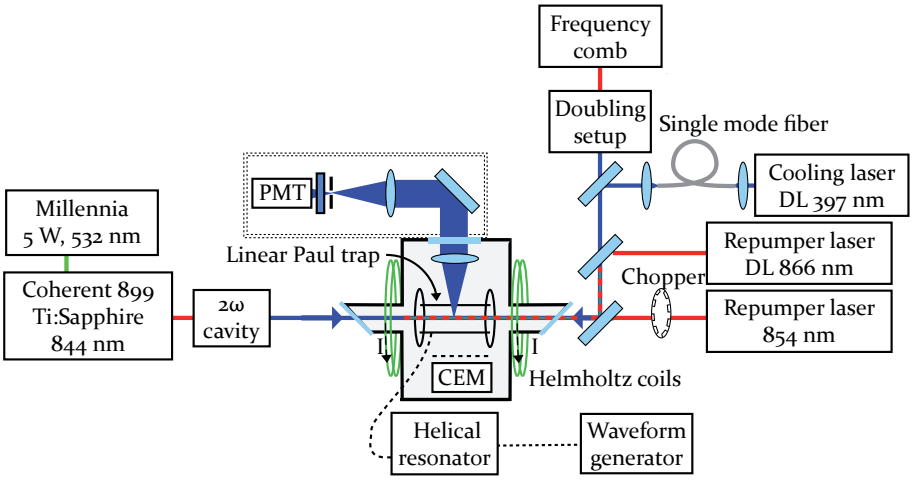

Figure 6.1: Schematic layout of the laser system and linear Paul trap. The indicated doubling setup is shown in detail in Fig. 6.2. DL=Diode laser, PMT=Photo-Multiplier Tube, 2ω=frequency-doubling setup, CEM=Channel Electron Multiplier.

perform spectroscopy on various ionic transitions in a single measurement system.

In this Chapter we demonstrate for the first time direct frequency comb spectroscopy of ions in a trap. It is shown that this technique can be applied using an upconverted frequency comb at 394 nm, without amplification of the comb pulses. Furthermore, we combine it with a shelving scheme [169] to suppress background signal from non-resonant comb modes, resulting in a good signal to noise ratio despite the low power per comb mode. Calcium ions are used for this experiment because a more accurate calibration of the $4s\,^2\mathrm{S}_{1/2} - 4p\,^2\mathrm{P}_{3/2}$ state is of interest for the search for a change of α over timespans of many billion years [149]. Apart from this application, trapping and laser cooling of the calcium ion has been widely studied [170–172], in particular for atomic clocks [26, 41] and quantum computation [152].

6.2 Experimental setup and procedures

6.2.1 Ion trapping

The spectroscopy is performed in a linear Paul trap. This trap consists of four linear electrodes at a distance $r_0 = 4$ mm to the trap axis. To two diagonally facing rods

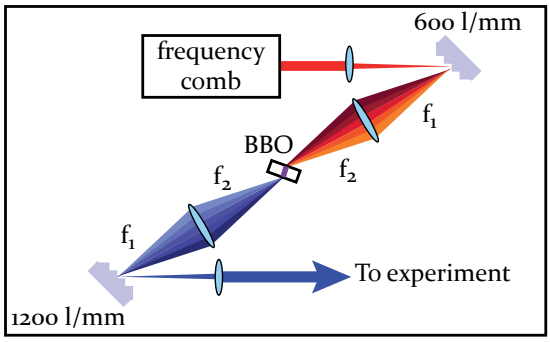

Figure 6.2: Setup for chirped doubling of the frequency comb. Lenses are drawn for clarity, in practice only reflective optics are used. The comb spectrum is dispersed on a 600 l/mm grating before being doubled in a BBO-crystal, in order to obtain a good conversion efficiency over a wide spectrum. The colors in the doubled spectrum are overlapped again using a 1200 l/mm grating. $f_1 = 20$ cm, $f_2 = 10$ cm.

an oscillating voltage $V_0 = 60$ V at a frequency $\Omega = 2\pi \times 3.3$ MHz is applied, corresponding to a stability parameter $q = 0.04$. The endcaps are formed by two ring electrodes at a voltage $V = 10$ V. Further details on the trap are described in Chapter 2. The ion trap is mounted in a vacuum chamber, evacuated to a pressure of 3×10^{-9} mbar. Calcium ions are produced by a two-step ionization process: Evaporated atoms from an oven are first excited at 422 nm to the $4p\,^1\mathrm{P}_1$ state by a frequency-doubled CW Ti:sapphire laser (Coherent 899), and subsequently ionized by part of the doubled frequency comb spectrum at $\lambda < 391$ nm (see Section 2.3.4). The comb is also used for the spectroscopy on the ions (see below). The total system is schematically depicted in Fig. 6.1.

6.2.2 Doppler cooling to ion cloud crystallization

In order to reduce the Doppler effect on the single-photon spectroscopy transition, laser cooling is applied on the $4s\,^2\mathrm{S}_{1/2} - 4p\,^2\mathrm{P}_{1/2}$ transition using a 397 nm diode laser (Toptica DL100). The relevant energy levels are shown in Fig. 6.4. The cooling laser is set at a red-detuning $\Delta f \approx 10$ MHz from resonance, referenced to a wavemeter (Atos model LM-007). The wavemeter is regularly calibrated by scanning the cooling laser over the transition, and the locking point is set relative to the resonance. During the measurements the cooling range is locked within the relative accuracy of the wavemeter of ± 3 MHz.

The spatial mode of the cooling laser is cleaned up in a single mode fiber to

reduce background from scattered light. The remaining 0.3 mW is focused to a beam diameter of $w_0 = 0.5$ mm in the trap. Since the excited ions have a 7% chance to decay to the long-lived $3d\,^2\mathrm{D}_{3/2}$ state, a repumper diode laser at 866 nm is used ($P = 1$ mW, Toptica DL100). The spectroscopy is performed on a crystallized ion cloud to reduce the Doppler broadening. The center of the trap is imaged onto a pinhole to remove background radiation and scattered light from the electrodes. Fluorescence from the $4s\,^2\mathrm{S}_{1/2} - 4p\,^2\mathrm{P}_{1/2}$ transition is then observed using a photomultipler tube (PMT, Philips XP2020Q). From the decay in fluorescence we determined a lifetime for the ions in the trap of $\tau \approx 8$ minutes, which is limited by the vacuum conditions. This lifetime can vary ~ 10 % from scan to scan due to a change in cooling parameters, in particular due to the free drifting repumper laser. The exact number of ions is difficult to determine with the current setup, but is estimated to be of the order of a few hundred ions per cloud based on the absence of discretization in the fluorescence signal (even for long measurement times) and the short loading time of < 1 s.

6.2.3 Absolute frequency calibration

The modes from a frequency comb can be described by the repetition frequency f_{rep} of the pulses and a carrier-envelope offset frequency f_{ceo}. The frequency of the n^{th} mode is equal to $f_n = \pm f_{ceo} + n \times f_{rep}$. Both f_{rep} and f_{ceo} are radio frequencies, which are locked to a frequency standard (in our case a Stanford PRS10 Rubidium atomic clock, referenced to the Global Positioning System). The frequency comb laser for this experiment is based on Ti:sapphire. Chirped mirrors are used in the laser for dispersion management, and are chosen such that the output is maximized at the desired wavelength of $\lambda = 788$ nm (see Chapter 3). This light is frequency doubled in a 3 mm BBO-crystal to obtain the right wavelength range to excite the $4s\,^2\mathrm{S}_{1/2} - 4p\,^2\mathrm{P}_{3/2}$ transition. By matching the angular dispersion induced by a grating to the wavelength derivative of the phase-matching angle [173], a wide bandwidth can be phase-matched. This method is used (Fig. 6.2) to obtain a frequency comb in the blue with a FWHM of 13 nm and a power of P ≈ 2 mW (Fig. 6.3).

The calcium ions are excited by focusing the upconverted comb light in the trap to an elliptical beam with a major axis ($1/e^2$ width) of 0.8 mm, and a minor axis of 0.4 mm. In order to scan over the transition, f_{rep} is varied. A small change in this parameter leads to a frequency scan of the comb near the resonance. Only one comb mode is resonant at the time because a single-photon transition is probed. All other $\approx 10^5$ modes do not contribute to the signal, but do give background signal due to scattered photons. This signal-to-noise issue is over-

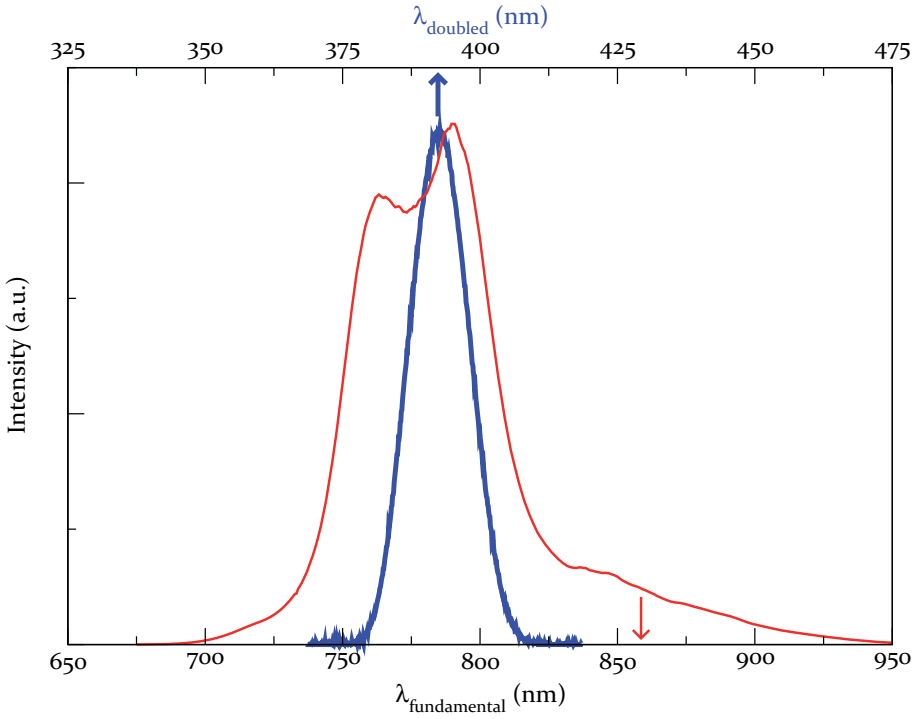

Figure 6.3: (The comb spectrum that is used for this spectrum: both the fundamental in the infrared (thin line, axis at the bottom) and the doubled blue spectrum (thick line, wavelength axis above the picture) are shown.

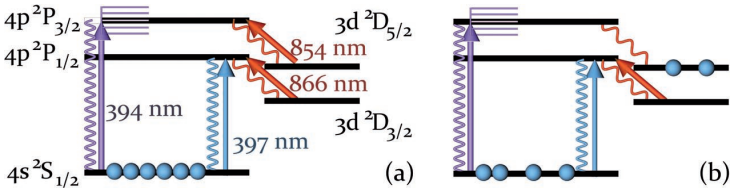

Figure 6.4: Schematic view of the energy levels and the shelving principle. Arrows indicate laser beams, the wavy lines spontaneous fluorescence. The second repumper at 854 nm is periodically blocked using a chopper. If this repumper is present (situation (a)) all ions stay in the cooling cycle. A blocked repumper leads to transfer of the ions into the dark state, and the fluorescence from the cooling laser decreases (situation (b)).

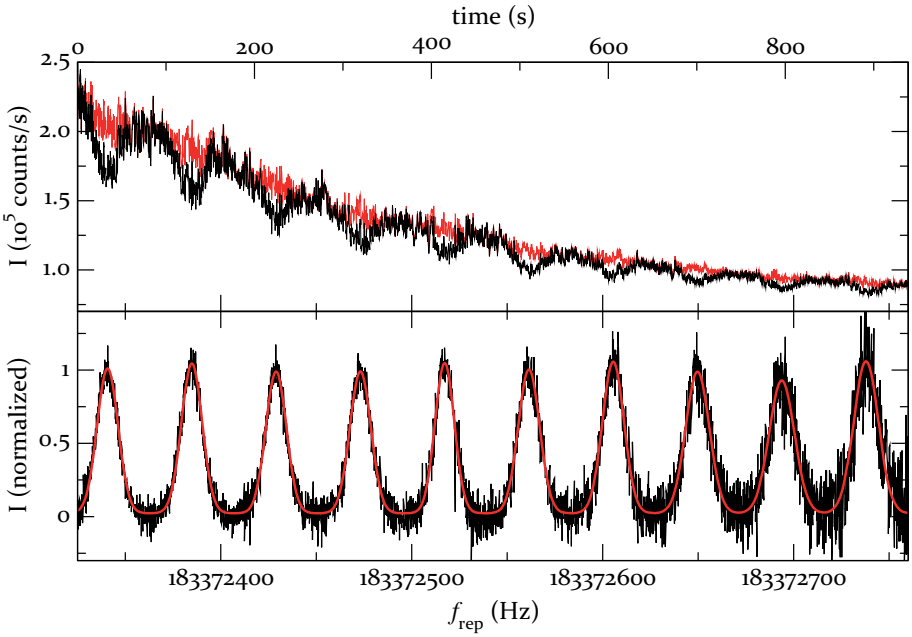

Figure 6.5: Top: Measured fluorescence signal for the periods where the second repumper at 854 nm is on (red trace) and the periods where the repumper is off (black trace). The comb repetition frequency f_{rep} is scanned against time (upper axis) and frequency (lower axis). Bottom: Normalized fluorescence signal (corrected for decay, thin black trace) and the corresponding fit (thick red trace).

come by employing a 'shelving' scheme (see e.g. [169]), depicted schematically in Fig. 6.4. Ions that are excited to the $4p\,^2\mathrm{P}_{3/2}$ state, have a 7% chance to decay to the $3d\,^2\mathrm{D}_{5/2}$ state which has a lifetime of 1.2 s [174]. Trapped in this state they can no longer contribute to the cooling cycle. Since the fluorescence from the cooling laser is monitored, less signal will be observed in this situation (Fig. 6.4(b)). However, if a second repumper laser is used on the $3d\,^2\mathrm{D}_{5/2}$-$4p\,^2\mathrm{P}_{3/2}$ transition at $\lambda = 854$ nm, ions will be pumped back into the ground state and participate in the cooling cycle (Fig. 6.4(a)).

The periods with and without the second repumper are alternated using a chopper at 100 Hz, and for each data point the fluorescence counts for both situations are recorded. The fluorescence signal detected at 397 nm will now be unaffected by the presence of the comb laser for the periods where the 854 nm repumper is present ('repumper on' in the upper part of Fig. 6.5). The situation is different for the periods where the second repumper is blocked. In this

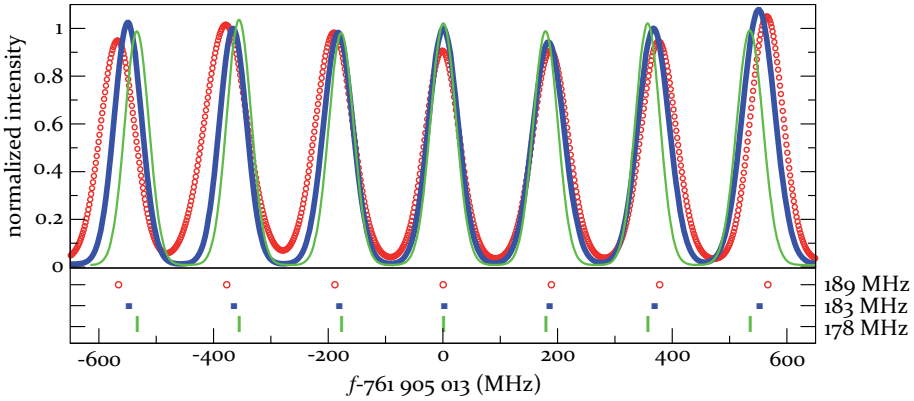

Figure 6.6: Mode number determination: The upper part of the graph shows the fits to the scans at different frequency comb repetition frequencies (f_{rep}), multiplied with a mode number n_0 to the approximate optical transition frequency (see text). Three different f_{rep} are shown (frequency uncertainty margins are smaller than the shown data points): 178 MHz (thin green trace), 183 MHz (blue thick trace) and 189 MHz (circles, red trace). The lower part shows the possible transition frequencies corresponding to the upper graph. The overlap of the traces at $f_{trans} = 761\,905\,012.7$ MHz can clearly be seen, and was checked for five different repetition frequencies (only 3 are shown for clarity).

case, every time a comb line comes into resonance with the $4s\,^2\mathrm{S}_{1/2} - 4p\,^2\mathrm{P}_{3/2}$ transition, ions are pumped into the dark $3d\,^2\mathrm{D}_{5/2}$ state, so the measured fluorescence will decrease proportional to the excitation rate. Due to the periodic nature of the frequency comb, this signal is repeated for every comb mode that comes into resonance with the probed transition ('repumper off' in the upper part of Fig. 6.5). The recorded signals for the situations with and without repumper are subtracted and corrected for the loss of calcium ions from the trap, resulting in a typical measurement curve as shown in the lower part of Fig. 6.5. In order to eliminate residual directionally dependent effects, all measurements are performed in both increasing and decreasing frequency direction. A comb of Gaussians is fitted to the corrected curves, where the width and height of each resonance is varied separately, but with fixed distances as given by the frequency comb spacing. The statistical uncertainty of such a fit is typically 1.8 MHz.

An important issue in frequency comb spectroscopy is the determination of the mode number n_0, usually based on previous measurements. The best known value for the $4s\,^2\mathrm{S}_{1/2} - 4p\,^2\mathrm{P}_{3/2}$ transition has long been $\nu = 25\,414.40(15)$ cm^{-1} [155], until a new value was reported of $\nu = 25\,414.4137$ cm^{-1} [153].

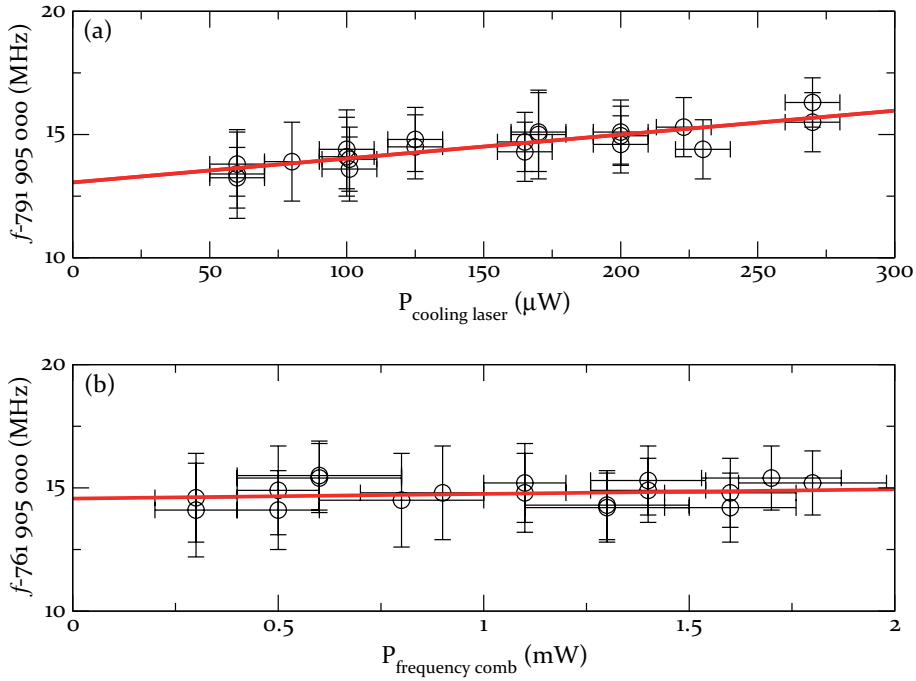

Figure 6.7: (a) Measured data for light shifts induced by the cooling laser at $P_{comb} = 1.9(0.2)$ mW (circles). (b) Measured data for light shifts induced by the frequency comb laser at $P_{cooling\ laser} = 200(10)\ \mu$W. The weighted fits to the data are also shown (lines).

Because no uncertainty was known for this measurement, it has been re-evaluated recently leading to a best value of $\nu = 25\,414.415(2)$ cm^{-1} [154]. The resulting 1σ accuracy of 60 MHz is insufficient to assign the mode number with confidence. We can, however, determine the mode by changing f_{rep}, which is graphically shown in Fig. 6.6. First an approximate mode number can be deduced from the earlier presented values. Using the selected mode number, one of the peak centers overlaps with the transition frequency, while the others deviate an integer times the repetition rate from this value. After f_{rep} is changed by several MHz, the procedure is repeated. The peak centers of scans with different f_{rep} will overlap at the peak with the correctly assigned mode number, but seperate on neighbouring peaks (Fig. 6.6).

6.2.4 Results and systematic effects

In order to absolutely determine the transition frequency of the $4s\,^2\mathrm{S}_{1/2}-4p\,^2\mathrm{P}_{3/2}$ transition, we have investigated several systematic effects on the transition frequency. The strongest is due to the always present 397 nm cooling laser on the $4s\,^2\mathrm{S}_{1/2} - 4p\,^2\mathrm{P}_{1/2}$ transition. Since its detuning is set at about half the natural linewidth, and the cooling laser couples to the same ground state as the transition that is measured, this laser can cause a significant AC Stark shift. Fluctuations in the cooling laser frequency may lead to a variation in this shift during measurements. However, this does not lead to a systematic effect due to the regular calibration of the detuning. For this average detuning an effective shift is measured, by varying the cooling laser intensity (Fig. 6.7 (a)). The measured frequency shift is $\Delta f_{trans} = 9.7(1.3)$ kHz/μW$\times P_{cooling}$, where $P_{cooling}$ is the cooling laser power in μW. The corresponding zero-crossing is $f_{trans} = 761\,905\,013.06(0.21)$ MHz. In addition, at $P_{cooling} = 200(10)\mu$W the measured dependence of the transition frequency on the frequency comb laser power is $\Delta f_{trans} = 0.19(0.24)$ MHz/mW$\times P_{comb}$, with P_{comb} the comb laser power in mW (Fig. 6.7 (b)). The transition frequency is corrected for the corresponding shift at $P_{comb} = 1.9$ mW of $\Delta f_{trans} = 0.36(0.46)$ MHz. The repumper lasers do not cause a significant light shift, since the 866 nm laser does not couple to either one of the levels involved in the measured transition, and the 854 nm repumper is not present during the shelving intervals. The recoil shift is calculated to be 32 kHz, which is small compared to the measurement accuracy.

Due to stray electric fields, ions can be pushed from the axis towards a higher electric field region. The spectroscopy laser enters the trap on axis, through a 3 mm diameter hole, limiting the maximum deviation from the center at which ions can be probed. We made a conservative estimation of the Stark shift by calculating the maximum Stark shift at the edge of this region, using the Einstein A coefficients as published in [175]. The calculated shift is only 0.2 kHz, and can thus be neglected for the current measurement. This value is small due to the large energy difference between the $4s$ and $4p$ and the s, p and d levels that are connected through the Stark interaction, in combination with the low trapping fields that were used.

Since the comb laser beam is linearly polarized, both magnetic substates of the ground state are equally exited. Hence, without optical pumping between the levels no first order Zeeman shift is expected. The relative population of the ground states is expected to be mainly influenced by the lasers involved in the cooling cycle, which are both linearly polarized, so no optical pumping is expected. To experimentally verify this assumption, the Zeeman coefficient was measured by applying external magnetic fields perpendicular and parallel to the propagation

directions of the laser beams. On the basis of a previous Zeeman shift determination [47] and magnetic field measurements outside the vacuum chamber, the magnitude of the magnetic field in these directions is estimated to be $40\ \mu$T and $20\ \mu$T respectively. These fields correspond to shifts in the transition frequency of $+0.04(0.08)$ MHz and $-0.04(0.08)$ MHz using the measured field dependence, and are thus negligible compared to the measurement accuracy. This leaves the statistical uncertainty due to the comb laser to consider. For a measurement time per data point of 0.1 s, the Allan deviation is 10^{-9}. Since a typical scan consists of about 3000 points measured over 10 minutes, this deviation averages down further to 10^{-11} and does not contribute significantly to the uncertainty budget. Once corrected for the measured shifts, the unperturbed transition frequency of the $4s\,^2\mathrm{S}_{1/2} - 4p\,^2\mathrm{P}_{3/2}$ transition in $^{40}\mathrm{Ca}^+$ is found to be $f = 761\,905\,012.7(0.5)$ MHz (1σ uncertainty). This result is consistent with the previous most accurate result of $f = 761\,904\,994(60)$ MHz [154]

6.3 Conclusion

In conclusion, direct frequency comb spectroscopy on ions in a linear Paul trap has been demonstrated for the first time, using an upconverted comb laser and shelving detection. The $4s\,^2\mathrm{S}_{1/2} - 4p\,^2\mathrm{P}_{3/2}$ transition in $^{40}\mathrm{Ca}^+$ has been calibrated to be at $f = 761\,905\,012.7(0.5)$ MHz. The obtained level of accuracy is more than two orders of magnitude better than previous calibrations. The applicability of this method extends well beyond the probed ion and transition used for this experiment, if direct frequency comb spectroscopy were used on sympathetically cooled ions in a Paul trap.

Chapter 7

Direct frequency-comb spectroscopy of a dipole-forbidden clock transition in trapped $^{40}Ca^{+}$ ions

7.1 Introduction

Optical frequency combs provide a direct link between optical and microwave frequencies [7, 8]. This link enables to carry the accuracy of a microwave frequency standard to the optical domain, or to transfer the extreme accuracy achieved in optical spectroscopy (currently reaching below the 10^{-17}-level [1]) to any other part of the optical spectrum and to the microwave domain. In addition, the development of broadband titanium-doped sapphire frequency-comb (FC) lasers with a wavelength span of hundreds of nanometers [130, 176] makes high accuracy frequency calibration possible over a very wide wavelength range. These FCs can be employed to calibrate an additional laser that is used for excitation, but it is also possible to directly use the light of the comb modes to perform the metrology [48, 132, 135, 162]. This technique of Direct Frequency-Comb Spectroscopy (DFCS), is advantageous in that the full comb spectrum is in principle available for excitation, without the need for an additional probe laser.

An ion trap containing laser-cooled ions provides an ideal system for DFCS as it allows for long interaction times. Furthermore, different ionic species can be trapped simultaneously, and be sympathetically cooled and detected by the laser-cooled ions [164, 165]. The application of DFCS to trapped ions [48] thus provides the possibility to perform spectroscopy on various ionic transitions in a single measurement setup. To our knowledge, the possibility of DFCS of trapped

ions has been demonstrated only for strong resonance lines. The range of applicability of this method would be greatly extended if also weak and narrow transitions could be detected. For example, such a narrow 'clock' transition could be used as an *in situ* frequency reference for the calibration of other transitions in ions, or as an accurate probe for external fields in the ion trap. Also the comparison of several different clock transitions in an ion trap, with a single excitation laser would be possible. In this Letter we show that DFCS can be performed on significantly weaker transitions, using an ion trap and even without amplification of the FC laser. This is demonstrated on a laser-cooled crystal of calcium ions, in which the dipole-forbidden $4s\,^2\mathrm{S}_{1/2} - 3d\,^2\mathrm{D}_{5/2}$ transition at 729 nm (natural linewidth 0.14 Hz) is induced with DFCS. On this transition one can potentially reach Hz-level accuracy, as was shown previously by Chwalla *et al.* using CW laser excitation [27].

7.2 Experimental setup and procedures

7.2.1 Ion trapping and laser cooling

In our experiment, calcium ions are produced by two-photon excitation involving a frequency-doubled portion of the FC [48]. The created ions are trapped in a segmented linear Paul trap (Fig. 7.1), which consists of four cylindrical molybdenum electrodes with a radial spacing of $2 \times r_0 = 7$ mm. Two of these rods are segmented into 5 pieces of 12 mm length each, to which different direct-current (DC) voltages can be applied. These potentials serve to confine the ions to the trap axis and compensate for possible stray electric fields. The endcaps of the trap are formed by the electrodes adjacent to the central region, hence the spacing between the endcaps is $z = 12$ mm. A voltage of $V_{ec} = 10$ V is applied to these electrodes to provide axial confinement.

The other two electrodes are unsegmented cylindrical rods of 60 mm length. To these electrodes a radio-frequency (RF) signal is applied, to provide radial ponderomotive confinement of the ions. This RF voltage oscillates at frequency $\Omega = 2\pi \times 2.6$ MHz with amplitude $\mathrm{V}_{RF} = 150$ V, leading to a Mathieu stability parameter $q_r = 0.2$ and a radial secular trapping frequency of $2\pi \times 202$ kHz. The pressure inside the vacuum chamber is 10^{-11} mbar, for which the lifetime for a string of confined ions is larger than 8 hours. Further information on the ion trap can be found in Chapter 2.

The trapped $^{40}\mathrm{Ca}^+$ ions are Doppler cooled on the $4s\,^2\mathrm{S}_{1/2} - 4p\,^2\mathrm{P}_{1/2}$ transition, using a grating-stabilized diode laser at 397 nm ($P = 0.1$ mW after spatial filtering, Toptica DL100) in combination with a repumper diode laser at 866 nm

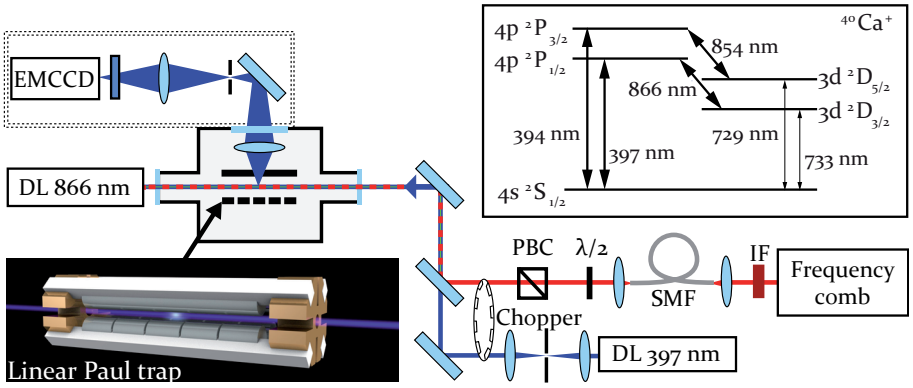

Figure 7.1: Schematic of the setup: $^{40}Ca^{+}$ is trapped in a linear Paul trap, and Doppler-cooled using two diode lasers (DL). Fluorescence at 397 nm due to the cooling laser is spatially filtered and detected by an EMCCD camera. A simplified energy level scheme for $^{40}Ca^{+}$ is shown in the inset. IF=interference filter, $\lambda/2$=half-wave plate, PBC=polarizing beamsplitter cube, SMF=single mode fiber.

($P = 0.8$ mW, Toptica DL100) [47]. Fluorescence photons emitted by the ions are imaged onto an Electron Multiplying CCD camera (EMCCD, Andor iXon^{Em} +), with a telescope comprising one lens inside the vacuum with an effective focal length EFL $= 25$ mm, and a second lens outside the vacuum with a focal length of $f = 100$ mm. In order to reduce stray light, the beam is spatially filtered at the intermediate focus in between the two lenses.

7.2.2 Frequency calibration

The $4s\,^2S_{1/2} - 3d\,^2D_{5/2}$ transition is excited with light near $\lambda = 729.5$ nm from an unamplified FC, which is described in chapter 3. The spectrum that is used for excitation is shown in Fig. 7.2. Both the carrier-envelope offset frequency (f_{ceo}) and the repetition frequency (f_{rep}) of the FC are locked to a Stanford PRS10 Rubidium atomic clock, that is referenced to the Global Positioning System. The FC has a power of P $= 0.12(2)\ \mu$W per mode at the transition frequency, focused to a spot size of $w_0 = 0.17$ mm. A 60 nm bandwidth interference filter with 99% transmission at 729.5 nm and an optical density of 7 in the wavelength range of $760 - 870$ nm is used in this beam to suppress excitation of the dipole allowed $3d\,^2D_{5/2} - 4p\,^2P_{3/2}$ and $3d\,^2D_{3/2} - 4p\,^2P_{3/2}$ transitions. To avoid an AC-Stark shift by the 397 nm laser, the cooling and comb laser are alternately chopped mechanically at a frequency of 59 Hz.

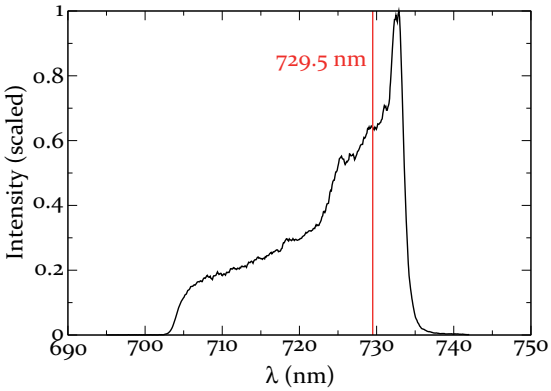

Figure 7.2: The comb spectrum as used for the direct excitation of the clock transition in calcium. The spectrum is cut by a combination of a dichroic beamsplitter and an interference filter.

The fluorescence of the ions due to the cooling laser is monitored with the EMCCD camera, at a speed of 1 Hz. Excitation of the clock transition is detected by observing the disappearance of fluorescence from the cooling laser throughout the lifetime of the $D_{5/2}$-level (similar to the method we used for the direct frequency comb spectroscopy described in Chapter 6). This shelving method yields near 100% detection probability, enabling to detect the transition despite a very low excitation rate of ~ 7 per 1000 seconds per ion, over a background count rate of ~ 0.9 per 1000 seconds per ion.

Typical images as recorded in this process are shown in Fig. 7.3.a and 7.3.b. Integration of the signal over several image rows results in the traces shown below the images, where the distinction between dark and bright ions is made based on a threshold at 50% of the peak fluorescence intensity. The count rate is limited to 20 counts/100 s for a string of 10 ions, to avoid ion heating and count ambiguity. An example of the detection of dark ions on resonance in 100 s is shown in Fig. 7.3.c. To record the transition, the FC is scanned over the transition in steps of frequency $\Delta f = 1.2$ MHz every 100 seconds, resulting in a total time of 30 minutes per scan. A single trace as recorded in this way is shown in Fig. 7.4. The corresponding total measurement signal is shown in Fig. 7.5 (the error bars indicate a $\sqrt{N}$ count uncertainty, and are based on the underlying Poissonian statistics of the ion excitation process[177]).

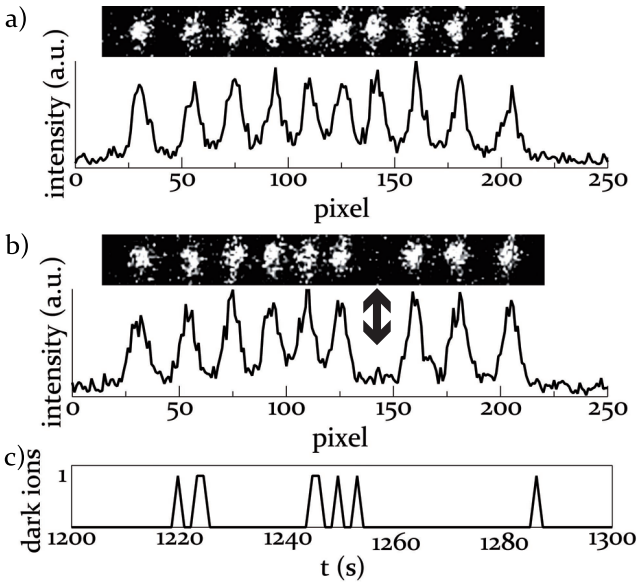

Figure 7.3: Detection method: Parts **a)** (all bright ions) and **b)** (one dark ion at arrow) show the camera image of a string of ions. The distance between the ions is $\sim 20\,\mu$m. Integration over ~ 15 lines of the camera images results in the traces as shown underneath the images. The detection of dark ions close to resonance in 100 seconds is shown in figure **c)**.

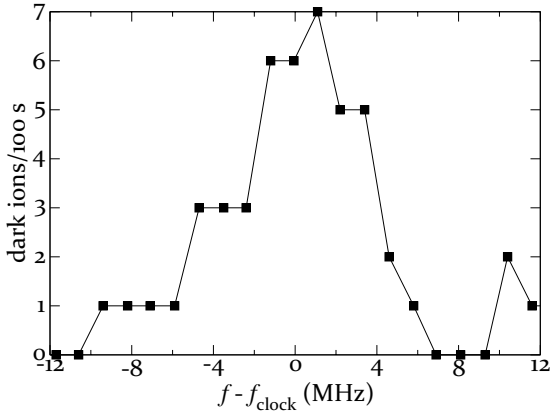

Figure 7.4: Example of a single scan over the transition. Even though the count rates are very low, the transition can still be identified. The frequencies are relative to the clock transition $f_{clock} = 411\,042\,129.776\,\text{MHz}$ [26, 27].

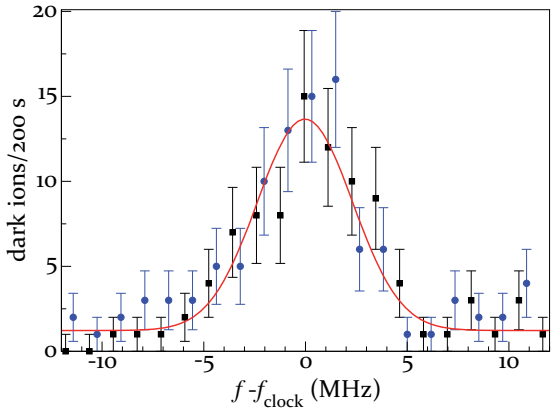

Figure 7.5: Graph of the resonance line, relative to the literature value of $f_{clock} = 411\,042\,129.776$ MHz [26, 27], consisting of two measurement sets (one indicated by circles, the other by squares). For each set the data is collected by scanning the FC over the resonance from both sides. The solid line shows a Gaussian fit through all the data points.

7.2.3 Results and systematic effects

There are several contributions to the current frequency uncertainty budget, which all have the prospect to be reduced to the Hz-level. The largest of these is caused by a residual time overlap between the cooling laser and the FC excitation period. Due to the change in intensity during the switching, this overlap leads to a time-dependent AC-Stark shift. The average result of this effect is a deformation of the lineshape. The effect has been simulated (Fig. 7.6), yielding an effective AC-Stark shift of $\Delta f = 0.15(0.10)$ MHz. The repumper causes a small shift of $\Delta f = -0.01(0.01)$ MHz. These two effects are relatively easy to reduce by total blocking of the cooling laser and repumper during the excitation with the frequency comb. Other systematic effects we investigated (AC-Stark effect due to the FC, the Zeeman effect in combination with possible optical pumping by the cooling laser, the AC- and DC-Stark effect due to the trap electric field and comb accuracy) give a total contribution < 8 kHz. An overview of the considered systematic effect is given in table 7.1. Correcting for all systematic shifts, we find a transition frequency $411\,042\,129.6(0.3)$ MHz, consistent with the value reported in [27].

Table 7.1: Measured systematic shifts and uncertainty budget (1σ).

Effect	$\Delta\nu$ (MHz)	1σ Uncertainty (MHz)
AC Stark:		
-frequency comb	0.00	0.00
-repumper	-0.01	0.01
-cooling laser	0.15	0.10
Zeeman and optical pumping	0.00	0.00
RF Stark effect	0.00	0.00
Comb calibration	0.00	0.00
Statistics	0.00	0.29
Total	0.14	0.30

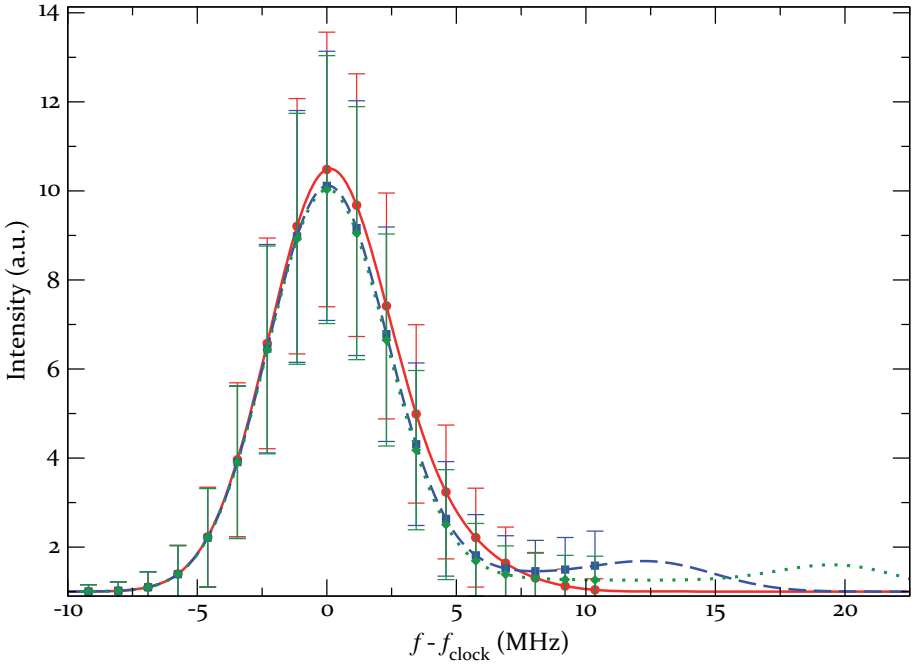

Figure 7.6: Simulation of the effect of a residual overlap between the spectroscopy and cooling laser: Due to the time overlap of the two, part of the time there will be a shift of the central frequency of the line profile. The lines indicate the resulting line profile, the dots the points as they would be recorded in our measurements. The different sets indicate different laser intensities, corresponding to AC Stark shifts (as would be recorded without the chopper) of: $\Delta f = 5$ MHz for the circles (solid line), $\Delta f = 13$ MHz for the squares (dashed line) and $\Delta f = 20$ MHz for the diamonds (dotted line).

7.3 Improvements towards building an ion clock

With some improvements to the current experiment, the $4s\,^2\mathrm{S}_{1/2} - 3d\,^2\mathrm{D}_{5/2}$ transition in either $^{40}\mathrm{Ca}^+$ or $^{43}\mathrm{Ca}^+$ could be used to built an ion clock. In the current experiment, an FC with a $\approx 2\,\mathrm{MHz}$ FWHM mode linewidth was used. The measured linewidth of $5.5\,\mathrm{MHz}$ FWHM is mainly limited by Doppler broadening, and corresponds to $T = 14\,\mathrm{mK}$. To improve on the presented results, both of these linewidths should be reduced. Doppler broadening may be removed by increasing the confinement of the ions by the trap such that the Lamb-Dicke regime is attained [41]. In this regime, the amplitude of the ion motion is smaller than the wavelength used for excitation, resulting in the cancellation of the first order Doppler effect. Due to this cancellation, the linewidth of the line to be measured is drastically reduced, allowing for higher precision measurements.

The criterion for trapping in the Lamb-Dicke regime is [41]:

$$k\lambda_{trap}\sqrt{2 < n > +1} \leq 1 \tag{7.1}$$

In this equation k is the laser wavenumber, $< n >$ the mean vibrational quantum number, and $\lambda_{trap} = \sqrt{\hbar/(2m\omega_{trap})}$. The energy of the vibrational quantum levels is $E_n = \hbar\omega_{trap}(n + \frac{1}{2})$. For a thermal distribution over these levels, the mean vibrational quantum number is given by $< n >= \frac{k_b T}{\hbar\omega_{trap}} - \frac{1}{2}$. Combining these equations, the Lamb-Dicke criterion translates into the following criterion for the trapping parameters:

$$\omega_{trap} \geq k\sqrt{\frac{k_b T}{m}} \quad \text{or} \quad T \leq \frac{\omega_{trap}^2 m}{k^2 k_b} \tag{7.2}$$

In a linear trap as used in the current experiment, this is most easily achieved in the radial direction. For the current trap conditions it would require implementation of 3D laser cooling to $T < 20.5\,\mathrm{mK}$ (which is well above the Doppler limit of $T_{Doppler} = 0.5\,\mathrm{mK}$), and excitation perpendicular to the trap axis.

In addition to the narrowing of the atomic linewidth described above, the width of the frequency comb modes also needs to be reduced in order to achieve a high accuracy and stability, as the current RF repetition rate locking results in frequency comb modes with a large bandwidth. This may be achieved by locking the comb to a high-finesse cavity [130]. Besides the increase in precision, a reduction of the comb linewidth in combination with a narrower atomic linewidth will enhance the excitation probability by orders of magnitude. On the assumption of an instrument linewidth of 23 Hz, as in [27], combined with such an FC, a 10^5 fold improved excitation rate can be obtained. Lowering the FC intensity by a factor of 10^2 then reduces the AC-Stark shift to $< 1.5\,\mathrm{Hz}$, with still a 10^3 times

increased excitation rate compared to the present experiment. The higher excitation rate requires a repumper on the $3d\,^2\mathrm{D}_{5/2} - 3p\,^2\mathrm{P}_{3/2}$-transition, for which light is available in the FC. With the aforementioned linewidths, in combination with a Poisson-limited noise, and a count rate of 5 counts/s, theoretically a stability of $\sigma(\tau) = 10^{-13}/\sqrt{\tau}$ could be reached. Under these conditions, DFCS as demonstrated here could provide a relatively simple method to operate a FC as an optical frequency standard with both stability and accuracy surpassing that of GPS-disciplined Rb standards by orders of magnitude.

The theory on further experimental requirements are described in [41] and shown to be experimentally achievable by [27].

7.4 Conclusions and outlook

In conclusion, we have demonstrated the feasibility of direct frequency comb spectroscopy of a dipole forbidden (clock-) transition in an ion trap. The measured transition frequency is consistent with previous measurements. The combination of long ion storage times with single-ion fluorescence imaging and detection by electron shelving yields a very high sensitivity. It enables DFCS even on narrow dipole-forbidden transitions, which are Doppler-broadened to several MHz.

We also point out that with the use of a FC with narrow linewidth and ion confinement in the Lamb-Dicke regime, DFCS as demonstrated here has the potential to reach a Hz-level accuracy. Work is ongoing to narrow down the frequency comb modes. This can be achieved by locking the comb modes via a transfer laser to a highly stable optical cavity. In addition, a tighter ion trap is needed in order to confine the ions in the Lamb-Dicke regime. The combination of these improvements will increase the excitation rate of the $4s\,^2\mathrm{S}_{1/2} - 3d\,^2\mathrm{D}_{5/2}$-transition by orders of magnitude, allowing to lock the frequency comb to the atomic transition. The presence of such a clock allows for more accurate measurements of atomic transition frequencies, relative to the clock transition in calcium ions. An option particularly worth mentioning would be to directly compare atomic transitions in a single ion trap.

In future work, the developed techniques of spectroscopy on laser-cooled and trapped ions can be applied to perform spectroscopy on other ions that are sympathetically cooled by calcium. For example, Ti^+ and Mn^+ could be trapped simultaneously with Ca^+. These ions are interesting to investigate at a MHz-level accuracy, in order to provide accurate laboratory wavelengths for use in the Many-Multiplet method. The technique of multiheterodyne spectroscopy (described in section 4.3.3) may be applied to unravel the complicated hyperfine structure of

Mn^+. Using this technique, also molecular ions could be trapped, cooled and studied.

Another direction of research could be spectroscopy of He^+ from the ground state, in order to provide a stringent test of the theory of quantum electrodynamics. The 1s-2s transition in these ions could be studied using two-photon excitation at a wavelength of 60.8 nm [178]. Light at this wavelength can be generated by focusing an amplified comb in a gas jet, generating high harmonics of the frequency comb at the desired frequency [134]. A similar approach may be used to search for the nuclear transition at 7.6 ± 0.5 eV in ^{229}Th [179]. Due to its narrow natural linewidth (estimated to be in the order of one mHz) and reduced sensitivity to the environment, this transition may be interesting for future clock applications. Despite being a nuclear transition, the expected transition wavelength of $\sim 160 \pm 10$ nm is still accessible using upconverted frequency combs. To pinpoint this transition, a frequency comb can be used to scan over a large range of frequencies simultaneously.

Bibliography

[1] C. W. Chou, D. B. Hume, J. C. J. Koelemeij, D. J. Wineland, and T. Rosenband, "Frequency comparison of two high-accuracy Al^+ optical clocks," Physical Review Letters **104**, 070802 (2010).

[2] W. Paul, "Electromagnetic traps for charged and neutral particles," Reviews of Modern Physics **62**, 531–540 (1990).

[3] T. Hänsch and A. Schawlow, "Cooling of gases by laser radiation," Optics Communications **13**, 68–69 (1975).

[4] D. Wineland and H. Dehmelt, "Proposed 1014 delta upsilon less than upsilon laser fluorescence spectroscopy on T1+ mono-ion oscillator iii," Bulletin of the American Physical Society **20**, 637 (1975).

[5] D. J. Wineland, R. E. Drullinger, and F. L. Walls, "Radiation-pressure cooling of bound resonant absorbers," Physical Review Letters **40**, 1639–1642 (1978).

[6] D. Jones, S. Diddams, J. Ranka, A. Stentz, R. Windeler, J. Hall, and S. Cundiff, "Carrier-envelope phase control of femtosecond mode-locked lasers and direct optical frequency synthesis," Science **288**, 635–639 (2000).

[7] S. Diddams, D. Jones, J. Ye, S. Cundiff, J. Hall, J. Ranka, R. Windeler, R. Holzwarth, T. Udem, and T. Hansch, "Direct link between microwave and optical frequencies with a 300 THz femtosecond laser comb," Physical Review Letters **84**, 5102–5105 (2000).

[8] R. Holzwarth, T. Udem, T. Hansch, J. Knight, W. Wadsworth, and P. Russell, "Optical frequency synthesizer for precision spectroscopy," Physical Review Letters **85**, 2264–2267 (2000).

[9] H. Schnatz, B. Lipphardt, J. Helmcke, F. Riehle, and G. Zinner, "First phase-coherent frequency measurement of visible radiation," Physical Review Letters **76**, 18–21 (1996).

[10] T. Udem, A. Huber, B. Gross, J. Reichert, M. Prevedelli, M. Weitz, and T. W. Hänsch, "Phase-coherent measurement of the hydrogen $1s - 2s$

transition frequency with an optical frequency interval divider chain," Physical Review Letters **79**, 2646–2649 (1997).

[11] M. Niering, R. Holzwarth, J. Reichert, P. Pokasov, T. Udem, M. Weitz, T. W. Hänsch, P. Lemonde, G. Santarelli, M. Abgrall, P. Laurent, C. Salomon, and A. Clairon, "Measurement of the hydrogen $1s$- $2s$ transition frequency by phase coherent comparison with a microwave cesium fountain clock," Physical Review Letters **84**, 5496–5499 (2000).

[12] S. Karshenboim and V. Ivanov, "Hyperfine structure in hydrogen and helium ion," Physics Letters B **524**, 259 – 264 (2002).

[13] N. Fortson, "Possibility of measuring parity nonconservation with a single trapped atomic ion," Physical Review Letters **70**, 2383–2386 (1993).

[14] T. Rosenband, D. B. Hume, P. O. Schmidt, C. W. Chou, A. Brusch, L. Lorini, W. H. Oskay, R. E. Drullinger, T. M. Fortier, J. E. Stalnaker, S. A. Diddams, W. C. Swann, N. R. Newbury, W. M. Itano, D. J. Wineland, and J. C. Bergquist, "Frequency ratio of Al^+ and Hg^+ single-ion optical clocks; Metrology at the 17th decimal place," Science **319**, 1808–1812 (2008).

[15] N. Kolachevsky, A. Matveev, J. Alnis, C. Parthey, T. Steinmetz, T. Wilken, R. Holzwarth, T. Udem, and T. Hänsch, "Testing the stability of the fine structure constant in the laboratory," Space Science Reviews **148**, 267–288 (2009).

[16] J. Benhelm, G. Kirchmair, R. Gerritsma, F. Zaehringer, T. Monz, P. Schindler, M. Chwalla, W. Haensel, M. Hennrich, C. F. Roos, and R. Blatt, "Ca^+ quantum bits for quantum information processing," Physica Scripta **T137** (2009).

[17] D. J. Wineland, "Quantum information processing and quantum control with trapped atomic ions," Physica Scripta **T137**, 014007 (2009).

[18] G. Campbell, A. Ludlow, S. Blatt, J. Thomsen, M. Martin, M. G. de Miranda, T. Zelevinsky, M. Boyd, J. Ye, S. Diddams, T. Heavner, T. Parker, and S. Jefferts, "The absolute frequency of the ^{87}Sr optical clock transition," Metrologia **45**, 539–548 (2008).

[19] T. Rosenband, W. Itano, P. O. Schmidt, D. B. Hume, J. Koelemeij, J. Bergquist, and D. Wineland, "Blackbody radiation shift of the $^{27}Al^+$ $^1S_0 - {}^3P_0$ transitions," Proceedings of the EFTF Conference pp. 289–292 (2006).

[20] S. Diddams, T. Udem, J. Bergquist, E. Curtis, R. Drullinger, L. Hollberg, W. Itano, W. Lee, C. Oates, K. Vogel, and D. Wineland, "An optical clock based on a single trapped Hg-199(+) ion," Science **293**, 825–828 (2001).

[21] J. Stenger, C. Tamm, N. Haverkamp, S. Weyers, and H. Telle, "Absolute frequency measurement of the 435.5-nm $^{171}Yb^{+}$-clock transition with a Kerr-lens mode-locked femtosecond lasers," Optics Letters **26**, 1589–1591 (2001).

[22] C. Tamm, B. Lipphardt, H. Schnatz, R. Wynands, S. Weyers, T. Schneider, and E. Peik, "$^{171}Yb^{+}$ single-ion optical frequency standard at 688 THz," IEEE Transaction on Instrumentation and Measurement **56**, 601–604 (2007).

[23] Y. H. Wang, T. Liu, R. Dumke, A. Stejskal, Y. N. Zhao, J. Zhang, Z. H. Lu, L. J. Wang, T. Becker, and H. Walther, "Improved absolute frequency measurement of the $^{115}In^{+}$ $5s^2\,{}^1S_0 - 5s5p\,{}^3P_0$ narrowline transition: Progress towards an optical frequency standard," Laser Physics **17**, 1017–1024 (2007).

[24] H. S. Margolis, G. P. Barwood, G. Huang, H. A. Klein, S. N. Lea, K. Szymaniec, and P. Gill, "Hertz-level measurement of the optical clock frequency in a single $^{88}Sr^{+}$ ions," Science **306**, 1355–1358 (2004).

[25] A. D. Ludlow, T. Zelevinsky, G. K. Campbell, S. Blatt, M. M. Boyd, M. H. G. de Miranda, M. J. Martin, J. W. Thomsen, S. M. Foreman, J. Ye, T. M. Fortier, J. E. Stalnaker, S. A. Diddams, Y. Le Coq, Z. W. Barber, N. Poli, N. D. Lemke, K. M. Beck, and C. W. Oates, "Sr lattice clock at 1×10^{-16} fractional uncertainty by remote optical evaluation with a Ca clock," Science **319**, 1805–1808 (2008).

[26] K. Matsubara, K. Hayasaka, Y. Li, H. Ito, S. Nagano, M. Kajita, and M. Hosokawa, "Frequency measurement of the optical clock transition of $^{40}Ca^{+}$ ions with an uncertainty of 10^{-14} level," Applied Physics Express **1**, 067011 (2008).

[27] M. Chwalla, J. Benhelm, K. Kim, G. Kirchmair, T. Monz, M. Riebe, P. Schindler, A. S. Villar, W. Hänsel, C. F. Roos, R. Blatt, M. Abgrall, G. Santarelli, G. D. Rovera, and P. Laurent, "Absolute frequency measurement of the $^{40}Ca^{+}$ $4s\,{}^2S_{1/2}$-$3d\,{}^2D_{5/2}$ clock transitions," Physical Review Letters **102**, 023002 (2009).

[28] H. B. Sandvik, J. D. Barrow, and J. a. Magueijo, "A simple cosmology with

a varying fine structure constant," Phys. Rev. Lett. **88**, 031302 (2002).

[29] J. Uzan, "The fundamental constants and their variation: observational and theoretical status," Reviews of Modern Physics **75**, 403–455 (2003).

[30] V. A. Dzuba, V. V. Flambaum, and J. K. Webb, "Space-time variation of physical constants and relativistic corrections in atoms," Physical Review Letters **82**, 888–891 (1999).

[31] J. Webb, V. Flambaum, C. Churchill, M. Drinkwater, and J. Barrow, "Search for time variation of the fine structure constant," Physical Review Letters **82**, 884–887 (1999).

[32] J. Berengut and V. Flambaum, "Laboratory spectroscopy and the search for variation of the fine-structure constant," Hyperfine interactions **196**, 269–278 (2010).

[33] M. T. Murphy, J. K. Webb, and V. V. Flambaum, "Revision of VLT/UVES constraints on a varying fine-structure constant," Monthly Notices of the Royal Astronomical Society **384**, 1053–1062 (2008).

[34] M. Murphy, V. Flambaum, J. Webb, V. Dzuba, J. Prochaska, and A. Wolfe, "Constraining variations in the fine-structure constant, quark massesand the strong interaction," Lecture Notes in Physics **648**, 131–150 (2004).

[35] H. Haffner, C. Roos, and R. Blatt, "Quantum computation with trapped ions," ArXiv: physics.quant-ph p. 0809.4368 (2008).

[36] J. Preskill, "The theory of quantum information and quantum computation lecture notes,"
http://www.theory.caltech.edu/people/preskill/ph229/ (1998).

[37] J. I. Cirac and P. Zoller, "Quantum computations with cold trapped ions," Physical Review Letters **74**, 4091–4094 (1995).

[38] C. Monroe, D. M. Meekhof, B. E. King, W. M. Itano, and D. J. Wineland, "Demonstration of a fundamental quantum logic gate," Physical Review Letters **75**, 4714–4717 (1995).

[39] D. Hayes, D. N. Matsukevich, P. Maunz, D. Hucul, Q. Quraishi, S. Olmschenk, W. Campbell, J. Mizrahi, C. Senko, and C. Monroe, "Entanglement of atomic qubits using an optical frequency comb," Physical Review Letters **104**, 140501 (2010).

[40] A. Steane, "The ion trap quantum information processor," Applied Physics

B: Lasers and Optics **64**, 623–642 (1997).

[41] C. Champenois, M. Houssin, C. Lisowski, A. Knoop, G. Hagel, A. Vedel, and F. Vedel, "Evaluation of the ultimate performances of a Ca^+ single-ion frequency standard," Physics Letters A **331**, 298–311 (2004).

[42] B. Guo, H. Guan, Q. Liu, Y. Huang, W.-c. Qu, X.-r. Huang, and K.-l. Gao, "Preliminary frequency measurement of the electric quadrupole transition in a single laser-cooled $^{40}Ca^+$ ion," Frontiers of Physics in China **4**, 144–154 (2009).

[43] S. Gulde, M. Riebe, G. Lancaster, C. Becher, J. Eschner, H. Haffner, F. Schmidt-Kaler, I. Chuang, and R. Blatt, "Implementation of the Deutsch-Jozsa algorithm on an ion-trap quantum computer," Nature **421**, 48–50 (2003).

[44] H. Haffner, F. Schmidt-Kaer, W. Hansel, C. Roos, T. Korber, M. Chwalla, M. Riebe, J. Benhelm, U. Rapoli, C. Becher, and R. Blatt, "Robust entanglement," Applied Physics B: Lasers and Optics **81**, 151–153 (2005).

[45] H. Haffner, W. Hansell, C. Roos, J. Benhelm, M. Chek-al kar, M. Chwalla, T. Korber, U. Rapol, M. Riebe, P. O. Schmidt, C. Becher, O. Guhne, W. Dur, and R. Blatt, "Scalable multiparticle entanglement of trapped ions," Nature **438**, 643–646 (2005).

[46] A. H. Myerson, D. J. Szwer, S. C. Webster, D. T. C. Allcock, M. J. Curtis, G. Imreh, J. A. Sherman, D. N. Stacey, A. M. Steane, and D. M. Lucas, "High-fidelity readout of trapped-ion qubits," Physical Review Letters **100**, 200502 (2008).

[47] A. L. Wolf, S. A. van den Berg, C. Gohle, E. J. Salumbides, W. Ubachs, and K. S. E. Eikema, "Frequency metrology on the $4s\,^2\mathrm{S}_{1/2} - 4p\,^2\mathrm{P}_{1/2}$ transition in $^{40}Ca^+$ for a comparison with quasar data," Physical Review A **78**, 032511 (2008).

[48] A. Wolf, S. van den Berg, W. Ubachs, and K. Eikema, "Direct frequency comb spectroscopy of trapped ions," Physical Review Letters **102**, 223901 (2009).

[49] R. Yamazaki, H. Sawamura, K. Toyoda, and S. Urabe, "Stimulated Raman spectroscopy and the determination of the D -fine-structure level separation in $^{40}Ca^+$," Physical Review A **77**, 012508 (2008).

[50] E. Fischer, "Die dreidimensionale stabilisierung von ladungstragern in

einem vierpolfeld," Zeitschrift für Physik **156**, 1–26 (1959).

[51] W. Paul, H. Reinhard, and U. Von Zahn, "Das elektrische massenfilter als massenspektrometer und isopentrenner," Zeitschrift für Physik **152**, 143–182 (1958).

[52] J. Prestage, G. Dick, and L. Maleki, "New ion trap for frequency standard applications," Journal of Applied Physics **66**, 1013–1017 (1989).

[53] D. Denison, "Operating Parameters of a quadrupole in a grounded cylindrical housing," Journal of Vacuum Science & Technology **8**, 266–& (1971).

[54] P. Ghosh, *Ion traps* (Oxford science publications, 1995).

[55] D. Berkeland, J. Miller, J. Bergquist, W. Itano, and D. Wineland, "Minimization of ion micromotion in a Paul trap," Journal of Applied Physics **83**, 5025–5033 (1998).

[56] W. Itano, B. J. C., and D. J. Wineland, "Laser spectroscopy of trapped atomic ions," Science **237**, 612–617 (1987).

[57] H. Metcalf and P. van der Straten, *Laser cooling and trapping* (Springer-Verlag New York, 1999).

[58] G. V. Major, F.G. and G. Werth, *Charged particle traps* (Springer Berlin Heidelberg, 2005).

[59] C. Roos, *Controlling the quantum state of trapped ions* (PhD Thesis, 2000).

[60] W. Itano and D. J. Wineland, "Laser cooling of ions stored in harmonic and Penning traps," Physical Review A **25**, 35–54 (1982).

[61] C. Foot, *Atomic physics* (Oxford university press, 2005).

[62] M. Marciante, C. Champenois, A. Calisti, J. Pedregosa-Gutierrez, and M. Knoop, "Ion dynamics in a linear radio-frequency trap with a single cooling laser," Physical Review A **82**, 033406 (2010).

[63] R. Hilborn, "Einstein coefficients, cross-sections, f values, dipole-moments, and all that," American Journal of Physics **50**, 982–986 (1982). Updated version from 2002 on the Arxiv: arXiv:physics/0202029.

[64] R. Drullinger, D. Wineland, and J. Bergquist, "High-resolution optical-spectra of laser cooled ions," Applied Physics A: Materials Science & Processing **22**, 365–368 (1980).

[65] D. J. Wineland, J. C. Bergquist, W. M. Itano, J. J. Bollinger, and C. H. Manney, "Atomic-ion coulomb clusters in an ion trap," Physical Review Letters **59**, 2935–2938 (1987).

[66] T. Baba and I. Waki, "Sympathetic cooling rate of gas-phase ions in a radio-frequency-quadrupole ion trap," Applied Physics B: Lasers and Optics **74**, 375–382 (2002).

[67] K. Okada, M. Wada, T. Takayanagi, S. Ohtani, and H. A. Schuessler, "Characterization of ion Coulomb crystals in a linear Paul trap," Physical Review A **81** (2010).

[68] V. Ryjkov, X. Zhao, and H. Schuessler, "Sympathetic cooling of fullerene ions by laser-cooled Mg^+ ions in a linear rf traps," Physical Review A **74**, 023401 (2006).

[69] T. Hasegawa and T. Shimizu, "Limiting temperature of sympathetically cooled ions in a radio-frequency trap," Physical Review A **67**, 013408 (2003).

[70] A. Ostendorf, C. B. Zhang, M. A. Wilson, D. Offenberg, B. Roth, and S. Schiller, "Sympathetic cooling of complex molecular ions to millikelvin temperatures," Physical Review Letters **97**, 243005 (2006).

[71] S. Schiller and C. Lämmerzahl, "Molecular dynamics simulation of sympathetic crystallization of molecular ions," Physical Review A **68**, 053406 (2003).

[72] M. D. Barrett, B. DeMarco, T. Schaetz, V. Meyer, D. Leibfried, J. Britton, J. Chiaverini, W. M. Itano, B. Jelenković, J. D. Jost, C. Langer, T. Rosenband, and D. J. Wineland, "Sympathetic cooling of $^9Be^+$ and $^{24}Mg^+$ for quantum logic," Physical Review A **68**, 042302 (2003).

[73] V. Alekseev, D. Krylova, and V. Letokhov, "Sympathetic cooling of 2 trapped ions," Physica Scripta **51**, 368–372 (1995).

[74] D. Kielpinski, B. E. King, C. J. Myatt, C. A. Sackett, Q. A. Turchette, W. M. Itano, C. Monroe, D. J. Wineland, and W. H. Zurek, "Sympathetic cooling of trapped ions for quantum logic," Physical Review A **61**, 032310 (2000).

[75] G. Morigi and H. Walther, "Two-species Coulomb chains for quantum information," European Physical Journal D **13**, 261–269 (2001).

[76] T. Hasegawa and T. Shimizu, "Observation and temperature measurement

of sympathetically cooled ions in an rf trap," IEEE Transactions on Instrumentation and Measurement **50**, 556 –558 (2001).

[77] R. Blümel, C. Kappler, W. Quint, and H. Walther, "Chaos and order of laser-cooled ions in a paul trap," Physical Review A **40**, 808–823 (1989).

[78] J. Prestage, A. Williams, L. Maleki, M. Djomehri, and E. Harabetian, "Dynamics of charged-particles in a paul radiofrequency quadrupole trap," Physical Review Letters **66**, 2964–2967 (1991).

[79] V. Ryjkov, X. Zhao, and H. Schuessler, "Simulations of the rf heating rates in a linear quadrupole ion trap," Physical Review A **71**, 033414 (2005).

[80] J. Schiffer, M. Drewsen, J. Hangst, and L. Hornekaer, "Temperature, ordering, and equilibrium with time-dependent confining forces," Proceedings of the National Academy of Sciences of the United States of America **97**, 10697–10700 (2000).

[81] I. M. Buluta, M. Kitaoka, S. Georgescu, and S. Hasegawa, "Investigation of planar Coulomb crystals for quantum simulation and computation," Physical Review A **77**, 062320 (2008).

[82] Y. Maeno, M. Tachikawa, Y. Moriwaki, and T. Shimizu, "Dynamics of trapped ions in the presence of laser cooling and radiofrequency heating," Japanese Journal of Applied Physics Part 2 - Letters **34**, L174–L176 (1995).

[83] D. James, "Quantum dynamics of cold trapped ions with application to quantum computation," Applied Physics B: Lasers and Optics **66**, 181–190 (1998).

[84] J. P. Schiffer, "Phase transitions in anisotropically confined ionic crystals," Physical Review Letters **70**, 818–821 (1993).

[85] D. Enzer, M. Schauer, J. Gomez, M. Gulley, M. Holzscheiter, P. Kwiat, S. Lamoreaux, C. Peterson, V. Sandberg, D. Tupa, A. White, R. Hughes, and D. James, "Observation of power-law scaling for phase transitions in linear trapped ion crystals," Physical Review Letters **85**, 2466–2469 (2000).

[86] C. Zhang, D. Offenberg, B. Roth, M. Wilson, and S. Schiller, "Molecular-dynamics simulations of cold single-species and multispecies ion ensembles in a linear paul trap," Physical Review A **76**, 012719 (2007).

[87] American Radio Relay League, *The ARRL Handbook for radio amateurs 2000, 77th ed.* (ARRL publishers, 1999).

[88] U. Brinkmann, W. Hartig, H. Telle, and H. Walther, "Isotope selective photoionization of calcium using 2-step laser excitation," Applied Physics A: Materials Science & Processing **5**, 109–115 (1974).

[89] N. Kjaergaard, L. Hornekaer, A. Thommesen, Z. Videsen, and M. Drewsen, "Isotope selective loading of an ion trap using resonance-enhanced two-photon ionization," Applied Physics B-Lasers and Optics **71**, 207–210 (2000).

[90] D. Lucas, A. Ramos, J. Home, M. McDonnell, S. Nakayama, J. Stacey, S. Webster, D. Stacey, and A. Steane, "Isotope-selective photoionization for calcium ion trapping," Physical Review A **69** (2004).

[91] T. Hänsch and B. Couillaud, "Laser frequency stabilization by polarization spectroscopy of a reflecting reference cavity," Optics Communications **35**, 441 – 444 (1980).

[92] K. Rosman and P. Taylor, "Isotopic compositions of the elements 1997," Pure and Applied Chemistry **70**, 217–235 (1998).

[93] R. Boyd, *Nonlinear optics* (Academic Press, 2009).

[94] J. Goodberlet, J. Wang, J. G. Fujimoto, and P. A. Schulz, "Femtosecond passively mode-locked Ti:Al_2O_3 laser with a nonlinear external cavity," Optics Letters **14**, 1125–1127 (1989).

[95] J. Herrmann, "Starting dynamic, self-starting condition and mode-locking threshold in passive, coupled-cavity or kerr-lens mode-locked solid-state lasers," Optics Communications **98**, 111–116 (1993).

[96] J. Herrmann, "Theory of kerr-lens mode-locking - role of self-focusing and radially varying gain," Journal of the Optical Society of America B-Optical Physics **11**, 498–512 (1994).

[97] R. Fork, O. Martinez, and J. Gordon, "Negative dispersion using pairs of prisms," Optics Letters **9**, 150–152 (1984).

[98] E. Treacy, "Optical pulse compression with diffraction gratings," Quantum Electronics, IEEE Journal of **5**, 454 – 458 (1969).

[99] R. Szipöcs, K. Ferencz, C. Spielmann, and F. Krausz, "Chirped multilayer coatings for broadband dispersion control in femtosecond lasers," Optics Letters **19**, 201–203 (1994).

[100] J. Zhou, G. Taft, C.-P. Huang, M. Murnane, H. Kapteyn, and I. Christov,

"Pulse evolution in a broad-bandwidth ti:sapphire laser," Optics Letters **19**, 1149–1151 (1994).

[101] H. A. Macleod, *Thin film optical filters* (Institute Of Physics publishing, 2001).

[102] D. Babic and S. Corzine, "Analytic expressions for the reflection delay, penetration depth, and absorptance of quarter-wave dielectric mirrors," IEEE Journal of Quantum Electronics **28**, 514–524 (1992).

[103] Agrawal, *Nonlinear fiber optics* (Academic Press, 2007).

[104] U. Keller, "Ultrafast solid-state lasers," (Elsevier Science B.V., 2004), pp. 1–115.

[105] M. Sander, J. Birge, A. Benedick, H. Crespo, and F. Kärtner, "Dynamics of dispersion managed octave-spanning titanium:sapphire lasers," Journal of the Optical Society of America B **26**, 743–749 (2009).

[106] U. Morgner, F. X. Kärtner, S. H. Cho, Y. Chen, H. A. Haus, J. G. Fujimoto, E. P. Ippen, V. Scheuer, G. Angelow, and T. Tschudi, "Sub-two-cycle pulses from a kerr-lens mode-locked ti:sapphire laser," Optics Letters **24**, 411–413 (1999).

[107] S. Witte, "Terawatt-intensity few-cycle laser pulses," Ph.D. thesis, Vrije Universiteit Amsterdam (2007).

[108] S. Witte, R. Zinkstok, A. Wolf, W. Hogervorst, W. Ubachs, and K. Eikema, "A source of 2 terawatt, 2.7 cycle laser pulses based on noncollinear optical parametric chirped pulse amplification," Optics Express **14**, 8168–8177 (2006).

[109] R. Fox, S. Diddams, A. Bartels, and L. Hollberg, "Optical frequency measurements with the global positioning system: tests with an iodine-stabilized He-Ne laser," Applied Optics **44**, 113–120 (2005).

[110] R. van Rooij, W. Vassen, and et al., "Precision spectroscopy of the triplet to singlet transition in metastable helium," To be published.

[111] "NIST GPS data archive," http://www.nist.gov/physlab/div847/grp40/gpsarchive.cfm.

[112] T. Fortier, D. Jones, and S. T. Cundiff, "Phase stabilization of an octave-spanning ti:sapphire laser," Optics Letters **28**, 2198–2200 (2003).

[113] O. Mücke, R. Ell, A. Winter, J.-W. Kim, J. Birge, L. Matos, and

F. Kärtner, "Self-referenced 200 MHz octave-spanning ti:sapphire laser with 50 attosecond carrier-envelope phase jitter," Optics Express **13**, 5163–5169 (2005).

[114] T. Fortier, A. Bartels, and S. Diddams, "Octave-spanning Ti:sapphire laser with a repetition rate >1 GHz for optical frequency measurements and comparisons," Opt. Lett. **31**, 1011–1013 (2006).

[115] J. Ranka, R. Windeler, and A. Stentz, "Visible continuum generation in air-silica microstructure optical fibers with anomalous dispersion at 800 nm," Optics Letters **25**, 25–27 (2000).

[116] J. Dudley, G. Genty, and C. Stéphane, "Supercontinuum generation in photonic crystal fiber," Reviews of Modern Physics **78**, 1135–1184 (2006).

[117] F. Helbing, G. Steinmeyer, U. Keller, R. Windeler, J. Stenger, and H. Telle, "Carrier-envelope offset dynamics of mode-locked lasers," Optics Letters **27**, 194–196 (2002).

[118] K. Holman, R. Jones, A. Marian, S. Cundiff, and J. Ye, "Detailed studies and control of intensity-related dynamics of femtosecond frequency combs from mode-locked Ti:sapphire lasers," IEEE Journal of Selected Topics in Quantum Electronics **9**, 1018–1024 (2003).

[119] L. Matos, O. Mucke, J. Chen, and F. Kartner, "Carrier-envelope phase dynamics and noise analysis in octave-spanning Ti:sapphire lasers," Optics Express **14**, 2497–2511 (2006).

[120] M. Sander, E. Ippen, and F. Kartner, "Carrier-envelope phase dynamics of octave-spanning dispersion-managed Ti:sapphire lasers," Optics Express **18**, 4948–4960 (2010).

[121] H. A. Haus and E. P. Ippen, "Group velocity of solitons," Optics Letters **26**, 1654–1656 (2001).

[122] D. Anderson and M. Lisak, "Nonlinear asymmetric self-phase modulation and self-steepening of pulses in long optical waveguides," Physical Review A **27**, 1393–1398 (1983).

[123] T. Brabec and F. Krausz, "Nonlinear optical pulse propagation in the single-cycle regime," Physical Review Letters **78**, 3282–3285 (1997).

[124] B. I. des Poids et Mesures, *The international system of units* (Bureau International des Poids et Mesures, 2006).

[125] S. Jefferts, T. Heavner, T. Parker, and J. Shirley, "Nist cesium fountains: current status and future prospects," (SPIE, 2007), vol. 6673, p. 667309.

[126] T. Parker, "Long-term comparison of caesium fountain primary frequency standards," Metrologia **47**, 1–10 (2010).

[127] L. Essen and J. Parry, "Caesium resonator," Nature **176**, 281–282 (1955).

[128] A. Clairon, S. Ghezali, G. Santarelli, P. Laurent, E. Simon, S. Lea, M. Bahoura, S. Weyers, and K. Szymaniec, "The LPTF preliminary accuracy evaluation of cesium fountain frequency standard," IEE Conference Publications **1996**, 218–223 (1996).

[129] D. Allan, "Statistics of atomic frequency standards," Proceedings of the Institute of Electrical and Electronics Engineers **54**, 221–& (1966).

[130] A. Bartels, C. Oates, L. Hollberg, and S. Diddams, "Stabilization of femtosecond laser frequency combs with subhertz residual linewidths," Optics Letters **29**, 1081–1083 (2004).

[131] A. Marian, M. Stowe, J. Lawall, D. Felinto, and J. Ye, "United time-frequency spectroscopy for dynamics and global structure," Science **306**, 2063–2068 (2004).

[132] S. Witte, R. Zinkstok, W. Ubachs, W. Hogervorst, and K. Eikema, "Deep-ultraviolet quantum interference metrology with ultrashort laser pulses," Science **307**, 400–403 (2005).

[133] R. T. Zinkstok, S. Witte, W. Ubachs, W. Hogervorst, and K. S. E. Eikema, "Frequency comb laser spectroscopy in the vacuum-ultraviolet region," Phys. Rev. A **73**, 061801 (2006).

[134] D. Z. Kandula, C. Gohle, T. J. Pinkert, W. Ubachs, and K. S. E. Eikema, "Extreme ultraviolet frequency comb metrology," Phys. Rev. Lett. **105**, 063001 (2010).

[135] M. Stowe, M. Thorpe, A. Pe'er, J. Ye, J. Stalnaker, V. Gerginov, and S. Diddams, "Direct frequency comb spectroscopy," **55**, 1–60 (2008).

[136] T. Fortier, Y. Le Coq, J. Stalnaker, D. Ortega, S. Diddams, C. Oates, and L. Hollberg, "Kilohertz-resolution spectroscopy of cold atoms with an optical frequency comb," Physical Review Letters **97**, 163905 (2006).

[137] J. Stalnaker, Y. L. Coq, T. Fortier, S. Diddams, C. Oates, and L. Hollberg, "Measurement of excited-state transitions in cold calcium atoms by

direct femtosecond frequency-comb spectroscopy," Physical Review A **75**, 040502 (2007).

[138] A. L. Wolf, J. Morgenweg, J. C. J. Koelemeij, S. A. van den Berg, W. Ubachs, and K. S. E. Eikema, "Direct frequency-comb spectroscopy of a dipole-forbidden clock transition in trapped $^{40}Ca^{+}$ ions," Opt. Lett. **36**, 49–51 (2011).

[139] S. Diddams, L. Hollberg, and V. Mbele, "Molecular fingerprinting with the resolved modes of a femtosecond laser frequency comb," Nature **445**, 627–630 (2007).

[140] C. Gohle, B. Stein, A. Schliesser, T. Udem, and T. Haensch, "Frequency comb vernier spectroscopy for broadband, high-resolution, high-sensitivity absorption and dispersion spectra," Physical Review Letters **99**, 263902 (2007).

[141] M. Thorpe, D. Balslev-Clausen, M. Kirchner, and J. Ye, "Cavity-enhanced optical frequency comb spectroscopy: application to human breath analysis," Optics Express **16**, 2387–2397 (2008).

[142] M. Thorpe, K. Moll, R. Jones, B. Safdi, and J. Ye, "Broadband cavity ringdown spectroscopy for sensitive and rapid molecular detection," Science **311**, 1595–1599 (2006).

[143] S. Schiller, "Spectrometry with frequency combs," Optics Letters **27**, 766–768 (2002).

[144] F. Keilmann, C. Gohle, and R. Holzwarth, "Time-domain mid-infrared frequency-comb spectrometer," Optics Letters **29**, 1542–1544 (2004).

[145] A. Schliesser, M. Brehm, F. Keilmann, and D. v.d. Weide, "Frequency-comb infrared spectrometer for rapid, remote chemical sensing," Optics Express **13**, 9029–9038 (2005).

[146] I. Coddington, W. Swann, and N. Newbury, "Coherent multiheterodyne spectroscopy using stabilized optical frequency combs," Physical Review Letters **100**, 013902 (2008).

[147] B. Bernhardt, A. Ozawa, P. Jacquet, M. Jacquey, T. Kobayashi, Y.and Udem, R. Holzwarth, G. Guelachvili, T. Hänsch, and N. Picque, "Cavity-enhanced dual-comb spectroscopy," Nature Photonics **4**, 55–57 (2010).

[148] M. Murphy, J. Webb, and V. Flambaum, "Further evidence for a variable

fine-structure constant from keck/hires qso absorption spectra," Monthly Notices of the Royal Astronomical Society **345**, 609–638 (2003).

[149] J. Berengut, "Isotope shifts and relativistic shifts in atomic spectra," Ph.D. thesis (2006).

[150] K. Toyoda, H. Naka, H. Kitamura, H. Sawamura, and S. Urabe, "Sideband-resolved spectroscopy on the $4\,^2S_{1/2} - 3\,^2D_{5/2}$ transition in single calcium ions by use of fundamental waves of diode lasers," Optics Letters **29**, 1270–1272 (2004).

[151] C. Roos, T. Zeiger, H. Rohde, H. Nagerl, J. Eschner, D. Leibfried, F. Schmidt-Kaler, and R. Blatt, "Quantum state engineering on an optical transition and decoherence in a Paul traps," Physical Review L **83**, 4713–4716 (1999).

[152] C. Roos, M. Riebe, H. Haffner, W. Hansel, J. Benhelm, G. Lancaster, C. Becher, F. Schmidt-Kaler, and R. Blatt, "Control and measurement of three-qubit entangled states," Science **304**, 1478–1480 (2004).

[153] D. C. Morton, "Atomic data for resonance absorption lines. iii. wavelengths longward of the lyman limit for the elements hydrogen to gallium," The Astrophysical Journal Supplement Series **149**, 205 (2003).

[154] U. Litzén, "Private communication," (2008).

[155] B. Edlen and P. Risberg, "The spectrum of singly-ionized calcium, Ca-II," Arkiv for Fysik **10**, 553–566 (1956).

[156] F. Diedrich, E. Peik, J. M. Chen, W. Quint, and H. Walther, "Observation of a phase transition of stored laser-cooled ions," Physical Review Letters **59**, 2931–2934 (1987).

[157] L.-S. Ma, M. Zucco, S. Picard, L. Robertsson, and R. Windeler, "A new method to determine the absolute mode number of a mode-locked femtosecond-laser comb used for absolute optical frequency measurements," IEEE Journal of Selected Topics in Quantum Electronics **9**, 1066 – 1071 (2003).

[158] J. Jin and D. Church, "Excited-level lifetimes and hyperfine-structure measurements on ions using collinear laser ion-beam spectroscopy," Physical Review A **49**, 3463–3471 (1994).

[159] M. Fischer, N. Kolachevsky, M. Zimmermann, R. Holzwarth, T. Udem, T. Hansch, M. Abgrall, J. Grunert, I. Maksimovic, S. Bize, H. Marion,

F. Dos Santos, P. Lemonde, G. Santarelli, P. Laurent, A. Clairon, C. Salomon, M. Haas, U. Jentschura, and C. Keitel, "New limits on the drift of fundamental constants from laboratory measurements," Physical Review Letters **92** (2004).

[160] R. Thompson, "Spectroscopy of trapped ions," in "Advances in Atomic, Molecular and Optical Physics, vol. 31," (Academic Press Inc., 1993), pp. 63–136.

[161] M. Herrmann, V. Batteiger, S. Knünz, G. Saathoff, T. Udem, and T. W. Hänsch, "Frequency metrology on single trapped ions in the weak binding limit: The $3s_{1/2} - 3p_{3/2}$ transition in $^{24}Mg^{+}$," Physical Review Letters **102**, 013006 (2009).

[162] V. Gerginov, C. Tanner, S. Diddams, A. Bartels, and L. Hollberg, "High-resolution spectroscopy with a femtosecond laser frequency comb," Optics Letters **30**, 1734–1736 (2005).

[163] P. Fendel, S. Bergeson, T. Udem, and T. Haensch, "Two-photon frequency comb spectroscopy of the 6s-8s transition in cesium," Optics Letters **32**, 701–703 (2007).

[164] D. Larson, J. Bergquist, J. Bollinger, W. Itano, and D. Wineland, "Sympathetic cooling of trapped ions: A laser-cooled two-species nonneutral ion plasma," Physical Review Letters **57**, 70–73 (1986).

[165] L. Hornekær, N. Kjærgaard, A. M. Thommesen, and M. Drewsen, "Structural properties of two-component coulomb crystals in linear paul traps," Physical Review Letters **86**, 1994–1997 (2001).

[166] J. Ranka, R. Windeler, and A. Stentz, "Optical properties of high-delta air-silica microstructure optical fibers," Optics Letters **25**, 796–798 (2000).

[167] R. Jones, K. Moll, M. Thorpe, and J. Ye, "Phase-coherent frequency combs in the vacuum ultraviolet via high-harmonic generation inside a femtosecond enhancement cavity," Physical Review Letters **94**, 193201 (2005).

[168] C. Gohle, T. Udem, M. Herrmann, J. Rauschenberger, R. Holzwarth, H. Schuessler, F. Krausz, and T. Hansch, "A frequency comb in the extreme ultraviolet," Nature **436**, 234–237 (2005).

[169] J. Bergquist, W. Itano, and D. Wineland, "Recoilless optical absorption and doppler sidebands of a single trapped ion," Physical Review A **36**, 428–430

(1987).

[170] S. Urabe, M. Watanabe, H. Imajo, and K. Hayasaka, "Laser cooling of trapped Ca^+ and measurement of the $3^2D_{5/2}$ state lifetime," Optics Letters **17**, 1140–1142 (1992).

[171] H. Nagerl, W. Bechter, J. Eschner, F. Schmidt-Kaler, and R. Blatt, "Ion strings for quantum gates," Applied Physics B-Lasers and Optics **66**, 603–608 (1998).

[172] G. Ritter, S. Bae, and U. Eichmann, "All-diode-laser cooling of single Ca^+ ions," Applied Physics B-Lasers and Optics **66**, 609–612 (1998).

[173] O. Martinez, "Achromatic phase matching for 2nd harmonic-generation of femtosecond pulses," IEEE Journal of Quantum Electronics **25**, 2464–2468 (1989).

[174] R. Gerritsma, G. Kirchmair, F. Zaehringer, J. Benhelm, R. Blatt, and C. F. Roos, "Precision measurement of the branching fractions of the $4p\,^2P_{3/2}$ decay of Ca II," European Physical Journal D **50**, 13–19 (2008).

[175] Y. Ralchenko, "NIST Atomic Spectra Database (version 3.1.5)," [Online] (2008).

[176] L. Matos, D. Kleppner, O. Kuzucu, T. Schibli, J. Kim, E. Ippen, and F. Kaertner, "Direct frequency comb generation from an octave-spanning, prismless ti:sapphire laser," Optics Letters **29**, 1683–1685 (2004).

[177] R. Blatt and P. Zoller, "Quantum jumps in atomic systems," European Journal of Physics **9**, 250 (1988).

[178] M. Herrmann, M. Haas, U. Jentschura, F. Kottmann, D. Leibfried, G. Saathoff, C. Gohle, A. Ozawa, V. Batteiger, S. Knünz, N. Kolachevsky, H. Schüssler, T. Hänsch, and T. Udem, "Feasibility of coherent xuv spectroscopy on the $1s-2s$ transition in singly ionized helium," Physical Review A **79**, 052505 (2009).

[179] W. Rellergert, D. DeMille, R. R. Greco, M. Hehlen, J. Torgerson, and E. Hudson, "Constraining the evolution of the fundamental constants with a solid-state optical frequency reference based on the Th-229 nucleus," Physical Review Letters **104**, 200802 (2010).

Summary

Frequency is currently the physical quantity which can be measured to the highest precision. The record in accuracy for such a measurement was obtained in a comparison of the $^1S_0 - ^3P_0$ transition in two $^{27}Al^+$ clocks, where an inaccuracy of 9 parts in 10^{18} was obtained [1]. The described experiment uses the combination of a Paul trap for confinement and a frequency comb for calibration. This combination provides an ideal tool for spectroscopy experiments, because the ions in a trap can be directly or sympathetically cooled and studied with a long interaction time, while a frequency comb adds a broad range of wavelengths for spectroscopy. In the work described in this thesis, we combine the advantages of ion trapping with (direct) frequency comb spectroscopy. We trap and study $^{40}Ca^+$, which is of interest for applications in ion clocks, the search for a variation of the fine-structure constant and quantum computing, as is described in Chapter 1.

For our experiments, two types of linear Paul traps have been constructed, which are discussed in Chapter 2. A linear Paul trap uses electric fields to trap ions. The field is formed by a combination of oscillating Radio Frequency (RF) fields for radial confinement, and DC electric fields on so-called endcaps to trap the ion in the axial direction. The first ion trap that we have constructed uses four elongated RF electrodes for radial trapping, and two ring electrodes to which the endcap potential is applied. Ions are made from a neutral beam of evaporated calcium atoms, which is photo-ionized inside the trapping region. The trapped ions are laser cooled using only diode lasers, with the combination of a cooling laser at 397 nm on the $4s\,^2S_{1/2} - 4p\,^2P_{1/2}$ transition and a repumper laser at 866 nm on the $3d\,^2D_{3/2} - 4p\,^2P_{1/2}$-transition. With this method calcium ions have succesfully been trapped and laser cooled to crystallization. The first trap has been employed in two experiments on dipole-allowed transitions in calcium ions, which are described in Chapter 5 and 6.

A second ion trap has been developed with a combination of two RF electrodes that extend over the full length of the trap, and two segmented electrodes which serve both as endcap electrodes and for correction of patch potentials. In this trap calcium ions are made and laser cooled using the same methods as described for the first trap. The second trap has been employed for an experiment on direct frequency comb spectroscopy of a dipole-forbidden (clock) transition in $^{40}Ca^+$, as is described in Chapter 7.

Besides the ion traps, two frequency combs have been constructed, for the purpose of high precision spectroscopy of transitions in the trapped ions. These combs are the subject of chapter 3. Both frequency combs are based on a Ti:Sa laser, in which Kerr-lens mode locking together with group velocity dispersion control and a broadband gain spectrum makes the generation of ultrashort pulses possible. We have built a laser with a broadband spectrum that is used as a seed laser for a noncollinear optical parametric chirped pulse amplifier, and a laser with a narrower spectrum for the purpose of direct frequency comb spectroscopy.

A frequency comb can be used in two ways to calibrate a transition frequency: either through an intermediate cw laser, or by directly exciting the transition of interest. In the first case, a resonance is detected using the cw laser, while the laser frequency is calibrated against the frequency comb. In the case of direct frequency comb spectroscopy, the comb is used both for excitation and calibration. However, the power from a comb mode usually is orders of magnitude lower than for the case with a cw laser. For a one-photon transition, an additional disadvantage is the presence of a large number of background modes, while only one mode at a time can excite the transition. We have performed both types of experiments on transitions in calcium ions, using the method of shelving to overcome the signal-to-noise issues of direct frequency comb spectroscopy.

The three frequency metrology experiments that we performed on trapped and cooled calcium ions are described in Chapter 5-7. The first experiment is the calibration of the $4s\,^2\mathrm{S}_{1/2} - 4p\,^2\mathrm{P}_{1/2}$ transition, which is described in Chapter 5. In this experiment, a frequency doubled diode laser is used to excite the transition, while the fundamental laser wavelength at 794 nm is calibrated against a frequency comb. The ion fluorescence is measured using a Photomultiplier Tube (PMT). The total measurement, accounting for the measured systematic effects, yielded a transition frequency of $\nu = 755\,222\,766.2\,(1.7)$ MHz. The obtained accuracy presents an order of magnitude improvement over the previous most accurate result.

A second spectroscopy experiment was conducted on the $4s\,^2\mathrm{S}_{1/2} - 4p\,^2\mathrm{P}_{3/2}$ transition at 393.5 nm, which is the subject of Chapter 6. For the excitation of the transition a frequency comb was employed directly, which was frequency doubled at full repetition rate. The signal-to-noise issue described earlier is overcome by employing a shelving scheme, using the 7 % chance of excited ions to decay to the long-lived $3d\,^2\mathrm{D}_{5/2}$ energy level. By monitoring the cooling laser fluorescence with a PMT, while the $4s\,^2\mathrm{S}_{1/2} - 4p\,^2\mathrm{P}_{3/2}$ transition is resonantly excited with the frequency comb, the excitation can be indirectly detected through a decrease of fluorescence on the cooling transition. The cooling laser fluorescence is alternately measured with and without a repumper on the $3d\,^2\mathrm{D}_{5/2} - 4p\,^2\mathrm{P}_{3/2}$ transition,

collecting both signal and background. These two datasets are subtracted and corrected for loss of ions from the trap. The determined $4s\,^2\mathrm{S}_{1/2} - 4p\,^2\mathrm{P}_{3/2}$ transition frequency in $^{40}\mathrm{Ca}^+$ is $\nu = 761\,905\,012.7\,(0.5)$ MHz, improving the best previously known value by more than two orders of magnitude.

In Chapter 7 a third experiment is described, where direct frequency comb spectroscopy applied to a dipole-forbidden clock transition: the $4s\,^2\mathrm{S}_{1/2} - 3d\,^2\mathrm{D}_{5/2}$ transition at 729.5 nm. The natural linewidth of this transition is 0.14 Hz which, combined with the low power per comb mode in modes of $\sim$ 2 MHz linewidth, leads to a very low excitation rate of $\sim$ 7 per ion per 1000 seconds. Despite this low rate, the transition can still be detected by again using shelving in the $3d\,^2\mathrm{D}_{5/2}$ state. A string of 10 calcium ions is created, and its cooling laser fluorescence is imaged onto an electron-multiplying CCD camera. When an ion is excited to the $3d\,^2\mathrm{D}_{5/2}$ state, it will turn dark in the camera image for the lifetime of the ion of about 1 second, since it no longer participates in the cooling cycle. The dark ions are detected, and the rate of ions turning dark is measured as a function of the excitation wavelength. Using this method, we found a transition frequency of $\nu = 411\,042\,129.6\,(0.3)$ MHz, which is consistent with previously reported measurements [27]. The accuracy and measurement rate of this experiment is currently limited by the Doppler temperature of the trapped ions, in combination with the linewidth of the comb modes. It can be improved upon by trapping and probing the ions in the Lamb-Dicke regime, in combination with a reduction of the comb mode linewidth by locking to a high-finesse optical cavity.

In conclusion, in this thesis the versatility of (direct) frequency comb spectroscopy in an ion trap is demonstrated through several experiments on calcium ions. We have shown that transitions can be calibrated both in the infrared and in the visible frequency regime. These experiments demonstrate the wide range of wavelengths that can be accessed for direct frequency comb spectroscopy using a single laser. In addition, the method of direct frequency comb spectroscopy has been applied to measure both a dipole allowed and an electric quadrupole transition. These results illustrate the possibility to employ the combination of a frequency comb and an ion trap for a wide range of calibration purposes.

Samenvatting

Frequentie is de fysische grootheid die met de grootste nauwkeurigheid gemeten kan worden. Het record voor een dergelijke meting is behaald op de $^1\mathrm{S}_0 - ^3\mathrm{P}_0$-overgang in $^{27}\mathrm{Al}^+$ ionen, waarvan de overgangsfrequentie is gemeten met een relatieve nauwkeurigheid van 9×10^{-18} [1]. Dit experiment maakt gebruik van de combinatie van een zogenaamde Paul val om ionen vast te houden, met een frequentiekamlaser om overgangen te calibreren. Deze combinatie is ideaal voor het doen van spectroscopie. In de eerste plaats omdat ionen in een val (direct of indirect) gekoeld kunnen worden met lasers en ze daarom lang gevangen en bestudeerd kunnen worden. Het tweede grote voordeel is dat met de frequentiekam overgangen gemeten kunnen worden over een breed spectrum van frequenties. In de experimenten die in dit proefschrift beschreven worden, combineren we de voordelen van het opsluiten van ionen in een val met (directe) frequentiekam-spectroscopie. Het ion dat we hiervoor gebruiken is $^{40}\mathrm{Ca}^+$. Dit ion heeft toepassingen in ionenklokken, het zoeken naar een verandering in natuurconstantes en quantumcomputers zoals is beschreven in Hoofdstuk 1.

Om deze experimenten uit te voeren hebben we twee verschillende lineare Paul vallen gebouwd, die beschreven zijn in Hoofdstuk 2. In zo'n lineare Paul val worden ionen gevangen met behulp van electrische velden. De velden worden gecreëerd met behulp van oscillerende velden in radiële richting, gecombineerd met statische velden op de zogenaamde eindelectrodes. Op deze manier worden de ionen in alle richtingen opgesloten. De eerste ionenval die we gebouwd hebben, bestond uit vier cilindrische electrodes met een oscillerend electrisch veld, en twee ringvormige electrodes als eindelectrodes. De calcium ionen worden gemaakt door neutraal calcium te verdampen uit een oventje, om de atomen vervolgens te fotoioniseren in de ionenval met behulp van lasers. De ionen worden gevangen in de val, waar ze worden afgekoeld met behulp van diodelasers. Hiervoor wordt de combinatie van een koellaser bij 397 nm op de $4s\,^2\mathrm{S}_{1/2} - 4p\,^2\mathrm{P}_{1/2}$-overgang en een zogenaamde repumper bij 866 nm op de $3d\,^2\mathrm{D}_{3/2} - 4p\,^2\mathrm{P}_{1/2}$-overgang gebruikt. Op deze manier hebben we calcium ionen gevangen en afgekoeld tot ze een kristalrooster vormen. De eerste ionenval is gebruikt voor de uitvoering van twee experimenten op toegestane overgangen in calcium (Hoofdstuk 5 en 6).

Na deze ionenval is een tweede ionenval gemaakt. Deze val bestaat uit twee electrodes met een oscillerend veld over de gehele lengte van de val, gecombi-

neerd met twee gesegmenteerde electrodes die gebruikt worden als eindelectrodes. Daarnaast kunnen de gesegmenteerde electrodes gebruikt worden om te corrigeren voor strooivelden. In deze ionenval kunnen calcium ionen op dezelfde manier worden gevangen en afgekoeld als in de eerste ionenval. In deze tweede val is een experiment uitgevoerd waarbij directe frequentiekam-spectroscopie op een zogenaamde klokovergang in $^{40}Ca^{+}$ is toegepast (Hoofdstuk 7).

Naast de ionenvallen hebben we ook twee frequentiekamlasers ontwikkeld, om te gebruiken voor precisiespectroscopie van overgangen in gevangen ionen. In Hoofdstuk 3 worden deze frequentiekammen beschreven. Beide frequentiekamlasers zijn Ti:Sa lasers, een type gepulste lasers waarin de combinatie van het Kerr-effect, controle over dispersie van de groepssnelheid en breedbandige versterking ervoor zorgt dat er ultrakorte pulsen gemaakt kunnen worden. Eén van deze lasers produceerde een breedbandig output spectrum om te gebruiken voor versterking in een niet-collineaire optische parametrische gechirpte puls versterker. De andere laser had een smaller spectrum, wat gunstig is voor de toepassing in directe frequentiekam-spectroscopie.

Een frequentiekamlaser kan op twee manieren gebruikt waren om een overgangsfrequentie te meten: De meest toegepaste methode gebruikt een extra continue laser voor excitatie, waarvan de golflengte gecalibreerd wordt met behulp van de frequentiekam. De tweede methode gebruikt het licht in de kamlijnen direct voor excitatie. De eerste methode heeft het voordeel dat er meestal ordes van grootte meer licht bij de overgangsfrequentie beschikbaar is in een cw laser dan in de frequentiekam. In het geval dat er wordt geëxciteerd met één foton, komt daar nog bij dat er in de kam een groot aantal modes aanwezig is die voor een achtergrondsignaal zorgen, terwijl maar één mode gebruikt wordt voor het aanslaan van de overgang. Daar staat tegenover dat in de frequentiekam direct een breed spectrum aan golflengtes beschikbaar is voor de spectroscopie, terwijl de cw laser doorgaans maar over een smal golflengtegebied te gebruiken is. Door de kam direct voor de excitatie te gebruiken, kunnen daarom vele overgangen gemeten worden met één laser. Wij hebbenbeide methodes gebruikt voor het meten van overgangen in calcium ionen, waarbij een 'shelving'-techniek gebruikt wordt om de signaal-ruis verhouding in de directe frequentiekam-spectroscopie te verbeteren.

De Hoofdstukken 5-7 beschrijven de drie metrologie-experimenten die we hebben uitgevoerd. Het eerste experiment (Hoofdstuk 5) is het meten van de $4s\,^2\mathrm{S}_{1/2}-4p\,^2\mathrm{P}_{1/2}$-overgangsfrequentie. In dit experiment wordt een frequentieverdubbelde diodelaser gebruikt om de overgang mee aan te slaan, en wordt de (onverdubbelde) lasergolflengte bij 794 nm gemeten met de frequentiekam. Op deze manier is een overgangsfrequentie van $\nu = 755\,222\,766.2\,(1.7)$ MHz geme-

ten, waarbij systematische effecten in het resultaat zijn meegenomen. De behaalde nauwkeurigheid is een orde van grootte beter dan het meest nauwkeurige bekende meetresultaat.

In een tweede experiment hebben we de overgangsfrequentie van de $4s\,^2\mathrm{S}_{1/2} - 4p\,^2\mathrm{P}_{3/2}$ overgang bij 393.5 nm gemeten (Hoofdstruk 6). Bij dit experiment is de kamlaser frequentieverdubbeld, en is het licht van de kamlijnen in de resulterende kam gebruikt om de overgang aan te slaan. Het eerder geschetste probleem van de signaal-ruisverhouding voor het aanslaan van een één-foton overgang kan worden opgelost door gebruik te maken van 'shelving': Van de aangeslagen ionen vervalt 7 % naar het $3d\,^2\mathrm{D}_{5/2}$-niveau, dat een levensduur heeft van 1 seconde. Omdat de koellaser deze ionen niet meer exciteert, kunnen deze ionen gebruikt worden om het aanslaan van de overgang te detecteren. Door de fluorescentie die geïnduceerd wordt door de koellaser te meten, terwijl de $4s\,^2\mathrm{S}_{1/2} - 4p\,^2\mathrm{P}_{3/2}$-overgang resonant wordt aangeslagen, wordt het maken van de overgang indirect gemeten als een afname van fluorescentie van de koelovergang. De fluorescentie wordt afwisselend gemeten met en zonder een repumper op de $3d\,^2\mathrm{D}_{5/2} - 4p\,^2\mathrm{P}_{3/2}$-overgang, zodat zowel het signaal als de achtergrond gemeten worden. Deze twee datasets worden van elkaar afgetrokken en gecorrigeerd voor het verlies van ionen uit de val. De gemeten overgangsfrequentie van de $4s\,^2\mathrm{S}_{1/2} - 4p\,^2\mathrm{P}_{3/2}$-overgang in $^{40}\mathrm{Ca}^+$ is $\nu = 761\,905\,012.7\,(0.5)$ MHz. Dit resultaat is een verbetering in nauwkeurigheid van meer dan twee ordes van grootte ten opzichte van eerder behaalde resultaten op deze overgang.

In Hoofdstuk 7 wordt een derde experiment beschreven, waarbij directe frequentiekam-spectroscopie wordt toegepast op een smalbandige klokovergang: de $4s\,^2\mathrm{S}_{1/2} - 3d\,^2\mathrm{D}_{5/2}$ overgang bij 729.5 nm. De combinatie van de smalle natuurlijke lijnbreedte van deze overgang van 0.14 Hz met het lage vermogen per kammode in lijnen met een breedte van $\sim$ 2 MHz, leidt tot een zeer lage signaalsterkte van $\sim$ 7 overgangen per ion per 1000 s. Ondanks deze lage excitatiesnelheid, kan de overgang toch gedetecteerd worden door wederom 'shelving' in de $3d\,^2\mathrm{D}_{5/2}$-toestand toe te passen. In dit experiment wordt een rij van 10 calciumionen gebruikt, waarvan de koellaser-fluorescentie wordt afgebeeld op een EMCCD (electron-multiplying CCD) camera. Als een ion wordt aangeslagen naar de $3d\,^2\mathrm{D}_{5/2}$ toestand, dan wordt deze donker in de afbeelding op de camera, omdat de koellaser het ion niet langer kan aanslaan. Na ongeveer 1 seconde vervalt het ion weer naar de grondtoestand, en kan het opnieuw geëxciteerd worden. De donkere ionen worden gedetecteerd, en de hoeveelheid ionen die donker worden in 100 secondes wordt gemeten ten opzichte van de excitatiegolflengte. Zo hebben wij een overgangsfrequentie van $\nu = 411\,042\,129.6\,(0.3)$ MHz gemeten, een resultaat dat in overeenstemming is met andere gepubliceerde meetresultaten

[27]. De nauwkeurigheid en meetsnelheid van deze meting is momenteel beperkt door de Dopplertemperatuur van de gevangen ionen en de lijnbreedte van de frequentiekamlijnen. Deze twee factoren kunnen verbeterd worden door de ionen in het Lamb-Dicke regime te vangen en te meten, en de lijnbreedte van de kam te versmallen door deze te locken aan een optische resonator met hoge finesse.

In dit proefschrift wordt kortom de veelzijdigheid van (directe) frequentiekam-spectroscopie in een ionenval aangetoond, door middel van verschillende experimenten aan calcium ionen. We hebben laten zien dat de frequentiekam gebruikt kan worden om zowel bij infrarode als bij zichtbare golflengtes overgangen te calibreren. Dit laat zien dat het brede golflengtegebied dat bereikbaar is met de frequentiekam ingezet kan worden voor directe frequentiekam-spectroscopie. Daarnaast is de methode van directe frequentiekam-spectroscopie toegepast op zowel een dipool als een electrische quadrupool overgang. Deze resultaten laten zien dat de combinatie van een frequentiekam en een ionenval ingezet kan worden voor vele toepassingen in de calibratie van overgangsfrequenties.

List of publications

This thesis is based on the following publications:

Chapter 5:
A. L. Wolf, S. A. van den Berg, C. Gohle, E. J. Salumbides, W. Ubachs, and K. S. E. Eikema, "Frequency metrology on the $4s\,^2\mathrm{S}_{1/2} - 4p\,^2\mathrm{P}_{1/2}$ transition in $^{40}\mathrm{Ca}^+$ for a comparison with quasar data," Physical Review A **78**, 032511 (2008).

Chapter 6:
A. L. Wolf, S. A. van den Berg, W. Ubachs, and K. S. E. Eikema, "Direct frequency comb spectroscopy of trapped ions," Physical Review Letters **102**, 223901 (2009).

Chapter 7:
A. L. Wolf, J. Morgenweg, J. C. J. Koelemeij, S. A. van den Berg, W. Ubachs, and K. S. E. Eikema, "Direct frequency-comb spectroscopy of a dipole-forbidden clock transition in trapped $^{40}\mathrm{Ca}^+$ ions," Opt. Lett. **36**, 49–51 (2011).

Other publications to which the author contributed:

- E. J. Salumbides, V. Maslinskas, I. M. Dildar, A. L. Wolf, E.-J. van Duijn, K. S. E. Eikema, and W. Ubachs, "High-precision frequency measurement of the 423-nm Ca I line," Physical Review A **83**, 012502 (2011).

- E. J. Salumbides, D. Bailly, A. Khramov, A. L. Wolf, K. S. E. Eikema, M. Vervloet, and W. Ubachs, "Improved laboratory values of the H_2 lyman and werner lines for constraining time variation of the proton-to-electron mass ratio," Physical Review Letters **101**, 223001 (2008).

- D. Z. Kandula, A. Renault, C. Gohle, A. L. Wolf, S. Witte, W. Hogervorst, W. Ubachs, and K. S. E. Eikema, "Ultrafast double-pulse parametric amplification for precision Ramsey metrology," Optics Express **16**, 7071–7082 (2008).

- A. Renault, D. Z. Kandula, S. Witte, A. L. Wolf, R. T. Zinkstok, W. Hogervorst, and K. S. E. Eikema, "Phase stability of terawatt-class ultrabroadband parametric amplification," Optics Letters **32**, 2363–2365 (2007).

- S. Witte, R. Zinkstok, A. L. Wolf, W. Hogervorst, W. Ubachs, and K. S. E. Eikema, "A source of 2 terawatt, 2.7 cycle laser pulses based on noncollinear optical parametric chirped pulse amplification," Optics Express **14**, 8168–8177 (2006).

- M. Zhang, A. L. Wolf, L. Zhang, O. Tegus, E. Brück, G. Wu, and F. de Boer, "The structure, magnetism, and electrical-transport properties of the Heusler alloys $Co_2Cr_{1-x}Fe_xAl$ (x=0.2-0.6)," Journal of Applied Physics **97** (2005).

Dankwoord

Aan het einde van dit proefschrift wil graag van de gelegenheid gebruik maken om iedereen die mij geholpen heeft tijdens mijn promotie te bedanken.

In de eerste plaats natuurlijk Kjeld Eikema. Kjeld, ik heb ontzettend veel van je geleerd in de afgelopen jaren, van het uitlijnen van mijn eerste laser tot allerhande ingenieuze manieren om de experimenten werkend te krijgen en signalen uit te filteren. Bedankt voor je inzet en positief-kritische instelling, en veel succes met alle projecten die nu worden opgebouwd (wie weet zelfs ooit nog met een ionenval?).

Wim Ubachs, bedankt voor al het verrichte werk op het meer politieke en financiële vlak, en het in goede banen leiden van het FOM-IPP programma waar dit werk onder viel. Ik heb met veel plezier gewerkt in de atoom- en laserfysica-groep, die onder jouw leiding een groep is met een goede sfeer waar hard gewerkt wordt.

Ook wil ik graag mijn co-promotor Steven van den Berg bedanken. Steven, bedankt voor je inzet om dit project goed en efficient te laten verlopen, en je begrip voor de regelmatige aanpassingen in de plannen. Het was erg prettig om met je samen te werken, en ik heb veel geleerd van je gestructureerde aanpak.

Daarnaast zijn er vele mensen met wie ik met veel plezier heb samengewerkt. Roel, de tijd met jou en Stefan in het lab was erg gezellig. Je bereidheid om altijd te helpen bij mijn problemen maakte het begin van mijn experiment een stuk makkelijker, en ook je hulp bij al mijn computer- en programmeerproblemen worden erg gewaardeerd! Amandine, thanks for the great mental support at the times I really needed it! Maybe now we can finally start that anticipated chicken farm? Christoph, your knowledge of physics and experimenting, compared with a remarkably relaxed attitude, is impressive. Thank you for your help and forever changing my view on bbq-ing. Dominik, I enjoyed working with you and good luck on your new job in Berlin. Edcel, thank you for your flexibility and patience in sharing the frequency comb with me, you are a great colleague to work with. Jonas, it was fun to work together on the last project! Your positive attitude and great programming skills were indispensable throughout the final experiment. Jeroen, bedankt voor al je hulp en het ontwerpen van de ionenval.

Ook wil ik graag Jacques Bouma bedanken. Je technische inzicht, creatieve en snelle oplossingen en enorme voorraad aan handige componenten hebben mij heel erg geholpen bij mijn experimenten.

Heel veel dank ook voor de fijnmechanische instrumentmakerij! Een goede ondersteuning op dit vlak is onmisbaar in de experimentele fysica, en ik ben dan ook erg dankbaar voor alle hulp van vrijwel iedereen uit de instrumentmakerij tijdens mijn onderzoek. Ook wil ik graag de electronische werkplaats bedanken voor hun ondersteuning.

Eric-Jan van Duijn, bedankt voor je hulp bij met name het installeren van de ringlasers, en je bereidheid om van alles aan optische componenten uit je goed georganiseerde voorraden aan mij uit te lenen.

I would like to thank all the group members of the atomic physics group, who made the VU a very nice workplace. So, with the risk of forgetting important people (for which I apologize beforehand), thanks to Ofelia, Toncho, Lineke, John, Sandro, Itan, Paul, Adrian, Marina, Rob, Roel, Gareth, Tjeerd, Tom, Arjan, Dmitry, César, Daniel, Ruud, Valdas, Joop, Ruth, Ishrat, Thomas, Juliette, Maarten, Ali, Ziyu, Wim V., Rick, Kees, Ilse, Elmar, Wim H. and Dongfeng. Ook wil ik graag Marja Herronen bedanken voor het regelen van allerhande ondersteunende zaken.

Van buiten de VU wil ik graag Ton Riemersma bedanken voor zijn hulp met zaken die op de VU niet direct voor handen waren. Ik hoop dat we nog lang contact houden! Ook mijn dank voor de hulpbereidheid van Hugo Schlatter, het was altijd gezellig om bij jullie langs te komen. Verder ben ik erg dankbaar voor alles wat ik tijdens mijn masteronderzoek heb geleerd over schrijven en experimenteren van Ekkes Brück, Jacques Klaassen, Lian, Tegus, en alle anderen! Cam Thanh, your positive attitude is inspirational. We greatly appreciate the friendship we have with you and Duc, and wish for all the best for you and your family.

Tot slot wil ik ook nog graag mijn vrienden bedanken voor hun steun en de broodnodige afleiding en mijn ouders en zus en haar gezin voor hun altijd aanwezige steun en vertrouwen. En dan natuurlijk Stefan, ik zou bijna een dankwoord alleen aan jou kunnen wijden. Jij hebt me op zo ongeveer elke mogelijke manier geholpen bij het tot stand komen van dit proefschrift. Heel erg bedankt voor alles, en dan is nu de stress van onze proefschriften eindelijk voorbij!